

MODELING AND EXPERIMENTAL VALIDATION OF A RESILIENT EXTRATERRESTRIAL HABITAT INTERIOR ENVIRONMENT

by

Laura Collazo Carballude

A Thesis

Submitted to the Faculty of Purdue University

In Partial Fulfillment of the Requirements for the degree of

Master of Science in Mechanical Engineering



School of Mechanical Engineering

West Lafayette, Indiana

May 2023

THE PURDUE UNIVERSITY GRADUATE SCHOOL
STATEMENT OF COMMITTEE APPROVAL

Dr. Davide Ziviani, Chair

School of Mechanical Engineering

Dr. Shirle Dyke

School of Mechanical Engineering

Dr. Ilias Bilionis

School of Mechanical Engineering

Approved by:

Dr. Nicole Key

In memory of my grandpa, Americo Carballude Estevéz

ACKNOWLEDGMENTS

I am deeply grateful for the invaluable support, guidance, and encouragement I received from the many people who made my dissertation work and the invaluable experience gained along the way possible. Foremost, I extend my gratitude to my advisor, Professor Davide Ziviani, for his unwavering patience, guidance, and overwhelming support throughout the years. He struck a delicate balance between high expectations and a hands-off approach, allowing me the freedom to explore various projects and take on multiple responsibilities. I greatly appreciated his feedback and invaluable insights during our weekly research meetings. Also, the opportunity to be part of the International Refrigeration Course (IRC) was another significant experience, where I had the pleasure of meeting wonderful people and learning from them, especially Riley Barta. His attention to detail, detailed feedback, and crystal-clear perspective on what's important contributed significantly to my growth as a researcher. Furthermore, I cannot overlook the lessons I learned from Professor Ziviani outside the laboratory, which broadened my education and aided both my professional and personal development. I also want to acknowledge Professor Ziviani's belief in me and giving me the opportunity to come to Herricks Laboratories. I am forever grateful.

I extend my heartfelt gratitude to the Herrick Lab shop and staff for their unwavering patience, guidance, and diligence throughout the years. I want to give a special thanks to Dino and Frank for their exceptional expertise, sense of humor, and for always making time for me, no matter the questions I had. Dino taught me the value of persistence in the face of obstacles, which has been invaluable to my growth as a researcher. Frank's detailed feedback and crystal-clear perspective on what's important also played a significant role in my development as a researcher. I am also grateful to Jose and others who have provided me with their assistance, jokes, and a fun workplace. Their contribution to creating a positive work environment has been deeply appreciated.

This work would not have been possible without the support and guidance of numerous collaborators. First of all I would like to thank Shirley Dyke for giving the opportunity to work on Residential Extra-Terrestrial Habitat Institution (RETHi). RETHi is funded by NASA under grant or cooperative agreement award number 80NSSC19K1076. I would like to extend my appreciation to Jaewon Park for his earlier work, which initiated the cyber physical testbed effort. His contributions were critical to the success of this project. I would also like to thank NASA engineer

Julia Badger and Veridiam's chief executive officer, Brian Joyal, for their feedback and guidance throughout the project. Their insights and expertise were instrumental in shaping the direction of this research. Furthermore, I would like to thank Hunter Sakiewicz for his significant contributions to the project and for being a great source of motivation. His hard work and dedication were truly inspiring. I am also grateful for the helpful resources and support provided by Dawn R Whitaker, which greatly aided my research. Her guidance and expertise were invaluable. Lastly, I want to acknowledge Luca Vaccino for his outstanding support in the lab and outside of it. His willingness to help and his knowledge were always greatly appreciated.

I am deeply grateful to my colleagues and friends at Herrick Labs for creating a wonderful environment to conduct research. Your kindness, willingness to help each other, and dedication to excellence without taking yourselves too seriously have all been crucial to my growth as a researcher. I would like to express my gratitude to Andreas Hoess, Parveen Dhillon, Raghav Kakani, Fatih Meral, Oliver Obst, Doni Thomas, Gabriele Toffoletti, Xing Li, Ashta Shubham, Weigang Hou, Changkuan Liang, Murali Krishnan Rajasekharan Pillai, Abhignan Saravana, Adil Manzoor Shaikh, Jiselle Thornby, Feng Wu, Zixin Wang, and many others who have helped me along the way.

I also want to thank my family and friends outside of Herrick Laboratories for their constant love and support. Without them, I would not have been able to maintain my sanity and make progress in graduate school. I am particularly grateful to my mother and sister for always believing in me, and my friends at Purdue, including Debraliz Isaac, Kevin Shi, Mike Thoenen, Andrew Vuong, and Parker Farese, who have motivated me throughout the process. Additionally, I would like to extend a heartfelt thanks to Amanda Lial and Eloy Ferreiro Pérez, who have been my biggest supporters since the day I started, and I know I can always count on them.

TABLE OF CONTENTS

LIST OF TABLES	8
LIST OF FIGURES	9
EXTRA HEADINGS	13
ABSTRACT.....	15
1. INTRODUCTION	17
1.1 Motivation.....	17
1.2 Resilient Extra-Terrestrial Habitats Institute and Research Gaps.....	18
1.3 Thesis Objectives and Approach	19
2. OVERVIEW OF MCVT AND CPT ARCHITECTURES.....	22
2.1 Literature Review of Systems of Systems	22
2.2 Modular Virtual Coupled Testbed Overview	23
2.2.1 Data Distribution	26
2.3 Modular Coupled Virtual Testbed Boundary Conditions.....	27
2.3.1 Lunar Conditions	27
2.3.2 Lunar Habitat Concept.....	29
2.3.3 Disruption	31
2.4 Cyber-Physical Testbed Overview	32
3. ANALYTICAL HABITAT INTERIOR ENVIRONMENT MODEL.....	34
3.1 Analytical Model Description.....	34
3.1.1 Habitat Interior Environment Model Disturbances	35
3.2 Development of Habitat Interior Environment Model.....	41
3.2.1 Thermal Model	41
3.2.2 Pressure Model	52
3.2.3 Coupling of Thermal Model and Pressure Model	54
3.3 Analytical Verification of Thermal Habitat Interior Environment Subsystem.....	56
3.4 Fire Case Study of Thermal Transfer Model	58
3.4.1 Design optimization of the door between zones.....	60
4. CYBER-PHYSICAL TESTBED:DESIGN AND CHARACTERISTICS.....	64

4.1	Objectives	64
4.2	Cyber physical testbed code.....	67
4.2.1	Cyber-physical testbed model: Test setup A	68
4.2.2	Cyber-physical testbed model: Test setup B	72
4.2.3	Cyber-physical testbed model: Test setup C	75
4.3	Test setup A: Bladder control volume	79
4.4	Test setup B: Aluminum of the TTP control volume	84
4.5	Thermal transfer panel design.....	85
4.5.1	Components of thermal transfer panel.....	94
4.5.2	Thermal transfer panel experimental setup.....	96
5.	VALIDATION OF ANALYTICAL VERSUS EXPERIMENTAL RESULTS	99
5.1	Maximum heating scenario: Test A	99
5.1.1	Filtered data	101
5.1.2	Heating load.....	102
5.1.3	Infiltration Load.....	103
5.1.4	System Parameter Identification.....	104
5.2	Emergency Heating Scenario: Test B	108
5.3	Heating load Scenario: Test B	113
5.4	Cooling Scenario at setpoint 16 C with heating load: Test B	117
5.5	Thermal Transfer Panel: Test C	122
6.	CONCLUSION AND FUTURE WORK	124
6.1	Conclusion	124
6.2	Future Work	124
	APPENDIX A: SENSOR CALIBRATION	125
	APPENDIX B: MINI-SPLIT OPERATING PROCEDURE	132
	APPENDIX C: HEAT PUMP MODEL	133
	REFERENCES	135

LIST OF TABLES

Table 1- MCVT Lunar regolith properties [8]	29
Table 2- Nominal Design Parameter values for fire [28]	39
Table 3-Meteorite Impact Disturbances [24]	40
Table 4- Airlock Failure Disturbances [24]	40
Table 5- Key thermal resistance and unit thermal capacitance values [29], [31]–[33]	48
Table 6- Thermal gains due to human activity [36].....	49
Table 7- Thermal gains due to equipment [36].....	50
Table 8- Average load density [36]	50
Table 9- Fractions for radiative and convective heat flows [29]	51
Table 10- Parameters of dynamic pressure [24]	53
Table 11-Properties of air	75
Table 12- Sensor’s specification for Test A	80
Table 13- Sensor list for thermal transfer panel piping	97
Table 14- Optimization of resistance values.....	105

LIST OF FIGURES

Figure 1- Notional Real Habitat components [6].....	24
Figure 2-MCVT subsystems (adapted from [8])	25
Figure 3-Dataflow of MCVT subsystems (adapted from [8])	27
Figure 4-MCVT Lunar Habitat Concept [8]	29
Figure 5- MCVT Lunar habitat layout (to the right inside the habitat and to the left surrounding it) [8].....	31
Figure 6- MCVT Disturbance dataflow [8]	32
Figure 7- CPT architecture diagram	33
Figure 8-Inputs and outputs of HIEM in MCVT	35
Figure 9-Content fire stages (reproduced from [15]).....	37
Figure 10-Heat release rate of different fire types (adapted from [16])	38
Figure 11- Content fire temperature at ignition stage	39
Figure 12-Schematic of the relation between heat flows and loads.....	42
Figure 13- Schematic sensible cooling load calculation process.....	43
Figure 14- Schematic of zone one air energy flows	44
Figure 15-Schematic of heat flows for thermal network approach.....	44
Figure 16-Thermal resistance network of HIEM.....	45
Figure 17- HIEM temperatures with different internal gains	52
Figure 18-Responds of HIEM to changing temperature in the structure.....	56
Figure 19- Verification through MATLAB of HIEM model in EES	58
Figure 20- Responds to temperature in zone 1 with different fires	59
Figure 21-Temperatures of HIEM with respect to fire with respect to polyester (left) and alcohol (right)	59
Figure 22- Modification to the thermal resistance network.....	60
Figure 23- Door schematic.....	61
Figure 24- Standard door with methyl alcohol fire starting in zone 1	62
Figure 25- Optimum door with methyl alcohol fire starting in zone 1	62

Figure 26- Layers of the CPT testbed structural subsystem (top left), the habitat interior environment subsystem (top right) and the exterior layer subsystem and disturbance subsystem (bottom left and right)	65
Figure 27-Diagram of Testbed A for validating the normal conditions of the interior environment	65
Figure 28-Diagram of the Testbed B of validating the normal conditions of the interior environment	66
Figure 29-Diagram of the Testbed C of validating the normal conditions of the interior environment	67
Figure 30-Testing scenarios HIEM CPT code.....	68
Figure 31- Diagram of heat transfer of Test A	68
Figure 32-Thermal resistance network for Test A	70
Figure 33- Reduced thermal resistance network for Test A	71
Figure 34-Diagram of the layers of the CPT	72
Figure 35- Thermal resistance network for Test B	73
Figure 36-Microscopic view of the contact vs the air gaps of the interface between two materials	74
Figure 37-Diagram of heat transfer of Test C.....	76
Figure 38-Thermal resistance network for Test C	76
Figure 39-Test C thermal resistance network	77
Figure 40-PI&D of test setup A (adapted from [53])	80
Figure 41-Physical sensor inside the bladder and diagram of the location of air temperature readings	81
Figure 42-Physical sensor inside the bladder and diagram of the location of bladder in temperature readings	81
Figure 43- Physical sensor outside the bladder and diagram of the location of bladder out temperature readings	82
Figure 44-Simulink code of CPT sensor reading (adapted from [53])	83
Figure 45- The different layers beyond the bladder of the CPT. The structural subsystem (left), the thermal interface material (middle) and the thermal transfer panel (right)	84
Figure 46-The box which contains four lamps (left) and the heater to the right of the unit of the mini-split (right).....	85
Figure 47- The pressure box testbed (left) and the CAD model of the dome testbed(right)	86
Figure 48- CAD model of the configuration of the lab	87

Figure 49-The piping system of room 90 (left) and the pressure drops (left).....	89
Figure 50- The main piping system of room 80 (left) and the pressure drops (left).....	90
Figure 51- The pressure box piping system of room 80 (left) and the pressure drops (left)	90
Figure 52- Pressure drops calculated analytically of the pressure box	91
Figure 53-Preliminary design of the 9 thermal transfer panel piping	92
Figure 54- Preliminary design of the 9 thermal transfer panel sensors	92
Figure 55- Pressure drops of the overall system vs the heat pump curve.....	93
Figure 56- Physical thermal transfer panel (left) and the CAD model (right).....	93
Figure 57- Final CAD of the room configuration with full piping system.....	94
Figure 58- Components of thermal transfer panel	94
Figure 59- Diagram of TIM location	95
Figure 60-Thermal interface material from Dow thermal conductivity vs Viscosity [49]	96
Figure 61- PI&D of a single thermal transfer panel	98
Figure 62-Experimental data of the mini-split pressures (a) and mass flow (b), inside unit temperatures (c) and outside unit temperatures (d) at maximum heating mode.....	99
Figure 63- Experimental data of the mini-split pressures (a) and mass flow (b), inside unit temperatures (c) and outside unit temperatures (d) at maximum heating mode.....	100
Figure 64- Heating at 25 C data of thermocouples of the bladder in temperature (a), bladder out temperature (b) and bladder air temperature (c)	101
Figure 65- Filter data versus raw data of pressure at State 1 of the vapor compression cycle ...	101
Figure 66-Heating load experimental data versus analytical model.....	103
Figure 67- Temperatures of the bladder out thermocouples (a) , bladder in temperatures (b) and bladder air temperatures (c) of the heating infiltration testing	104
Figure 68- Experimental vs analytical model with the local error for average air temperature .	106
Figure 69-Experimental vs analytical model with the local error for bladder in temperature (a) bladder out temperature (b) in max heating scenario of the mini-split system.....	107
Figure 70-Experimental data of the mini-split pressure (a), relative humidity (b) and mass flow (c) running at emergency mode Part 1	109
Figure 71- Experimental data of the mini-split running outside unit temperatures (a) and inside unit temperatures (b) at emergency mode Part 2	109
Figure 72-Experimental data of the thermocouples of the bladder out temperature (a), the bladder in temperature (b) and air temperature (c) at emergency mode.....	110

Figure 73-Experimental data of the thermocouples at the layers of the CPT at emergency mode	111
Figure 74-Experimental vs analytical model with the local error for air bladder temperature (top) and aluminum plate temperature (b) in emergency scenario of the mini-split	113
Figure 75-Experimental data of the mini-split not running	114
Figure 76-Experimental data of the thermocouples at the layers of the CPT with heaters	115
Figure 77-Experimental data of the thermocouples of the outer bladder temperature (a), inner bladder temperature (b) and air bladder temperature (c) with no-mini split.....	116
Figure 78-Experimental vs analytical model with the local error for air bladder temperature (a) and aluminum plate temperature (b) with heaters	117
Figure 79-Experimental data of the mini-split running at cooling mode.....	118
Figure 80-Experimental data of the thermocouples of the bladder at cooling mode.....	119
Figure 81-Experimental data of the thermocouples at the layers of the CPT at cooling mode ..	119
Figure 82-Cooling load experimental data versus analytical model.....	120
Figure 83-Experimental vs analytical model with the local error for air bladder temperature (a) and aluminum plate temperature (b) with cooling load.....	121
Figure 84-Pressure drop across thermal transfer panel.....	122
Figure 85-Temperature vs pressure drop of the system.....	123
Figure 86-Load of thermal transfer panel at different flow rates.....	123

EXTRA HEADINGS

Symbols:

A	Area [m ²]
C	Unit thermal capacitance [Btu / °F] & [W/ °C]
C_d	Discharge coefficient [-]
C_L	Loss coefficient [-]
L	Length [m]
\dot{m}	Mass flow rate [kg/s]
μ	Dynamic Viscosity [Pa-s]
Nu	Nusselt number [-]
P	Pressure [kPa]
Pr	Prandtl number [-]
Q	Heat transfer [kJ]
\dot{Q}	Heat transfer rate [kW]
\dot{V}	Volumetric flow rate [m ³ /hr]
R	Thermal Resistance [hr-°F/Btu] & [hr-°C/W]
Ra	Rayleigh's number [-]
ρ	Density [kg/m ³]
\dot{m}_f	Burning rate[m/s ²]
A_B	Burning area[m ²]
\dot{m}''_f	Burning rate per unit area [m/s ² -m ²]
α	Fire release rate [K/W]
ΔH_C	Enthalpy difference of combustion [J]
r_B	Burning radius [m]
V_s	Flame spread velocity [m/s ²]
t	Time [s]
$F_{g,c}$	Convective fraction coefficient [-]
$F_{g,r}$	Radiative fraction coefficient [-]

T	Temperature [$^{\circ}\text{C}$]
Ra	Rayleigh number [-]
Gr	Grashof number [-]
α_{air}	Thermal expansion coefficient [K^{-1}]
k_{air}	Thermal conductivity of air [W/m-K]
ν_{air}	Viscosity of the air [N-s/m^2]
c_p	Coefficient of pressure[pcm/MPa]
c_v	Coefficient of volume [K^{-1}]
E_{cv}	Energy in a control volume [J]
V	Volume [m^3]
h	Enthalpy [J]
W	Work [J]
g	Gravitational acceleration [m/s^2]

Abbreviations:

CPT	Cyber-physical testbed
ECLSS	Environmental control life support system
EMS	Electro-mechanical systems
HIEM	Habitat interior environment model
HMS	Health management systems
MCVT	Modular coupled virtual testbed
NASA	National aeronautics and space administration
NRH	Notional real habitat
RETHi	Resilient extra-terrestrial habitat institute

ABSTRACT

The NASA-funded Resilient Extra-Terrestrial Habitat Institute (RETHi) aims at developing the necessary fundamental knowledge to enable the design of future resilient deep space habitats. To achieve this, RETHi has developed a Modular Coupled Virtual Testbed (MCVT) consisting of various subsystems (such as power, structural, ECLSS, etc.) to simulate a range of deep space hazardous scenarios and assess the ability of the systems to recover from expected and unexpected fault scenarios under both crewed and uncrewed situations. The physics-based Simulink models within MCVT allow for direct interconnections among components, including damage cascading effects, repairability features, and various failures. Besides the MCVT platform, a Cyber Physical Testbed (CPT) has also been conceptualized to perform real-time experiments with physical portions of the MCVT models (e.g., structural, thermal and pressure management systems). The overarching goal of CPT is to implement and validate decision-making algorithms under various scenarios (e.g., leaks, thermal bridges, etc.), introduce controllable and realistic uncertainties (e.g., communication delays, sensing faults, etc.), and assess resilience, control effectiveness and autonomy. The CPT design consists of three main physical systems: the inflatable bladder, the aluminum dome structure, and the thermal transfer panels connected to a low-temperature chiller. Pressure and temperature controls inside the bladder are achieved by means of a pressure regulator and a mini-split heat pump system, respectively.

One of the core aspects of both MCVT and CPT is the habitat interior environment which includes the coupled temperature and pressure effects due to interior and exterior loads as well as the necessary conditions to ensure the crew survival.

As part of this work, a dynamic Habitat Interior Environment Model (HIEM) has been developed to simulate the behavior of a two-zone habitat in real-time. The model can directly interact with other subsystems such as the ECLSS and structural protective layer (SPL) and features various disturbances including pressure leaks due to meteorite impacts or airlock failures. The HIEM has been further extended to also include various fire intensity scenarios and also to enable the isolation of the zones by means of a door in case of an emergency or simply due to the architecture of the future habitat.

The CPT system is utilized to test the capability of HIEM in predicting the behavior of the interior environment in various scenarios. To impose the necessary thermal loads to the habitat structure (i.e., aluminum skeleton and inflatable bladder) in the laboratory environment, thermal transfer panels with coiled copper piping and aluminum heat spreaders have been designed to provide uniform temperature distributions. A cryogenic chiller with Syltherm as the working fluid is used to maintain and provide the necessary operating range between -40 °C and 60 °C.

The HIEM was modified to describe the physical sizing of the bladder as well as to capture the heat transfer characteristics between the bladder, the aluminum structure, and thermal transfer panels. In addition, the models also included the effects of air infiltrations within the bladder, various sources of heat losses by conduction and convection, and thermal resistances associated with non-perfect contacts between bladder and transfer panels. Experimental data was used to validate the model predictions and different operating conditions as well as to improve the model accuracy by identifying key thermal resistances and capacitances.

The HIEM was able to predict the temperature variations inside the bladder with a relative error of <3%. The accuracy of the HIEM temperature and pressure variations is affected by the heat pump model and the dynamics of the bladder. To minimize the errors, a detailed thermal resistance/capacitance network was developed. However, the equivalent thermal resistance network built to predict the heat transfer characteristics of the aluminum plate of the thermal transfer panel showed discrepancies up to 24% due to air gaps existing between the bladder and the panels as well as additional heat losses. Further testing and appropriate insulation can mitigate the thermal losses of the existing design.

Finally, the HIEM has been updated to assess the ability of CPT to experimentally recreate scenarios investigated within MCVT. Parametric studies have been conducted to predict temperature variations within the bladder due to changes in boundary conditions imposed by the transfer panels.

Based on the numerical and experimental analyses resulted in meaningful recommendations were identified to improve the design and operation of CPT.

1. INTRODUCTION

1.1 Motivation

Humanity's curiosity about the unknown has driven the exploration of new frontiers, leading to an improvement in the quality of life on Earth. Space exploration has played a significant role in this advancement, with over fifty years of human activity in space. The journey began on October 4th, 1957, with the launch of the world's first satellite, Sputnik. [1]. The first satellites contributed to critical knowledge and capabilities for developing satellite telecommunications, global positioning, and weather forecasting advances [2]. Over time, space exploration has made significant contributions to various aspects of daily life, including the development of solar panels, implantable heart monitors, cell phones, cancer therapies, lightweight materials, water purification systems, and improvements to the global search-and-rescue system. [3]. Explorations in the future have the potential to provide immediate benefits to Earth in a wide range of areas, including but not limited to materials, power generation, energy storage, recycling, waste management, advanced robotics, medicine, transportation, engineering, computing, and software [2].

In 1972, the Apollo 17 mission was the last time humankind saw a man walk on the moon, even though the investigation of new land enhances everyday life [1]. Efforts have been underway to establish a Low Earth Orbit space station, such as the ISS, since Apollo 17, with the goal of advancing exploration of deeper space. However, the idea of creating habitats for human settlements beyond Earth has generated interest around the world, rekindling the exploration of the Moon. As a result, NASA has initiated the Artemis project with the aim of establishing a long-term human presence on the Moon by 2025, with the Artemis III mission being the first step towards achieving this goal [4].

To reach the next milestone in the age of space exploration, humans must be prepared to handle unfamiliar situations both inside and outside the spacecraft. One crucial aspect of designing lunar habitats is to minimize the amount of material used while ensuring it can withstand extreme disturbances such as meteorites, moonquakes, and light cycles. Casanova and Sureda [5] outlines a wide range of potential benefits and challenges for building lunar habitats. The Lunar Surface Innovation Initiative (LSII) of NASA's Space Technology Mission Directorate (SpaceTech) is developing technologies for lunar surface exploration within the Lunar Surface

Innovation Consortium (LSIC) [6]. It is a challenging task to create a habitat that can endure uncertain levels of damage. To tackle this challenge, NASA has chosen to work with two Space Technology Research Institutes (STRIs) that will focus on creating systems for space habitats. The selected programs are the Habitats Optimized Missions of Exploration (HOME) and the Resilient Extra-Terrestrial Habitats Institute (RETHi) [6]. HOME aims to develop and demonstrate technologies and systems that enable long-duration human missions beyond low-Earth orbit, with a specific focus on the design and optimization of habitats for lunar and Martian missions. HOME will conduct research in several areas, including habitat design, life support systems, radiation shielding, and in-situ resource utilization.

1.2 Resilient Extra-Terrestrial Habitats Institute and Research Gaps

The Resilient Extra-Terrestrial Habitats Institute (RETHi) is focused on developing fundamental knowledge and technologies to create and maintain resilient extra-terrestrial habitats. RETHi's research is centered around three main areas: resilience, awareness and robotics. Specifically, RETHi aims to develop a comprehensive understanding of what makes an environment habitable for humans, develop technologies that enable habitats to operate autonomously, and develop technologies and systems that ensure the long-term performance of extra-terrestrial habitats [7].

To design lunar habitats the approach needs to adequately consider the wide range of potential hazards, emergent behaviors of complex systems, or hardware degradation over time. To address these challenges, RETHi is developing a Modular Coupled Virtual Testbed (MCVT) that utilizes computational models as a system of systems (SoS) to identify gaps in existing approaches and to develop resilient and autonomous smart habitats. The success of such investigation is heavily dependent on the capacity of the numerical models to capture accurate physical behaviors. To validate the complex system of systems a real-time multi physics Cyber Physical Testbed (CPT) is being developed. CPT is design to capture rate dependent behaviors in physical substructures [8]. This type of testing enables the evaluation of various design approaches under simulated hazardous and extreme environments in a cost-effective and timely manner.

There have been investigations and simulations conducted regarding failures of habitat systems in space, aimed at understanding potential risks and developing strategies to mitigate them.

These efforts involve various organizations, including NASA, and have contributed to the development of guidelines and standards for designing resilient habitats in space [9].

The Advanced Exploration Systems (AES) program by NASA aims to develop and demonstrate the technologies needed for human exploration of deep space[10]. One of the objectives of AES is to enhance crew health and performance by developing systems that can support extended human presence beyond low Earth orbit[10]. Exploration Systems Architectures Study (ESAS), on the other hand, is a NASA-led effort to define and evaluate human and robotic exploration mission architectures for the Moon, Mars, and beyond [11]. The objective of ESAS is to identify potential mission concepts that can achieve NASA's exploration goals [11]. The Deep Space Habitability Design Guidelines (DSHDG) is a project that aims to establish a set of design guidelines for deep space habitats. These guidelines include criteria for environmental control and life support systems, human factors, crew health and safety, and system maintainability [9].

While the programs at NASA are focused on developing the specific technologies and systems required for human space exploration, RETHi has a broader scope and focuses on developing the overall concept of resilient habitats for human space exploration and settlement. RETHi's research is essential to ensure the long-term viability of human presence in space and on other celestial bodies, by developing technologies and systems that can operate autonomously and sustainably in extreme and challenging environments. Therefore, RETHi fills a research gap by focusing on the development of fundamental knowledge and technologies to create and maintain resilient and sustainable extra-terrestrial habitats, which is not the primary focus of AES, ESAS, and DSHDG.

1.3 Thesis Objectives and Approach

The aim of this thesis is to develop, design, and execute a CPT with specific focus on the Habitat Interior Environment Model (HIEM) and its integration into the larger computational models of the System of Systems (SoS) referred to as MCVT. In other words develop and validate the HIEM. The HIEM must possess all the specified objectives and demonstrate the ability to effectively predict the dynamics characteristics of the physical system, the HIEM CPT. To accomplish these overarching goals, the following objectives have been identified and divided into two subgroups:

MCVT

- Develop a numerical simulation of a two-zone Habitat Interior Environment with integrated air-lock feature to meet the real-time requirements set by MCVT.
- Must include the following disruption with different intensity levels: meteorite strike, internal disturbance (e.g., people, equipment) and fire.
- The HIEM MCVT model needs to accurately account for the latent and sensible loads, air leaks (in both the structure and zonal barriers), pressure loss, and ventilation/recirculation functionalities of the system.
- Predict the coupling between temperature and pressure in the computational model.
- To compare the results of the HIEM model through Engineering Equation Solver (EES) with MATLAB results in normal conditions and analyze any discrepancies.
- Review and develop specific fire HIEM MCVT disruption.
- Analytically verify whether the HIEM model responds and works properly in the presence of disruptions when integrated in MCVT.
- Utilize the HIEM MCVT code to devise the optimal design for the doorway that connects the two zones within the interior environment.

CPT

- Develop, optimize, and construct a CPT testbed aimed at verifying the accuracy and validity of the HIEM.
- Develop a numerical simulation of a two-zone HIEM to be executed on SpeedGoat according to requirements set by CPT.
- Experimentally validate the Habitat Interior Environment numerical simulation with the CPT experimental results

The thesis is structured in six chapters to address the research objectives outlined. Specifically, Chapter 2 consists of a literature review of real-time computational system used to also to provide an overview of MCVT (Section 2.1), the subsystems and dataflow (Section 2.1.1), the boundary conditions of the lunar habitat assumed for MCVT (Section 2.2.1), the parameters of the lunar habitat (Section 2.2.2), and the disruptions tested in MCVT (Section 2.2.3). Additionally, Section 2.3 provides an overview of the CPT.

Chapter 3 describes the analytical method and is divided into three sections: assumptions and disruptions (Section 3.1), the HIEM code (Section 3.2), and the results (Section 3.3).

Chapter 4 explains the experimental method, which is known as the CPT. It starts with an introduction of the boundary conditions and goal of the experiment (Section 4.1), followed by the development of the HIEM CPT from the MCVT code (Section 4.2). Then, the chapter describes the testing procedure for the different experiments, which are divided into two parts to validate the HIEM in normal conditions (Section 4.3-4.4), and the design of the transfer panel to fully validate the HIEM code for disruption scenarios (Section 4.5).

Then chapter 5 includes the results and the verification of the experimental data versus the analytical data.

Chapter 6 presents the discussion and conclusions from the analytical method regarding the experimental data acquired throughout the study.

2. OVERVIEW OF MCVT AND CPT ARCHITECTURES

2.1 Literature Review of Systems of Systems

Computational modeling and systems of systems (SoS) approaches are becoming increasingly popular across various industries and fields, including space exploration [12]–[18]. While the Modular Couple Virtual Testbed (MCVT) developed by RETHi is designed specifically for space habitats, there are other organizations and institutions utilizing similar approaches for developing resilient and autonomous systems for various applications.

The Smart Cities and Communities initiative funded by the European Union is developing simulation and modeling tools to optimize energy consumption and resource utilization in buildings and other urban infrastructure[14]. The National Institute of Standards and Technology (NIST) is developing a Disaster Resilience Framework that includes computational models and simulations to test the resilience of critical infrastructure systems in the event of natural disasters or other emergencies[12]. The Federal Aviation Administration (FAA) is developing a Systems Engineering Research Center (SERC) to advance systems engineering approaches for aviation systems [13]. The National Security Agency (NSA) is developing a Cybersecurity Directorate that utilizes systems engineering and modeling tools to develop resilient and secure information systems for government and private sector organizations[15].

Apart from MCVT developed by RETHi, there are several other examples of MCVT systems being developed for space exploration and lunar habitats. NASA's Kennedy Space Center has developed the Lunar Analog Simulation Suite (LASS), which allows researchers to simulate and test lunar habitats and exploration systems in a variety of scenarios [16]. The Lunar Habitats Initiative, led by the National Space Society, is developing sustainable lunar habitats, including a Virtual Habitat Testbed (VHT) that uses simulation and modeling tools to test and optimize habitat designs [17]. NASA's Langley Research Center has conducted the Lunar Base Systems Study (LBSS), a systems engineering study focused on developing sustainable and resilient systems for lunar habitats [18]. The study includes the development of a Virtual Lunar Habitat Testbed (VLHT) that uses simulation and modeling tools to evaluate the performance and resilience of lunar habitats under various conditions.

The MCVT approach is particularly effective for developing resilient and autonomous lunar habitats. MCVT systems can create highly realistic simulations of lunar habitats and exploration systems, allowing researchers to test and evaluate designs and systems under a wide range of conditions. Additionally, MCVT systems provide a cost-effective alternative to physical testing and allow researchers to rapidly iterate on designs and test multiple scenarios quickly and efficiently. MCVT systems also facilitate collaboration between researchers and stakeholders, allowing multiple teams to work together to develop and test designs in a virtual environment.

In conclusion, computational modeling and systems of systems approaches are becoming increasingly popular across various industries and fields for developing resilient and autonomous systems. While MCVT developed by RETHi is specific to space habitats, there are other organizations and institutions utilizing similar approaches for various applications, including Smart Cities, Disaster Response, Transportation, and Cybersecurity. In addition to MCVT developed by RETHi, several other MCVT systems are being developed for space exploration and lunar habitats. MCVT systems are particularly effective for developing resilient and autonomous lunar habitats due to their ability to provide highly realistic simulations, computational cost-effectiveness, rapid iteration.

2.2 Modular Virtual Coupled Testbed Overview

RETHi (Resilient Extra-Terrestrial Habitats Institute) has developed Modular Virtual Coupled Testbed (MCVT) as a tool to evaluate the resilience of space habitats by incorporating safety controls and repair strategies. In order to enhance the resilience of the habitat and plan for hazard mitigation and repair strategies, it is necessary to model disruptive events, their propagation, and the impacts on various subsystems [8]. Therefore, the MCVT framework allows fast plug-and-play testing of different subsystems associated with various components of a notional space habitat.

MCVT is a MATLAB Simulink model that has been chosen for its flexibility in solving dynamic equations and optimization problems [19]. It allows for the integration of custom blocks and can be easily coupled with rapid prototyping platforms such as SpeedGoat to develop digital twins, hybrid simulations, or hardware-in-the-loop testing [19]. The latest version of MCVT v6.2 has the capability to perform complex simulations based on seven disruptions and sixteen disruption scenarios (see Section (2.3.3)) [8].

The MCVT code is a system-of-systems simulation platform that comprises different subsystems (e.g., structural, thermal and pressure management systems, etc.). These subsystems form a subset of the component subsystems that are part of the Notional Real Habitat (NRH). Notional Real Habitat is a hypothetical space habitat used as a concept for designing and testing various subsystems, sensors, and fault models. The NRH is needed to provide a realistic for testing and validating technologies that are meant to be used in future space habitats. NRH allows researchers to evaluate the performance of different subsystems under various conditions and to identify potential problems before they occur in actual space missions [6]. By simulating the conditions of a real space habitat, the NRH helps to ensure that the technologies and systems being developed are safe, reliable, and efficient. The selection of subsystems for the MCVT is done to preserve the critical and representative functionalities of an integrated extraterrestrial habitat system. The conceptualization of the NRH is shown in Figure 1.

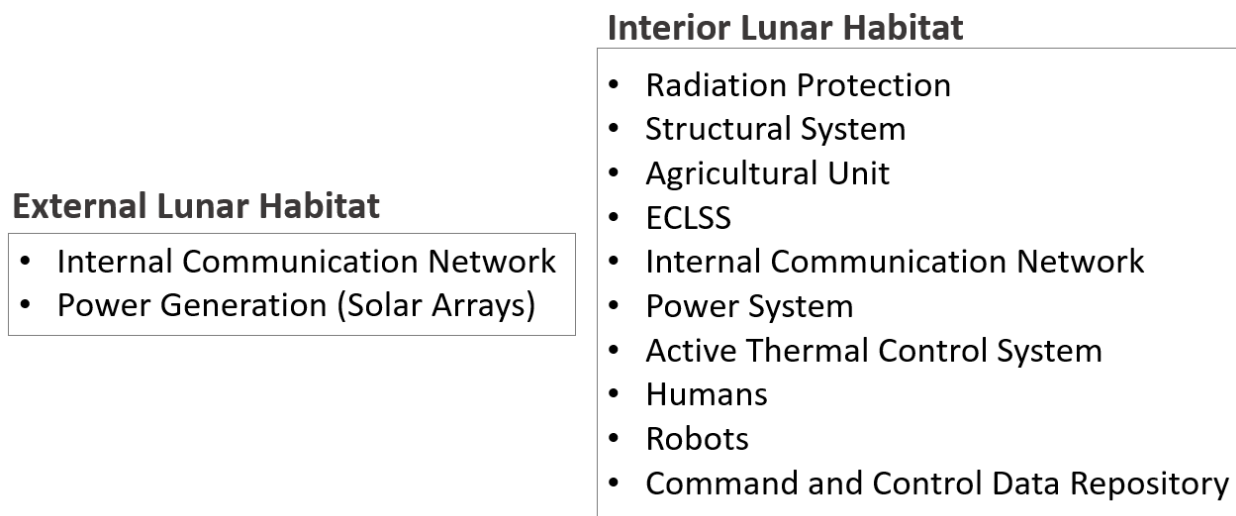


Figure 1- Notional Real Habitat components [6]

The MCVT's component subsystems are classified into three categories as illustrated in Figure 2: 1) Electro-Mechanical Systems (EMS), 2) Health Management Systems (HMS), and 3) Agent Systems. EMS subsystems directly propagate the physics of the habitat in both its operational and hazard states. HMS subsystems are present primarily for system evaluation and decision-making. HMS include an internal and interplanetary communication network, a command & control system, and a data repository. Human and robotic agents serve as the interface

between the EMS and HMS subsystems, playing significant roles in each by effecting physical changes in the habitat according to HMS directives. EMS subsystems encompass the Structural Protective Layer (SPL), Structural system (SS), Habitat Interior Environment Model (HIEM), Environmental Control and Life Support system (ECLSS), and Power system (PS), all of which are responsible for propagating the physical response through the habitat system.



Figure 2-MCVT subsystems (adapted from [8])

The SPL in the habitat is comprised of lunar regolith and serves the purpose of preventing radiation as well as dissipating meteorite impacts. The structural subsystem supports the insulation panels and the SPL. The Power subsystem comprises power generation (both nuclear and solar), energy storage (in the form of batteries), and a smart power distribution system, which can optimize power dissipation and battery life. The ECLSS maintains a constant temperature and pressure within the habitat by providing cooling and heating. This subsystem is comprised of the interior pressure control system (IPCS) and active thermal control system (ATCS). Finally, the Habitat Interior Environment model (HIEM) predicts the temperature and pressure within the two-zoned habitat and includes an airlock system to ensure access to the habitat. Both temperature and pressure change in real-time in response to physics from other subsystems. In addition to predicting the temperature of the interior environment, the HIEM model can also predict the humidity levels and the amount of ventilation required to maintain a comfortable and healthy living environment. The development and functionality of HIEM will be explained in detail throughout this work.

The communication network simulates the communication infrastructure utilized to facilitate the flow of data. The command-and-control system determines the necessary actions to

maintain or restore system functionalities. The data repository stores sensor data and information related to fault detection and diagnosis.

The Agent System is responsible for the actions of both human and robotic agents and tasked with repairing damage resulting from disturbances to the various subsystems. It comprises the Health Management System (HMS), which conducts periodic checks on signals generated by the fault detection and diagnosis block (FDD). Upon detection of a fault, the output of these periodic checks will trigger agent activity. In the current version of MCVT (v6.2), there are 117 distinct failure modes that can occur in the lunar environment, including meteorite impacts, dust accumulation, moonquakes, airlock failure, and fire. These disturbances can also have a cascade effect, where one event can trigger another. For instance, a meteoroid impact could penetrate the interior environment and damage the ECLSS, potentially leading to a fire.

2.2.1 Data Distribution

The interaction among subsystems is complex. To ensure proper communication and interaction, four distinct types of signals (cyber, intervention, physical and disruption) have been created as shown in Figure 3. Physical signals (indicated by light blue) are essential to the functioning of EMS subsystems and represent physical phenomena within the habitat. EMS subsystems communicate with each other by exchanging these signals to check their overall functionality. Cyber signals (indicated by orange lines) simulate sensor data, including corresponding noise and errors, as it would occur in real-life scenarios. This data is sent to the FDD for monitoring the health of the system. Disruption signals are sent or received by the disruption matrix (indicated by dark blue lines). When a disruption occurs, the disruption matrix sends specific parameters to each EMS subsystem to notify them of how each subsystem is affected. In return, the EMS subsystems send the conditions of each subsystem back to the disruption matrix (as explained in greater detail in Section 2.3). Agent intervention signals are double-format vectors containing information about repairing rates, agent availability, and repairing IDs.

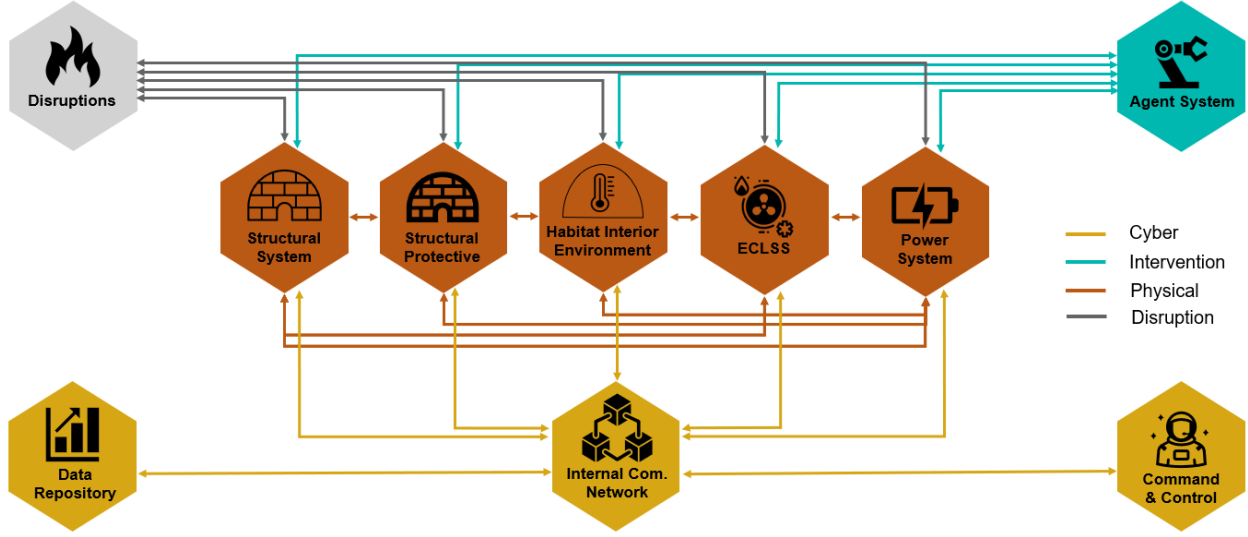


Figure 3-Dataflow of MCVT subsystems (adapted from [8])

2.3 Modular Coupled Virtual Testbed Boundary Conditions

2.3.1 Lunar Conditions

The Moon completes an approximately circular orbit around the Earth every 27.32 days. As a result of this orbit and its tilted rotational axis, only one side of the Moon is illuminated at any given time. [20]. For approximately 14 days, one side of the Moon is illuminated and experiences temperatures of up to 123°C, while the other side remains in darkness for an equal period and can experience temperatures as low as -233°C (Table 1). At the poles, certain craters remain unexposed to sunlight for billions of years and can reach temperatures as low as -272°C. [20]. In the polar regions of the Moon, there exists the potential for prolonged periods of continuous sunlight. These areas are known as "peaks of eternal light" (PEL). In these regions, the Sun is situated close to the true horizon, rising no more than 1.54° above it. [5].

The location of the proposed lunar base involves a broad range of factors that need to be considered. These factors include geography, geology, temperature, atmosphere, radiation, meteoroids, lunar dust, and seismic activities. Additionally, the chosen location can impact the complexity of thermal management systems.

When considering the equatorial region, nighttime would be less challenging. On the other hand, the polar regions would present the opposite issue. However, research in the past decade has indicated the potential for a base at the Moon's poles, particularly the south pole [2].

The lunar poles present a range of advantages for a habitable base [2]. These include reduced energy storage needs due to the abundance of sunlight, less extreme temperature variations, the presence of hydrogen, and interesting geological complexity and shadowed regions that are ideal for scientific experiments. Additionally, transporting humans and equipment to the south pole requires less fuel. Finally, there is the possibility of a peak of eternal light at the poles.

It is worth noting that through billions of years of meteorite and micrometeorite impacts, a layer of regolith has been produced that covers the entire lunar surface. This soil contains various particles, such as rocks, minerals, and glass fragments [5]. These effects have expanded the types of lunar heavy stone materials and caused these external particles to fuse with particles that already exist on the surface. The presence of iron makes fusion possible. This mixture of native and external materials in the lunar soil forms the composition of lunar dust [3].

The particle size distribution of lunar soil is very wide. Over 95% of the lunar soil is less than 1mm thick and a thickness of 60 μm is around 50% [20]. The main elements in lunar rocks and soils that compose 99% of the mass consists of seven chemical elements: oxygen (O), silicon (Si), aluminum (Al), calcium (Ca), iron (Fe), magnesium (Mg) and titanium (Ti). In the case study of lunar habitat of MCVT, Table 1 summarizes the main lunar regolith properties assumed. Additionally, the low pressure on the Moon has numerous implications for anyone planning to relocate there. The range of pressure on the Moon is very low due to its lack of atmosphere. The pressure on the Moon's surface during the day is typically around 10^{-7} to 10^{-14} atmospheres (atm). Microgravity, also known as very low gravity or near-zero gravity, appears on the surface of the moon due to its weak gravitational pull. The gravitational acceleration on the surface of the moon is about one-sixth of the Earth's gravity, which is equivalent to 1.62 m/s^2 . At such a low pressure, structural designs necessarily become more complex. Inevitably, exploration on the Moon will be constrained by this low pressure.

Table 1- MCVT Lunar regolith properties [8]

Regolith Properties	Value	Units
Emissivity	0.97	-
Absorptance	0.87	-
Density	2,000	kg/m ³
Thermal conductivity	0.014	W/m-K
Specific heat	1,053	J/kg-K
Compressibility	0.175	-

2.3.2 Lunar Habitat Concept

The four main criteria for habitat design can be summarized into the categories of habitable volume, radiation protection, weight, and shell thickness [21]. In designing the structure of the module, the key requirement is to minimize the material employed. In other words, there needs to be a balance between the performance under compressive and tensile stresses and the quantity of material needed. Through deep research and evaluation of the design criteria, it has been validated that a tunnel, hatch area, cylinder, and end dome are the most suitable design elements for the habitat. [22]. A hemispherical thin-shell (dome) differs from traditional beam systems in that it cannot withstand bending under any system of symmetrical loads. The compression stress of the dome is primarily distributed along the latitude direction, while in the longitude direction, it is regularly constrained by tensile stress. [2]. Concluding that an inflatable module is an accurate assumption for the MCVT lunar habitat. See Figure 4.



Figure 4-MCVT Lunar Habitat Concept [8]

Regolith can be a proposal for thermal and radiation protection [21], [22], as it is seen in Figure 4. To protect from radiation minimum protection of $7,000 \text{ kg/m}^3$ is required for shielding against highly energetic extraordinary solar flares. Radiation protection is a function of the thickness and density (around $1,300 \text{ kg/m}^3$) [23]. If the optimum thickness is 5.38 m, then to effectively shield against quiet-Sun conditions, the density value would be decreased to $4,000 \text{ kg/m}^3$, resulting in a thickness of 3.07 m. For the MCVT lunar habitat since it has a density of $2,000 \text{ kg/m}^3$ a thickness of around 1 m is proposed [8].

The lunar habitat has been designed with three distinct layers. The first layer is referred to as the Interior Environment, which is made up of a base surface area of 19.63 m^2 and a total volume of 32.72 m^3 . For safety reasons, the Interior Environment (HIEM) is divided into two zones, as detailed in Section 3.1 of the thesis. The second layer is the structural layer, which has a thickness of 0.4 m, while the third layer is the external protective layer, which is constructed from regolith.

Figure 5 illustrates the subsystems located within the HIEM, with the reference frame starting at the center of the habitat. These subsystems include ECLSS (thermal and pressure management systems) in zone two, power subsystem (energy storage, power distribution, and power conversion), command and control, and data repository. On the other hand, the components surrounding the habitat, such as the power subsystem (solar arrays and nuclear reactor) and ECLSS (external radiator), are shown to the right of Figure 5. The habitat also includes an inventory and storage depot for the robotic agents and a launch and landing site.

It is important to note that the MCVT assumes a 1/5th scale of the NRH, which is compatible with the dimensional scaling of the cyber-physical testbed.

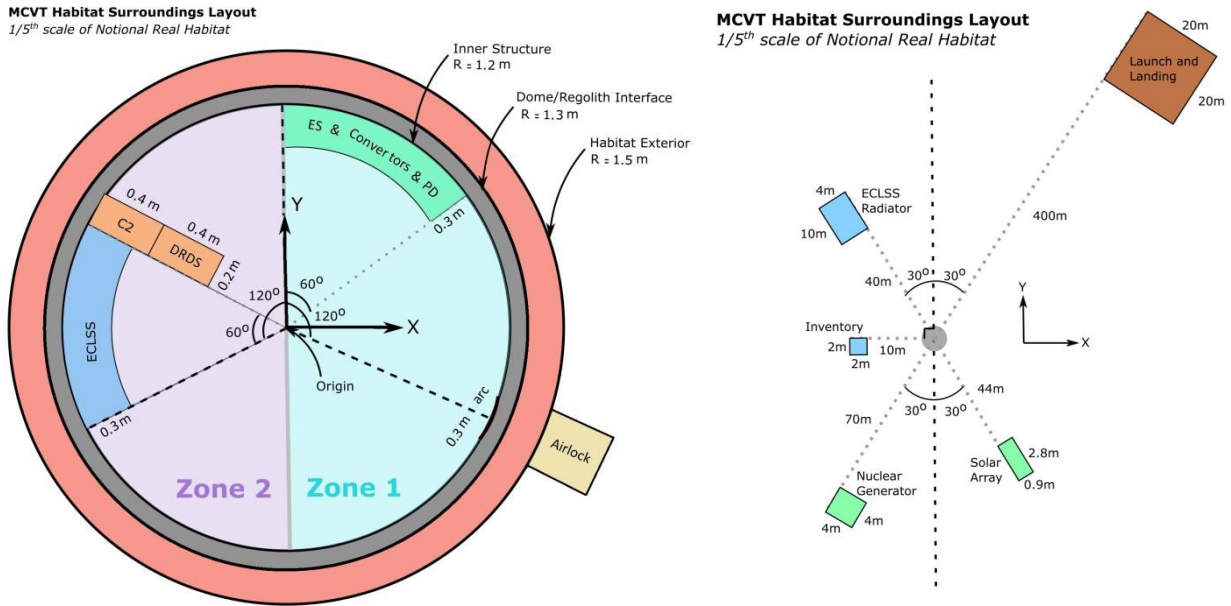


Figure 5- MCVT Lunar habitat layout (to the right inside the habitat and to the left surrounding it) [8]

2.3.3 Disruption

The disruption that can impact the lunar habitat refer to various disruptions that may alter its nominal conditions. In MCVT v6.2, meteorite impacts, dust accumulation, moonquakes, airlock failure, and fire are among the scenarios considered. These scenarios can be simulated in almost real-time with all subsystems operating simultaneously.

Both physical effects and phenomenological approaches have been employed to model these disruption. Physics-based models employ input parameters in the governing equations and lumped parameter models (e.g., meteorite mass), while phenomenological methods consider the effects of a disruption through a general concept (e.g., meteorite impact may damage the radiator of ECLSS). The hazard is measured through an intensity level from 1 to 5 using phenomenological cases. The modelers of each subsystem consider these intensity levels and create various case studies for each level. Figure 6 displays the physical system behavior of the subsystem within the disruption matrix.

Disruption signals can be classified as either integer or double signals. Phenomenological signals are represented by integer values and are used to determine the severity of the disruption's impact on other subsystems, without focusing on a specific physical interpretation. On the other hand, physical disruption signals are represented by double values, which denote the actual

physical damage to a subsystem. For instance, the size of a meteorite hole is considered a physical disruption signal.

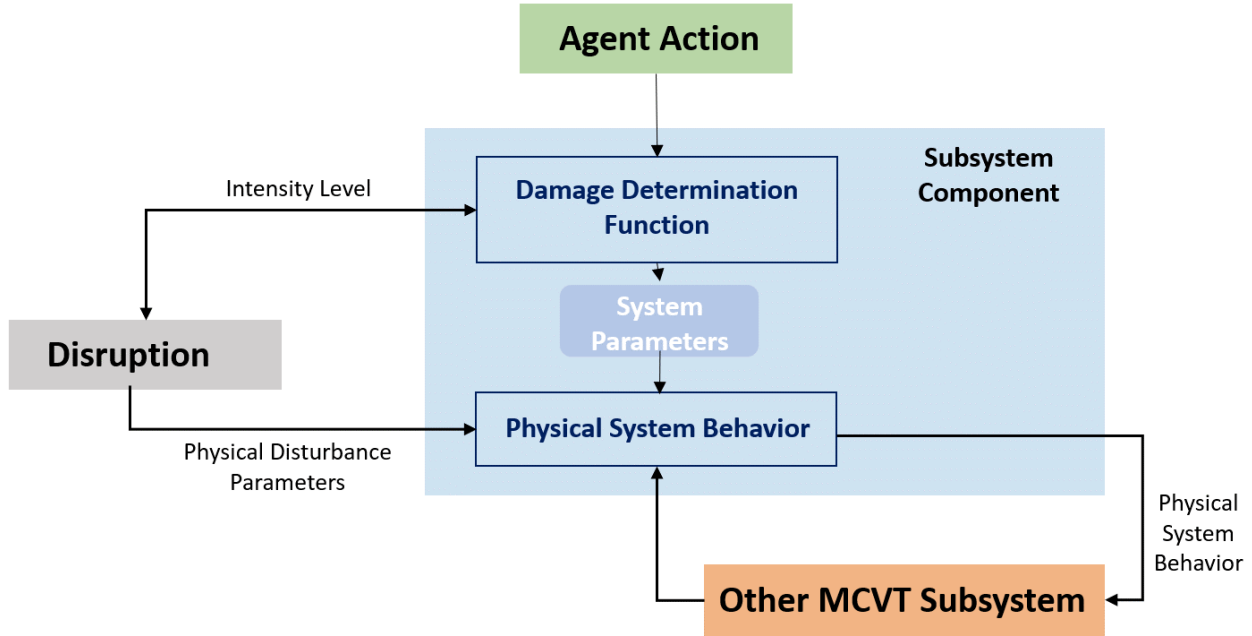


Figure 6- MCVT Disturbance dataflow [8]

2.4 Cyber-Physical Testbed Overview

Cyber-physical testing involves coupling computational models with physical models to study their dynamic interaction. It is also known as hybrid simulation, dynamic sub-structuring, or dynamic virtualization. This approach allows for gaining insight into the behavior of physical systems for which there is limited prior knowledge, and lunar habitats provide an ideal case study for this purpose. The testbed enables the validation of the results obtained in MCVT to ensure their realism and a better understanding of the physics of the habitat. Furthermore, CPT enables the testing of different disturbances and their impact on the habitat with a single testbed.

The CPT consists primarily of two subsystems: the physical subsystem and the computational subsystem seen in Figure 7. The computational domains contain models of the power subsystem, agents, structural protective layer, and health management. The physical domains comprise physical specimens of those parts of the system that are difficult to model computationally, such as the habitat interior environment, structural subsystem, and ECLSS. These

subsystems interact with each other through sensors and actuators at their interfaces, facilitated by a transfer system that enforces the necessary boundary conditions.

The testbed includes an inflated bladder and structural dome surrounded by thermal transfer panels that impose an exterior thermal boundary condition similar to that experienced by deep-space habitats. Cyber-physical testing plays a crucial role in thermal management, particularly when a hazard such as a meteorite impact occurs on the habitat's surface. This impact can displace the lunar regolith protective layer, resulting in temperature fluctuations within the interior environment. The temperature control system is responsible for managing this disruption.

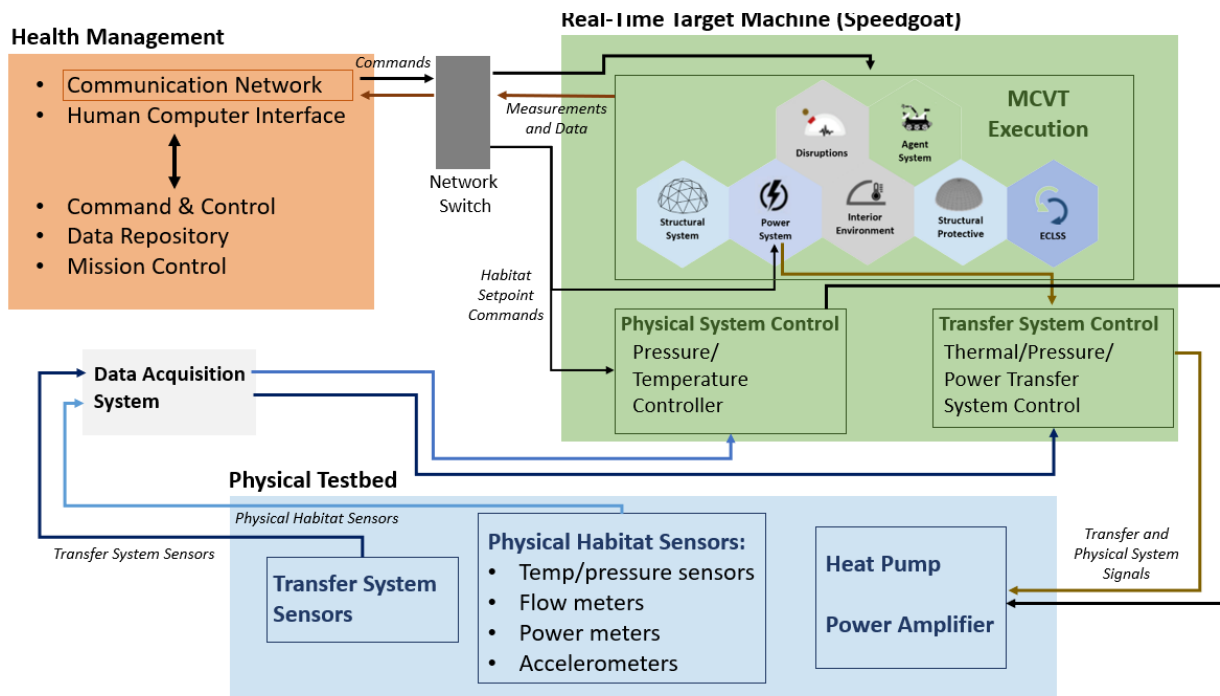


Figure 7- CPT architecture diagram

3. ANALYTICAL HABITAT INTERIOR ENVIRONMENT MODEL

3.1 Analytical Model Description

The Habitat Interior Environment Model (HIEM) developed is a physics-based lumped Simulink model called the HIEM to provide real-time information on the air temperature and pressure within the lunar habitat dome, as indicated in Figure 8. HIEM is designed to accurately account for various thermal and mass flow exchanges over time, and is divided into two zones within the dome, as well as an airlock zone. The development of HIEM proceeded in four phases, starting with the temperature model, followed by the pressure model, and the coupling of the two through mass conservation and energy conservation, and finally the addition of humidity. The temperature model uses a thermal resistance network, as explained in detail in section 3.2. The pressure model was developed in two parts [24]. The HIEM model incorporates ideal air composition and humidity preservation, as well as the transition from continuum flow to molecular flow when the pressure approaches a near-vacuum state. The temperature and pressure models are coupled using a control volume analysis with mass and energy conservation to observe changes under different disturbances. HIEM also considers changes to the thermodynamic state of air caused by neighboring subsystems, and ECLSS provides heating and cooling loads to adjust the temperature and supply and relief inputs to ensure the interior environment remains within an acceptable range.

The HIEM model includes a door that separates the zones inside the habitat, which is represented as either open or closed. However, the model does not capture the dynamics of the system when the door is opened or closed, and HIEM does not incorporate the effects on the temperature of both zones. In addition, the model does not have the CO₂ and O₂ system, which is crucial for regulating the levels of these gases to ensure the health and safety of the crew. The Oxygen Generation System produces oxygen by separating it from other gases, such as nitrogen, and is essential for maintaining human health and survival. The Carbon Dioxide Removal System removes excess CO₂ from the air through a chemical process and prevents it from reaching dangerous levels. Finally, the Air Revitalization System is responsible for maintaining the overall air quality, which includes filtering out contaminants and controlling temperature and humidity levels within the habitat.

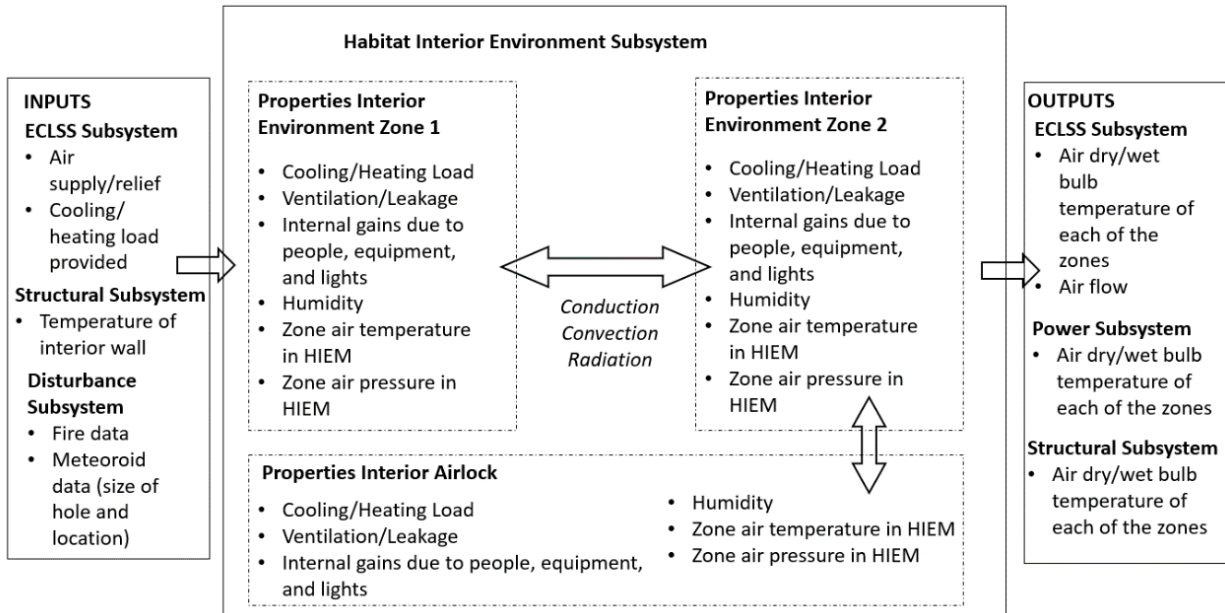


Figure 8-Inputs and outputs of HIEM in MCVT

3.1.1 Habitat Interior Environment Model Disturbances

The simulation of disruptions in MCVT is conducted to assess the resilience of the habitat design, as described in Section 2.3. Among the disruptions considered are fire, meteorite impact, and airlock failure, all of which affect the interior environment. Fire and airlock failure are initiated within HIEM, meaning that the disruption block transmits information about the hazard directly to the subsystem. In the case of a meteorite impact, however, the disturbance information is sent to the structure subsystem, which then provides HIEM with the radius size of the impact, if any.

Fire

The MCVT disruption scenarios consider fire as the only disturbance that originates within the interior environment. A chemical reaction causes the evolution of light and heat in varying intensities through a rapid oxidation process. [25]. The Fire Tetrahedron provides a visual representation of the fundamental components necessary for a fire to occur. These components include fuel, an oxidizing agent (usually oxygen), heat, and an uninhibited chemical reaction. When these four elements are present and in the correct proportion, they create a self-sustaining chemical reaction known as a fire. The heat ignites the fuel, which then reacts with the oxygen to

release energy in the form of light and heat. The uninhibited chemical reaction sustains the fire and allows it to continue until one or more of the components are depleted or removed. [26]. Explosions can be best addressed by preventing them since they are not known to occur over an extended period of time.

The progression of a fire is influenced by a range of factors, including the characteristics of the fuel, the amount of fuel present, the type of ventilation (natural or mechanical), the geometry of the compartment (including volume and ceiling height), the location of the fire, and the ambient conditions such as temperature and wind [25]. The fire curve displayed below illustrates the impact of ventilation limitations on the indoor environment. Figure 9 depicts a fire originating inside a structure. During the initial growth phase of the fire, there is a sufficient amount of oxygen to combine with the heated gases, causing the flame to burn. However, as the oxygen supply within the structure is consumed, the fire begins to diminish, resulting in a decrease in the heat output and temperature. Opening the vents allows for the introduction of oxygen, revitalizing the fire [26]. Oxygen mixes with the heated gas in the structure, and energy levels begin to rise. This change in ventilation can cause the fire to grow rapidly, potentially resulting in a flashover situation (full fire in a fire compartment).

During the growth stage, the fire increases in size from small flaming to a full conflagration that covers the entire room. This may take several seconds to several hours to occur. During the growth phase, flammable gases produced by the burning material are trapped at the ceiling, this combination of gases is augmented by oxygen [27]. The gases that are heated are forced under pressure from the fire's area into areas that aren't involved. When this mixture is burned, short bursts of flame can be observed in the layer of smoke. This condition is called rollover. Rollover should serve as a precursor to flashover in the fire area. As the fire moves through the growing and developed stages, the potential for flashover increases. Flashover is the sudden spread of flames from floor to ceiling as a result of thermal radiation, this causes the flames to spread from room to room [25]. Radiation from the ceiling and walls that bounce back to the room heats the smoke and gases released as a result of the burning materials and the room's contents being combusted.

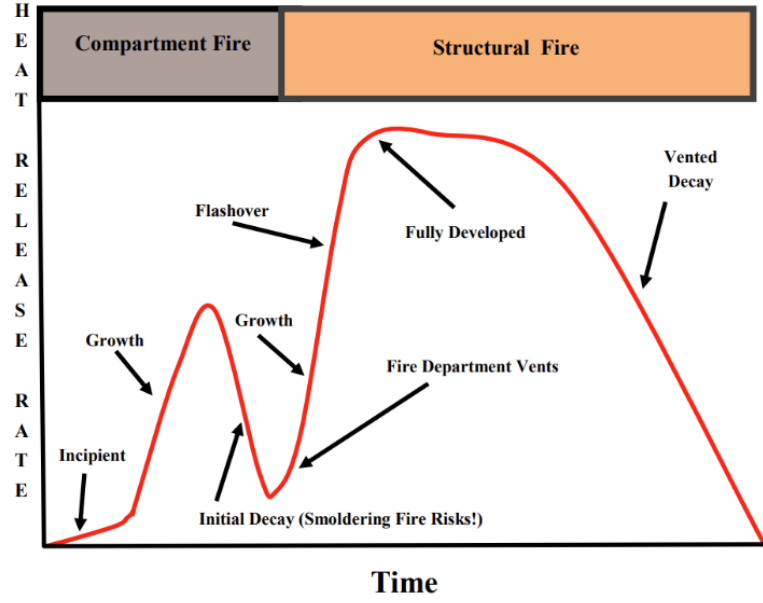


Figure 9-Content fire stages (reproduced from [15])

The goal is controlling the fire before the flashover stage begins which is what is studied in MCVT. The ignition stage can be characterized by the thermal load that is produced through Equation 1 in terms of the burning rate (\dot{m}_f) [25]. Also, the burning area (A_B) with respect to the burning rate per unit area (\dot{m}''_f).

$$\dot{Q} = \dot{m}_f \Delta H_c \quad (1)$$

$$\dot{Q} = \Delta H_c A_B \dot{m}''_f \quad (2)$$

The burning area is characterized by Equation 3 where r_B is the burning radius, V_s flame spread velocity and t is the time [25].

$$A_B = \pi r_B^2 = \pi V_s t \quad (3)$$

All these characteristics of the heat thermal load of fire depend of the material that is burning. It has been parametrized through normalized design factor for fires seen in Figure 10.

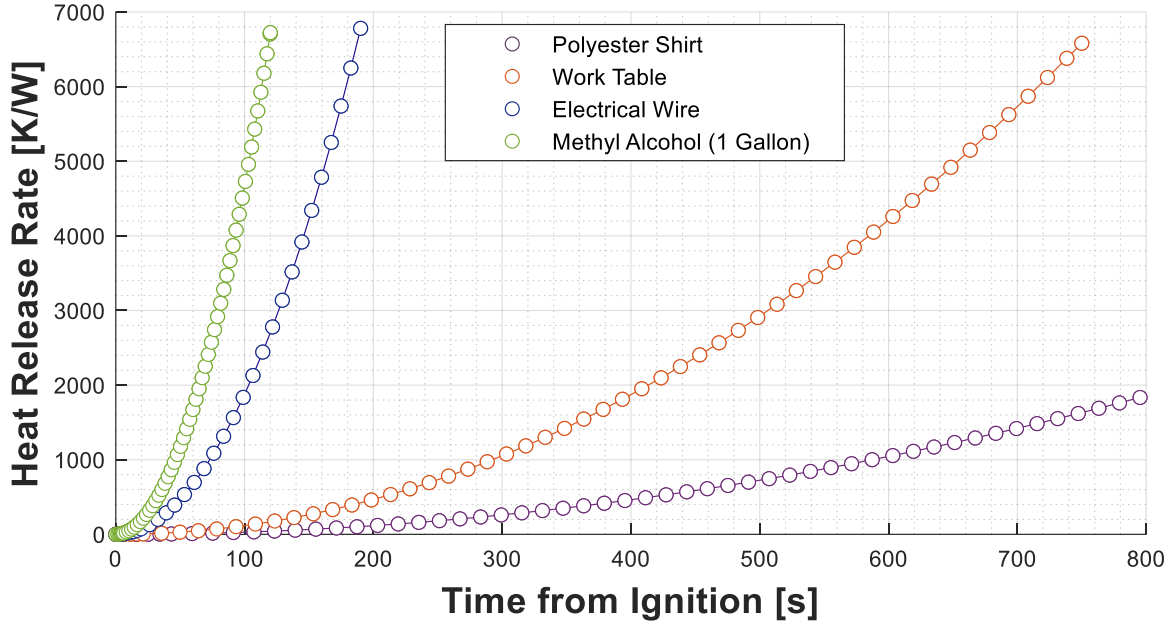


Figure 10-Heat release rate of different fire types (adapted from [16])

Leading to the thermal load released by the fire to be simplified to Equation 4 where α is the heat release rate of fire.

$$\dot{Q} = \alpha t^2 \quad (4)$$

The mass flow rate can be determined by Equation 5 where ρ_a is the interior environment density, g is gravity, E is the entrainment constant (0.2) and H is the height of the entrainment

$$\dot{m}_f = E \left(\frac{g \rho_a^2}{c_p T_a} \right)^{1/3} \dot{Q}^{1/3} H^{5/3} \quad (5)$$

To calculate the smoke temperature it will depend on Equation 6 where c_p the coefficient of pressure, \dot{m}_A air flow of the zone and the T_A the temperature of the zone.

$$T_s = T_A + \frac{\dot{Q}}{\dot{m}_A c_p} \quad (6)$$

The interior environment temperature will vary through Equation 7 which relates the smoke temperature and the previous temperature of the interior environment with its respecting flow rate.

$$T_{HIEM,t+1} = \frac{\dot{m}_{f,t} T_{HIEM,t} + \dot{m}_A \Delta t T_s}{\dot{m}_{f,t+1}} \quad (7)$$

Figure 11 represent the dynamics of a polyester fire as that smoke layer decreases as the temperature of the zone increases exponentially. Once the smoke layer equals zero the flashover stage has begond.

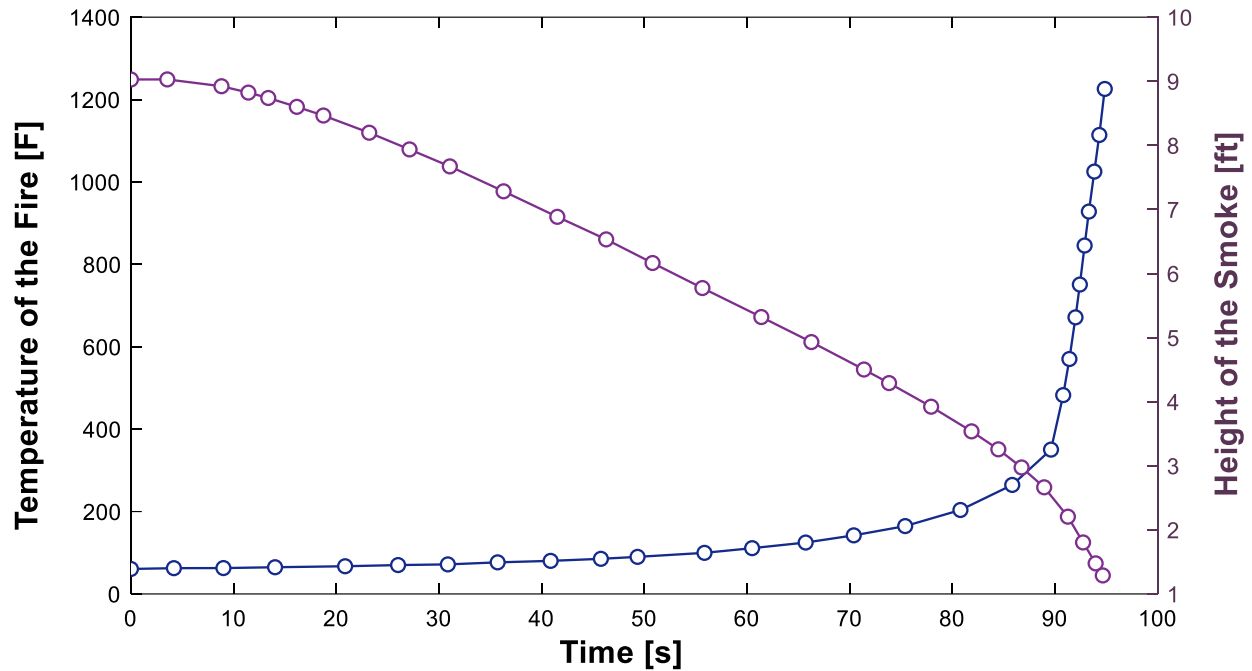


Figure 11- Content fire temperature at ignition stage

As a result of these equations the following types of fires with their corresponding α value are seen in Table 2.

Table 2- Nominal Design Parameter values for fire [28]

Type	Class	α	Units
Polyester Shirt	Slow	0.0029	K/W
Office Desk	Medium	0.0117	K/W
Electrical wires	Fast	0.1876	K/W
Methyl alcohol (1 Gallon)	Ultra-Fast	0.4669	K/W

Meteorite Impact

In the event of a meteorite impact, the disruption is not directly transmitted to the Habitat Interior Environment Model. Instead, a disturbance model is sent to systems that are directly

affected, such as the structural system. The structural subsystem then transmits information about the size of the meteorite impact after it has penetrated through the entire thickness of the habitat's wall. In the interior environment, the impact results in a significant loss of pressure. According to Table 3, full penetration occurs at intensities 4 and 5, which are the only relevant intensities for HIEM. These scenarios have been validated using the MCVT code and the pressure model. [24].

Table 3-Meteorite Impact Disturbances [24]

Intensity Level	Description	Radius size	Units
1	Normal Operations	0.000	m
2	Half penetration through structural protective layer (SPL)	0.000	m
3	Full penetration through SPL, no penetration through structural layer	0.000	m
4	Penetration through SPL and structural layer	0.005	m
5	Penetration through SPL and structural layer	0.008	m

Airlock Failure

The use of airlocks is critical for structures located in high-pressure differential areas, such as in space and marine missions. These airlocks enable individuals and objects to transition gradually from an atmospheric environment on Earth to one with high pressure, and vice versa. In the airlock, occupants enter a chamber where they acclimate to the environment they are about to enter. Additionally, the airlock prevents the interior environment from losing its preset temperature and pressure due to movement in or out of the habitat. The MCVT airlock is based on the Quest Joint Airlock from the International Space Station. Its structure, which consists of a bladder, aluminum, insulation, and steel, has been validated through MCVT [24].

Table 4- Airlock Failure Disturbances [24]

Intensity Level	Description	Radius size	Units
1	Inner door is open and there is a leakage from the outer door	0.002	m
2	Inner door is closed and there is a leakage between the airlock and interior environment	0.002	m

3.2 Development of Habitat Interior Environment Model

3.2.1 Thermal Model

The mechanism by which energy flows into and out of the components of a building structure are seen in Figure 12. The ambient driving forces that produce the instantaneous energy flows entering through the wall and glazing are transient. Internal gains vary over the course of the day as people enter, turn on lights and equipment, and leave. The instantaneous energy flows, termed gains, or losses, interact with the structure and increase or decrease the temperature of the zone air, internal structural mass, and furnishings [29]. The net thermal effect of these gains on the zone air is termed the load, and the interaction among these gains produces a load that is out of phase with the instantaneous heat gain.

Heat is transferred by convection and radiation from the ambient to the exterior of the wall, resulting in a heat flow that is conducted to the interior surface of the wall seen in Figure 12. Convection transfers a portion of the heat flow at the interior surface of the structure subsystem components (\dot{Q}_s) into the zone. Solar energy enters through the \dot{Q}_{sol} fenestration and is absorbed by the surfaces of the internal mass [29]. However, since control volume of the system is the internal wall of the structural subsystem these effects will be neglected. Equipment and people contribute to heat and moisture to the zone air through internal gains \dot{E}_g , and they radiate heat to the internal mass. The internal mass heat is transferred to the zone air by convection. A zone's sensible and latent energy flow into the zone is controlled by the ventilation air \dot{E}_v and infiltration air \dot{E}_{inf} . The model simulates the ventilation load, but the infiltration of air cannot be model until having a physical system. The cooling load $\dot{Q}_{cooling}$ corresponds to the net amount of energy that needs to be removed from the zone just to maintain a specific zone condition [29].

The ECLSS subsystem model has the capability to manage the temperature within the interior environment by supplying cooling and heating loads to keep the temperature within a comfortable range. When the temperature is higher than the upper bound of the setpoint range, ECLSS provides cooling until the temperature is once again within the proper range. When the temperature is lower than the lower bound of the setpoint range, ECLSS will then provide heating. This model will be dependent on the moisture within the interior environment due to internal process and infiltration.

The gains and losses as they relate to cooling and heating are shown in Equation 8. In Equation 8, \dot{L}_T is the total load of the interior environment, \dot{Q}_s is the structural layer gains, \dot{E}_g is the internal gains, \dot{E}_v is the ventilation, \dot{E}_{inf} is the infiltration, and $\frac{dE}{dt}$ is the energy storage within the zone which is illustrated in Figure 12 [29].

$$\dot{L}_t = \dot{Q}_s + \dot{E}_g + \dot{E}_v + \dot{E}_{inf} - \frac{dE}{dt} \quad (8)$$

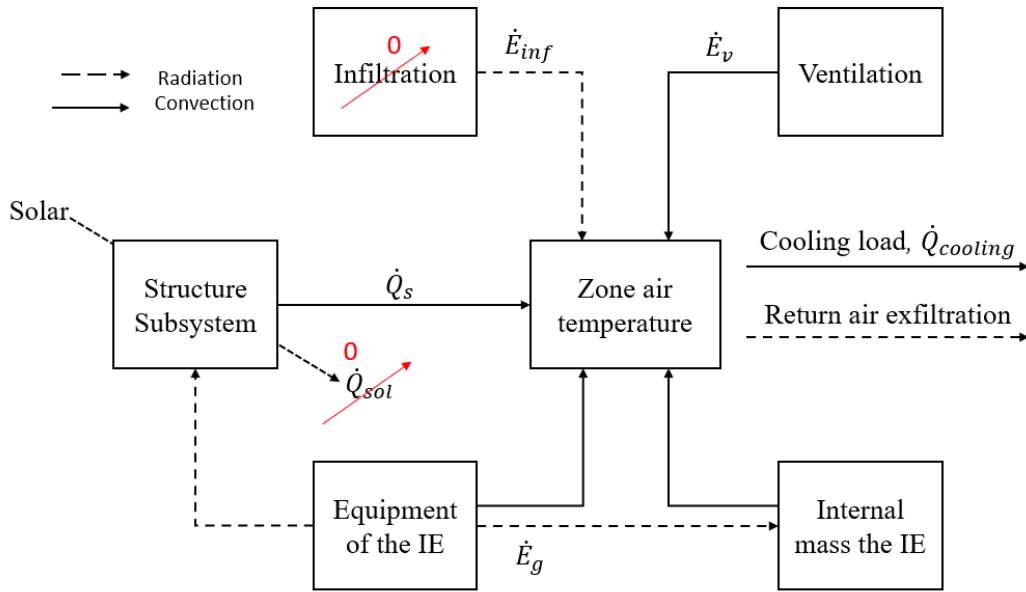


Figure 12-Schematic of the relation between heat flows and loads

The relationship between various terms is demonstrated by Equation 8, which is the starting point for calculation approaches for both the design heating and cooling loads and the seasonal energy requirements. During the cooling season, the cooling load is the sum of the wall, internal, and ventilation energy flows. The energy balance equation also indicates that during the heating season, when the wall and ventilation and infiltration energy flows represent losses, internal gains offset some of the losses and reduce the heating demand. Moreover, thermal storage in the interior can reduce heating and cooling peaks.

The combined effect of thermal storage and time-varying driving forces leads to four energy flows related to sensible cooling, as shown in Figure 13. The instantaneous heat gain is the rate at which energy enters a space and is generated. The sensible cooling load is the rate at which

energy must be removed to maintain the space at a constant temperature. The temperature in a zone air is typically controlled with a thermostat that allows for a temperature range, and the heat extraction rate is the rate at which energy is removed from the space, accounting for the temperature swing. The coil sensible cooling load is the sensible energy removed by the cooling coil servicing the zone and is the sum of the heat extraction rate and additional sensible loads such as duct heat gain or fan energy dissipation. This method is known as the heat balance method and considers heat flows and distributed thermal storage [29].

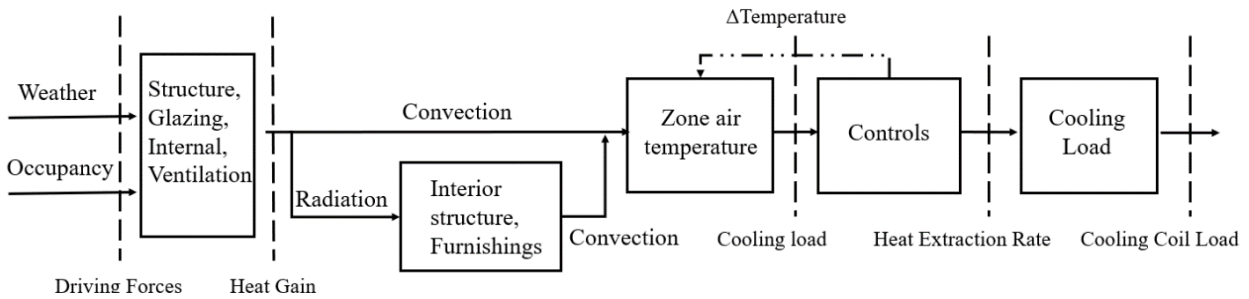


Figure 13- Schematic sensible cooling load calculation process

The zonal air energy balance equation is provided in Equation 9 and seen in Figure 14. It is assumed that the zone air is uniform throughout and negates the zonal air capacitance. $\dot{Q}_{s,c}$, from the structure subsystem, the internal gains and thermal mass, $\dot{Q}_{g,c}$, and sensible energy from the ventilation airflow, $\dot{E}_{v,s}$, and infiltration, \dot{E}_{inf} . The energy flow is balanced by the sensible load, \dot{L}_s , from ECLSS. The instantaneous sensible heat balance for the zone is given in Equation 9.

$$\sum \dot{Q}_{s,c} + \sum \dot{Q}_{g,c} + \dot{L}_s + \dot{E}_{v,s} + \dot{E}_{inf} = 0 \quad (9)$$

The convection from the physical wall structure seen in Figure 14 is assumed to the thermal transfer panel load that is in direct contact with the structure layer and later through conduction it passes the bladder and interacts through convection with the zone air.

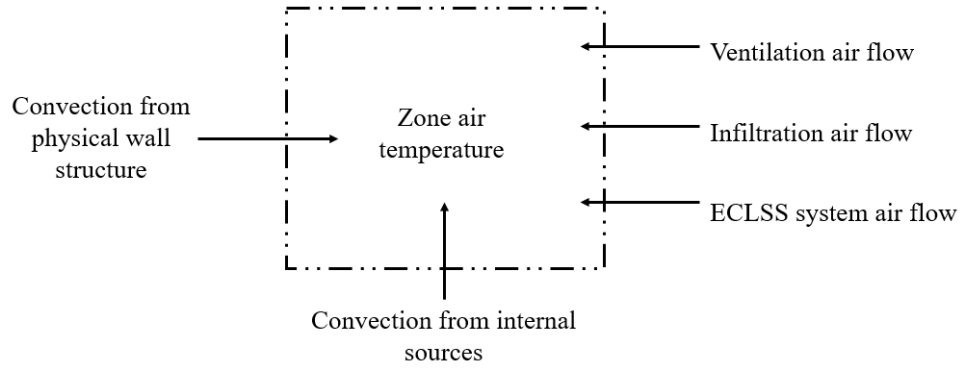


Figure 14- Schematic of zone one air energy flows

The approach of HIEM thermal model is seen in Figure 15 that is the same as in the heat balance and radiant time series methods from Figure 12. The thermal capacitance is represented as a lumped capacitance for the structure and furnishings. Furthermore, to simplify calculations, rather than analyzing the radiant exchanges, the radiant time series method is implemented to separate the radiant portion from the convection portion [29]. For this model it will be incorporated two zone air temperatures that will be interacting with each other through convection as well as an airlock air temperature separated by a series of walls seen in Figure 15 [29].

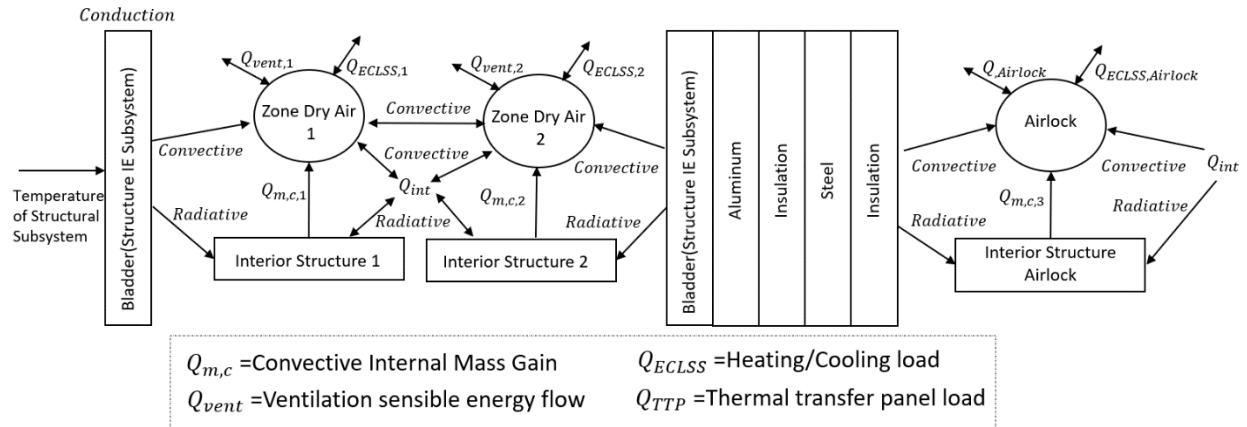


Figure 15-Schematic of heat flows for thermal network approach

The thermal circuit for this model is shown in Figure 6 for a three-zone air (two zones in the habitat and an airlock). The model reads the temperature of the structural subsystem which later has wall of polyester (component the bladder is made). It proceeds with the two-zone air of the habitat. After there is the polyester and the contact with the walls of the airlock. These are

composed of 4 layers of wall (aluminum-insulation-steel-insulation) ending in the zone air of the airlock. The heat flow into the zone from the surface of the wall is determined using the thermal network representation with the resistances and capacitances selected to best represent the element. The T_z is the temperature of the zone air, T_m is the temperature of the internal mass, T_s is the temperature of inner wall of the airlock, $R_{conv,zone}$ is the thermal resistance of the air convection, R_m is the thermal resistance of the internal mass convection, R_{rad} is the thermal resistance of the internal mass radiation, and C_m is the thermal capacitance of the internal mass. The heat gain from the structure is transferred by convection to T_z and by radiation to T_m . The coefficient for the interior surfaces is comprised of convection and radiation coefficients used for respective convection and radiation transfers. The internal sensible gains generated by equipment and individuals and the glazing conductive gains are divided into a convective and a radiative fraction. These fractions cause a difference in temperature between the zonal air and internal mass resulting in convection transferring heat to the zone air.

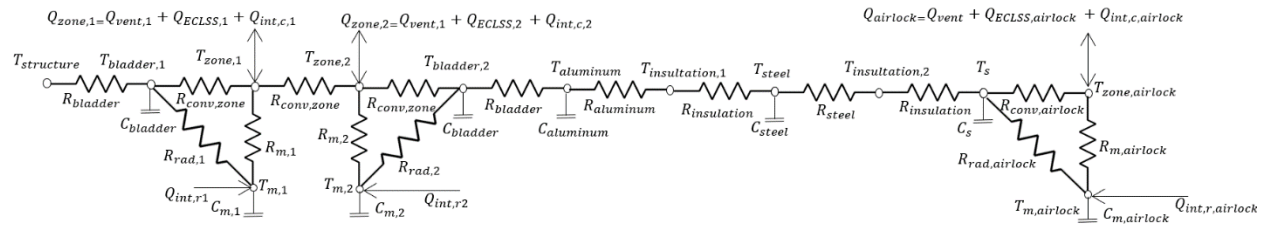


Figure 16-Thermal resistance network of HIEM

For this circuit there are seven relevant energy balances (Equations 10-16). There are three for each of the nodes representing the capacitances in the envelope element and one for the node representing the internal mass. The internal mass will be the same for each zone (i is written in the equation meaning could be 1, 2) [29]. These energy balance yield the node temperature as a function of time. The internal sensible gains due to people, lights and equipment are divided into a convective fraction $F_{g,c}$ and a radiative fraction $F_{g,r}$, that go to the zone air and internal mass, respectively.

$$\frac{dT_{bladder,1}}{dt} = \left(\frac{T_{structure} - T_{bladder,1}}{R_{bladder}C_{bladder}} \right) + \left(\frac{T_{zone,1} - T_{bladder,1}}{R_{conv,zone}C_{bladder}} \right) \quad (10)$$

$$\frac{dT_{bladder,2}}{dt} = \left(\frac{T_{aluminum} - T_{bladder,2}}{R_{bladder}C_{bladder}} \right) + \left(\frac{T_{zone,2} - T_{bladder,2}}{R_{conv,zone}C_{bladder}} \right) \quad (11)$$

$$\frac{dT_{m,i}}{dt} = \left(\frac{T_{zone,i} - T_{m,i}}{R_{m,i}C_{m,i}} \right) + \left(\frac{T_{bladder,i} - T_{m,i}}{R_{rad,i}C_{m,i}} \right) + \frac{\sum F_{g,r}\dot{Q}_g}{C_{m,i}} \quad (12)$$

$$\frac{dT_{m,airlock}}{dt} = \left(\frac{T_{zone,airlock} - T_{m,airlock}}{R_{m,airlock}C_{m,airlock}} \right) + \left(\frac{T_s - T_{m,airlock}}{R_{rad,airlock}C_{m,airlock}} \right) + \frac{\sum F_{g,r}\dot{Q}_g}{C_{m,airlock}} \quad (13)$$

$$\frac{dT_{aluminum}}{dt} = \left(\frac{T_{bladder,2} - T_{aluminum}}{R_{bladder}C_{aluminum}} \right) + \left(\frac{T_{insulation,1} - T_{aluminum}}{R_{aluminum}C_{aluminum}} \right) \quad (14)$$

$$\frac{dT_{steel}}{dt} = \left(\frac{T_{insulation,1} - T_{steel}}{R_{insulation}C_{steel}} \right) + \left(\frac{T_{insulation,2} - T_{steel}}{R_{insulation}C_{steel}} \right) \quad (15)$$

$$\frac{dT_s}{dt} = \left(\frac{T_{insulation,2} - T_s}{R_{insulation}C_s} \right) + \left(\frac{T_{zone,airlock} - T_s}{R_{conv,airlock}C_s} \right) \quad (16)$$

The energy balance on the two zone air equations and the airlock zone air equation, the insulation temperatures yield an algebraic system of equation (Equations 17-21) [29].

$$\begin{aligned} & \frac{T_{bladder,1} - T_{zone,1}}{R_{conv,zone}} + \frac{T_{zone,2} - T_{zone,1}}{R_{conv,zone}} + \frac{T_{m,1} - T_{zone,1}}{R_{m,1}} + \dot{Q}_{ECLSS,1} \\ & + \dot{m}c_p(T_{structure} - T_{zone,1}) + \sum F_{g,c}Q_{g,1} = 0 \end{aligned} \quad (17)$$

$$\begin{aligned} & \frac{T_{bladder,2} - T_{zone,2}}{R_{conv,zone}} + \frac{T_{zone,1} - T_{zone,2}}{R_{conv,zone}} + \frac{T_{m,2} - T_{zone,2}}{R_{m,2}} + \dot{Q}_{ECLSS,2} \\ & + \dot{m}c_p(T_{structure} - T_{zone,2}) + \sum F_{g,c}Q_{g,2} = 0 \end{aligned} \quad (18)$$

$$\frac{T_s - T_{zone,airlock}}{R_{conv,airlock}} + \frac{T_m - T_{airlock}}{R_{m,airlock}} + Q_{ECLSS,airlock} + \sum F_{g,c}Q_{g,airlock} = 0 \quad (19)$$

$$\frac{T_{aluminum} - T_{ins,1}}{R_{aluminum}} + \frac{T_{steel} - T_{ins,1}}{R_{insulation}} = 0 \quad (20)$$

$$\frac{T_{steel} - T_{ins,2}}{R_{steel}} + \frac{T_s - T_{ins,2}}{R_{insulation}} = 0 \quad (21)$$

Energy flows due to ventilation and infiltration

The word ventilation is used to describe the flow of natural air that is intended to be introduced into a building to improve the air quality. The word infiltration is employed to describe the unplanned airflows that enter or exit a building, such as the accidental passage of air through cracks around doors or joints between structural elements [29]. The airflow influences the building's energy loss or gain, because outdoor air enters the building at its ambient temperature, while it leaves at a zone temperature. The energy required to condition the air that is infiltrated and vented is an additional burden on the ECLSS system.

Airflow through the vents is regulated in order to meet the requirements of comfort and health, and it's a significant component of the load. Infiltration flows are typically small compared to ventilation flows and can therefore be disregarded when calculating heat loss or gain.

The energy gain from cooling and dehumidifying or heating and humidifying these flows from the ambient to zone conditions is given as the product of flow rate and enthalpy difference between ambient and zone [29]. Do to modeling a lunar habitat conditions the difference would be from the structural subsystem to the zone assuming complete insulation with the exterior beyond the structural subsystem. Assuming an average airflow (\dot{V}) of 20 CFM in Equation 22 which corresponds the ventilation system of the ISS being crew [30]. In Equation 22 ρ_{air} is the density of the air h_a is the enthalpy of the air and h_z the enthalpy of the zone.

$$L_v = \dot{V} * \rho_{air}(h_a - h_z) \quad (22)$$

Thermal resistance and capacitance

The resistances and capacitors parameters used in calculating the air temperature within the interior environment is summarized in Table 5. The resistance of the materials is calculated using thermal conductivity specification from literature [31][32],[33]. The internal mass parameters are calculated with respect to the floor area of each of the zones with respect to the unit thermal resistance and capacitor [29].

Table 5- Key thermal resistance and unit thermal capacitance values [29], [31]–[33]

Parameter	Value	Units
Thermal resistance for convection, $R_{conv,zones}$	0.025-0.325	[hr-ft ² -°F/Btu] & [W/m ² -K]
Thermal resistance for internal mass, R_{rad}	1.08	[hr-ft ² -°F/Btu] & [W/m ² -K]
Thermal resistance for internal mass, R_m	1.84	[hr-ft ² -°F/Btu] & [W/m ² -K]
Unit bladder thermal capacitance, $C_{m,bladder}$	1.9	[Btu/ ft ² -°F] & [W/m ² -K]
Unit zones thermal capacitance, C_m	10	[Btu/ ft ² -°F] & [W/m ² -K]
Unit aluminum thermal capacitance, C_m	3.18	[Btu/ ft ² -°F] & [W/m ² -K]
Unit steel thermal capacitance, C_m	1.68	[Btu/ ft ² -°F] & [W/m ² -K]

In the case of natural convection resistance to calculate the heat transfer coefficient will vary depending on the temperature difference from the medias. The heat transfer coefficient used in Equation 23 is found using the Nusselt number (Equation 24). The Nusselt number is the ratio of heat transfer by convection and conduction [34]. This ratio can be correlated to the Rayleigh number for a fluid's natural convection. Equation 25 shows the equation of the Rayleigh number as a product of the Grashof number (Equation 26) and Prandtl (Equation 27). The Grashof number is an approximate ratio of buoyancy to viscous forces on a fluid while the Prandtl number is the ratio of momentum diffusivity and thermal diffusivity [34].

$$h = \frac{Nu * k_{air}}{L} \quad (23)$$

$$Nu = 0.26 * Ra^{1/3} \quad (24)$$

$$Ra = Gr * Pr \quad (25)$$

$$Gr = \frac{L^3 * \rho_{air}^2 * g * \Delta T * \alpha_{air}}{\nu_{air}} \quad (26)$$

$$Pr = \frac{\nu_{air} * c_{v,air}}{k_{air}} \quad (27)$$

In Equations 23-27, k_{air} is the thermal conductivity of air ($W/m - K$), L is the characteristic length (m), ρ_{air} is the density of air (kg/m^3), g is the gravitational acceleration of the moon (m/s^2), ΔT is the difference of temperatures (K), α_{air} is the thermal expansion coefficient, ν_{air} is viscosity of the air ($N - s/m^2$).

Internal thermal gains

The primary sources of internal thermal gains in a lunar habitat are expected to be humans, equipment, appliances, and lighting systems. These internal processes can help to cool the habitat in high ambient temperatures and offset heating during low temperatures. Heat transfer from people and equipment occurs primarily through convection to the interior air and radiation to the surrounding surfaces.

Humans produce heat and moisture through metabolic processes [35] The amount of influence will depend on the activity that person is doing. Table 6 shows average values for women and men engaged in different activities the corresponding unit gain (U_{gain}). For calculation purposes it was assumed that the humans inside the interior environment will be performing moderate office work as it is the most common activity will be done by astronauts in the Gateway [35].

Table 6- Thermal gains due to human activity [36]

Activity	Unit Latent	Unit Sensible	Units
Rest	105	245	Btu/hr
Light office work	155	245	Btu/hr
Moderate office work	200	250	Btu/hr
Heavy office work	275	275	Btu/hr
Light physical work	475	275	Btu/hr
Moderate physical work	675	375	Btu/hr
Heavy physical work	870	580	Btu/hr

Table 7 shows the appliances and equipment also contribute that also contribute to the heat gain.

Table 7- Thermal gains due to equipment [36]

Activity	Unit Latent	Unit Sensible	Units
Equipment Type	500-1200	50-100	W
Desktop computer	50-130	10-35	W
Laptop computer	250-400	20-40	W
Monitor	600	120	W
Microwave	-	5000	W
Electric stove	800	50	W
Refrigerator	500-1200	50-100	W

The maximum power that equipment can draw is referred to as the name plate power, while the recommended heat gain is the value used in design calculations. In cases where a detailed equipment description is not available (as seen in Table 7), general load density values from Table 8 can be used. These values are based on the assumption of medium activity within the interior environment. Lighting systems are known to contribute significantly to thermal gain, and advances in fluorescent lights and ballasts have helped reduce energy consumption. The typical energy intensities for illumination range from 0.5 to 2 W/ft² of floor area, as shown in Table 8 for average load density in typical office spaces.

Table 8- Average load density [36]

Activity	Unit Latent	Units
Light	0.5	W/ft ²
Medium	1.0	W/ft ²
Medium/heavy	1.5	W/ft ²
Heavy	2.0	W/ft ²
Level of activity	0.5	W/ft ²
Light	1.0	W/ft ²

Table 9 provides the interior environment conditions and their corresponding radiative and convective fractions. It is noteworthy that radiative fractions are generally twice as much as convective fractions. Therefore, the radiant heat transfer from a wall surface to internal mass is approximately twice the convective heat transfer from the surface to the air.

Table 9- Fractions for radiative and convective heat flows [29]

Source of Heat Flow	Radiative Fraction ($F_{g,r}$)	Convective Fraction ($F_{g,c}$)
Occupants	0.6	0.4
Walls	0.63	0.37
Equipment	0.1-0.4	0.6-0.9
Incandescent Lighting	0.8	0.2

The energy flow due to illumination can be substantial, and the proportion of radiation and convection depends on factors such as whether the lighting fixture is recessed or suspended, and whether it is ventilated with supply and/or return air. The fraction of radiation and convection for equipment varies widely, and it is recommended to use higher radiation factors for equipment with higher surface temperatures. Furthermore, the radiant fraction for occupants is greatly influenced by the ventilation of the interior environment.

The internal gains, Q_g , due to lights, people, and equipment (i) are determined through Equation 28 & 29 assuming that there are two crew members where U_i represents the unit latent load of either lights, people, or equipment.

$$\dot{Q}_{g,l} = 2 * A_{floor} * U_i \quad (28)$$

$$\dot{Q}_{g,people} = 2 * U_i \quad (29)$$

Assuming standard conditions, with the interior habitat temperature maintained at 25 °C (77 °F), the addition of one person in each zone with equipment and medium light systems, and airlock only equipment and lighting, results in notable temperature increases, as shown in Figure 17. It appears that humans contribute significantly to the temperature increase, which will have a significant impact on the crew and non-crew members.

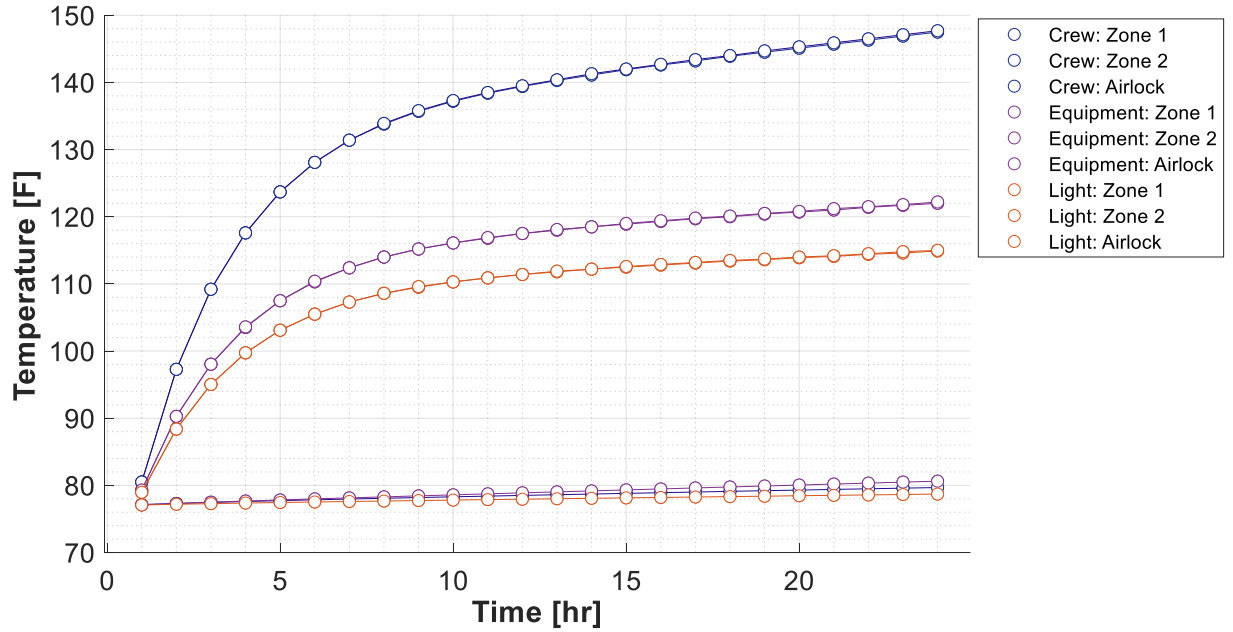


Figure 17- HIEM temperatures with different internal gains

3.2.2 Pressure Model

In normal conditions or through a fire disturbance, the habitat interior environment pressures are calculated through by means of ideal gas equation.

$$P = \frac{m}{MM} \frac{\bar{R}T}{V} \quad (30)$$

Equation 30 is the pressure, m is the mass of air (g), MM is the molar mass of air (gmol^{-1}), \bar{R} is the universal gas constant ($\text{K}^{-1}\text{mol}^{-1}$), T is the interior environment temperature (K), and V is the volume of the interior environment (m^3).

Air leakage for meteorite disturbances

If an impact by a meteorite or any other form of pressure release happens, a trapped mass of pressurized air in the fluid will flow through the downhole drill string or fluid line system, creating a slug of air. This concept stems from the Helmholtz resonator, fluid flow change, and resonance instability[37]. It can be assumed that there is no net flow of the air slug and that the interior pressure is uniform. It is also worth noting that these slugs have been observed in microgravity conditions [37].

Pressure variations are calculated using the method of Jaffe [38]. This method was created to predict the pressure fluctuations in buildings with one or multiple openings that are low-rise or have multiple openings during a tornado, the inspiration for this method came from Jeong Hee Oh [39]. The equation that is used to model this pressure's dynamic is derived from Bernoulli's equation for an unsteady fluid that travels along a streamline, the equation is presented in Equation 31. The equation assumes that the fluid is incompressible, viscous, and isothermal, where ρ is the fluid density, U is the flow velocity, P is the fluid's pressure, g is gravitational acceleration, and z is the height.

$$\rho \int_1^2 \frac{\partial U}{\partial t} ds + \int_1^2 dP + \int_1^2 \frac{1}{2} \rho (U_2^2 - U_1^2) + \rho g(z_2 - z_1) = 0 \quad (31)$$

Combining the concept of Bernoulli's equation with the idea of an air slug results in a single-degree-of-freedom mass-spring damping system that is illustrated in Equation 32 [38]. In this equation, the air slug is considered to be mass which depends on, ρ is the density of air, C_L is the loss coefficient through the opening, P_e is the external pressure, \dot{x} is the air slug velocity, \ddot{x} is the acceleration of the air slug.

$$\rho l_e \ddot{x} + C_L \rho \frac{\dot{x}|\dot{x}|}{2} = P_e - P_i \quad (32)$$

To study a single meteorite hit with full penetration into the interior environment or a single leakage Equation 33 is adapted to Equation 34 where l_e is effective length of air slug (m), V_0 internal volume of building, γ is the ratio of specific heat of air, A is the area of the opening, P_o is static pressure and \dot{P}_i^j is the j^{th} time derivative of internal pressure, P_i^j is the internal pressure, and P_e^j is j^{th} time step of the external pressure or the moon's atmospheric pressure. Previous of pressure analysis and validation to the MCVT lunar habitat have assumed the following set of parameters (Table 10) [24].

Table 10- Parameters of dynamic pressure [24]

ρ	V_0	γ	P_o	C_L	l_0	P_e^j
1.23 kg/m^3	32 m^3	1.4	10^5 Pa	2.5	0.6 m	$3 \times 10^{-10} \text{ Pa}$

The area of the opening is assumed to be circular and is calculated using the value of the radius provided by the structural subsystem[24]. The effective length of air slug, l_e , is calculated in meters using Equation 33, where l_0 is the structural wall thickness.

$$l_e = l_0 + 0.89\sqrt{A} \quad (33)$$

The mass flow leaving the system for the dynamic pressure is calculated through Equation 34 [24].

$$\dot{m} = c_d \cdot A \cdot \sqrt{2 \cdot \rho \cdot (P_1 - P_2)} \quad (34)$$

3.2.3 Coupling of Thermal Model and Pressure Model

To maintain the thermal and pressure interactions in the air, or the zone as referred to in the zonal modeling approach, the lumped air node is replaced with a system that incorporates two-way coupling between temperature and pressure. [40]. The control volume analysis considers the space enclosed by the inner surfaces of the interior environment as a control volume. Using this approach, two fundamental conservation principles, namely mass and energy, can be analyzed.[41]. Starting with the conservation of mass Equation 35 where m_{cv} is the mass of the air inside the control volume, and \dot{m}_i and \dot{m}_e are the entering and exiting mass flow rate of the air crossing the boundary of the control volume.

$$\frac{dm_{cv}}{dt} = \sum_i \dot{m}_i - \sum_e \dot{m}_e \quad (35)$$

It's assumed that the volume of the interior environment is practically confined by the walls, is constant. Then, the mass of the interior habitat is a function of density only, resulting in Equation 36 where, V_{cv} is the volume of the interior air, and ρ is the density of the interior air.

$$V_{cv} \frac{d\rho}{dt} = \sum_i \dot{m}_i - \sum_e \dot{m}_e \quad (36)$$

For the conservation of energy Equation 37 is used where E_{cv} is the energy in the control volume, \dot{Q}_{cv} is the heat transfer rate added to the control volume, \dot{W}_{cv} is the rate of the boundary work done (e.g., deformation of the boundary), h is the enthalpy of the air, V is the velocity of air, g is the gravitational acceleration, and z is the height at which mass transfer through the boundary

occurs. Subscript i and e indicate whether the properties are for entering or exiting the control volume.

$$\frac{dE_{cv}}{dt} = \dot{Q}_{cv} - \dot{W}_{cv} + \sum_i \dot{m}_i \left(h_i + \frac{V_i^2}{2} + gz_i \right) - \sum_e \dot{m}_e \left(h_e + \frac{V_e^2}{2} + gz_e \right) \quad (37)$$

This can be further simplified by assuming the kinetic and potential energy, and boundary work terms to be negligible [42] as well as a constant control volume, resulting into Equation 38 where u is the internal energy of the interior air. Also, only assuming one inlet and outlet.

$$V_{cv} \frac{d(\rho u)}{dt} = \dot{Q}_{cv} + \dot{m}_i h_i - \dot{m}_e h_e \quad (38)$$

Conservation laws to be explicit with enthalpy and pressure for gas tank pressurization and heat exchanger modeling respectively, the similar approach can be taken by using Equation 39 [43] & [44].

$$\frac{\partial \rho}{\partial t} = \left(\frac{\partial \rho}{\partial h} \right)_P \frac{dh}{dt} + \left(\frac{\partial \rho}{\partial P} \right)_h \frac{dP}{dt} \quad (39)$$

Since density is a function of enthalpy and pressure, Equation 38 can be rearranged to explicitly represent enthalpy and pressure on the left-hand side, as shown in Equation 40.

$$LHS \text{ of (4)} = V_{cv} \frac{d(\rho u)}{dt} = V_{cv} \frac{d(\rho h - P)}{dt} = V_{cv} \left(\rho \frac{dh}{dt} + h \frac{\partial \rho}{\partial t} - \frac{\partial P}{\partial t} \right) \quad (40)$$

Equation 40 is combined with the relationship described in to produce the final expression of the conservation of energy explicit in enthalpy and pressure. The resulting expression is Equation 41.

$$V_{cv} \left[\rho + h \left(\frac{\partial \rho}{\partial h} \right)_P \right] \frac{dh}{dt} V_{cv} + \left[h \left(\frac{\partial \rho}{\partial P} \right)_h - 1 \right] \frac{dP}{dt} = \dot{Q}_{cv} + \dot{m}_i h_i - \dot{m}_e h_e \quad (41)$$

Similarly, the conservation of energy, the conservation of mass expression, Equation 36, can be written in terms of enthalpy and pressure as Equation 42.

$$V_{cv} \left(\frac{\partial \rho}{\partial h} \right)_P \frac{dh}{dt} + V_{cv} \left(\frac{\partial \rho}{\partial P} \right)_h \frac{dP}{dt} = \dot{m}_i - \dot{m}_e \quad (42)$$

The two resulting equations, Equation 41 & 42, are to be solved simultaneously at each timestep during the simulation.

3.3 Analytical Verification of Thermal Habitat Interior Environment Subsystem

The temperature range specified in the MCVT documentation, which is 10 to 40 °C (equivalent to 50 to 104 °F), refers to the temperature range of the structure in contact with the interior environment in normal conditions [6]. This temperature range is determined by the conditions of the moon and the temperature that the structure can reach. Deviations from this range can affect the performance of the system, such as damage to the system when the temperature is too high.

Understanding the effect of structural temperature variation on the interior environment is crucial for evaluating and ensuring stable temperature-sensitive processes. Running the code at different temperatures and observing the results provides valuable insight into the performance of the interior environment. This information can help inform decisions about the design and operation of the the MCVT system and its components to ensure optimal performance and reliability.

To assess the performance of the interior environment with respect to structural temperature variation, the code was run at five different structural temperatures (50°F, 68°F, 77°F, 86°F, and 104°F) as shown in Figure 18. The setpoint temperature (initial condition) of 77°F was used as the reference temperature, and it was observed that the temperature remained constant at this setpoint. As the temperature deviated from the setpoint temperature, the temperature changed in a parabolic manner before stabilizing.

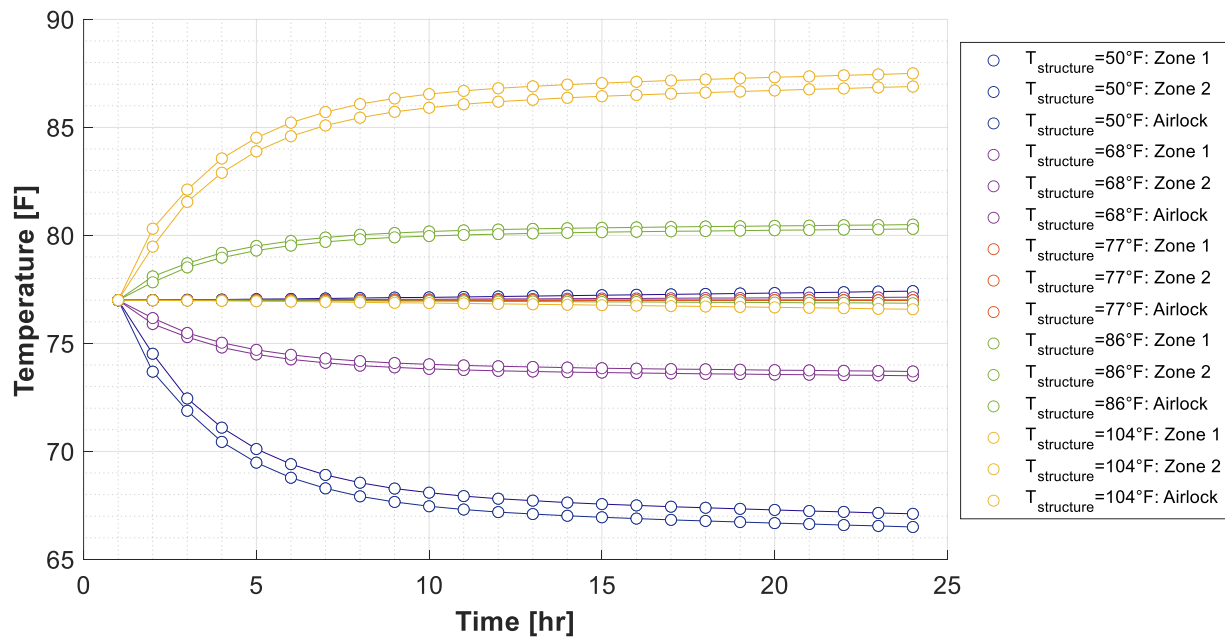


Figure 18-Responds of HIEM to changing temperature in the structure

Fluctuations in the temperature of the structure can affect the temperature of the airlock. However, the airlock is designed with insulation (as shown in Figure 18) to maintain a constant temperature. This ensures that the temperature of the airlock remains stable despite changes in the zone temperature.

To ensure the accuracy and reliability of the zonal model, it is important to validate the data obtained through multiple analytical methods. The Engineering Equation Solver (EES) code was compared to MATLAB as an additional analytical method to validate the zonal model. This involves comparing the results obtained from one method with those obtained from another method, which can help identify potential errors or biases in the original method.

Both EES and MATLAB are computational methods used for modeling and simulation. EES is specifically designed for solving and analyzing engineering problems, particularly those involving thermodynamics and energy systems. It includes a simple, spreadsheet-like interface and a built-in equation solver that can handle non-linear equations and perform parametric studies. EES also includes a large library of thermodynamic and transport property functions.[45].

MATLAB is a numerical computing environment and programming language that provides tools for data analysis, visualization, and simulation [46]. It includes a wide range of mathematical and engineering functions and provides a powerful scripting language for custom analysis and modeling. MATLAB also has a large community of users who share code, algorithms, and tools, making it a popular choice for engineers and scientists.

In conclusion, both EES and MATLAB are effective computational tools. In order to validate the system, the optimal step size needs to be determined for both methods to generate identical solutions, which is achieved with a step size of 0.08 for both as seen in Figure 19.

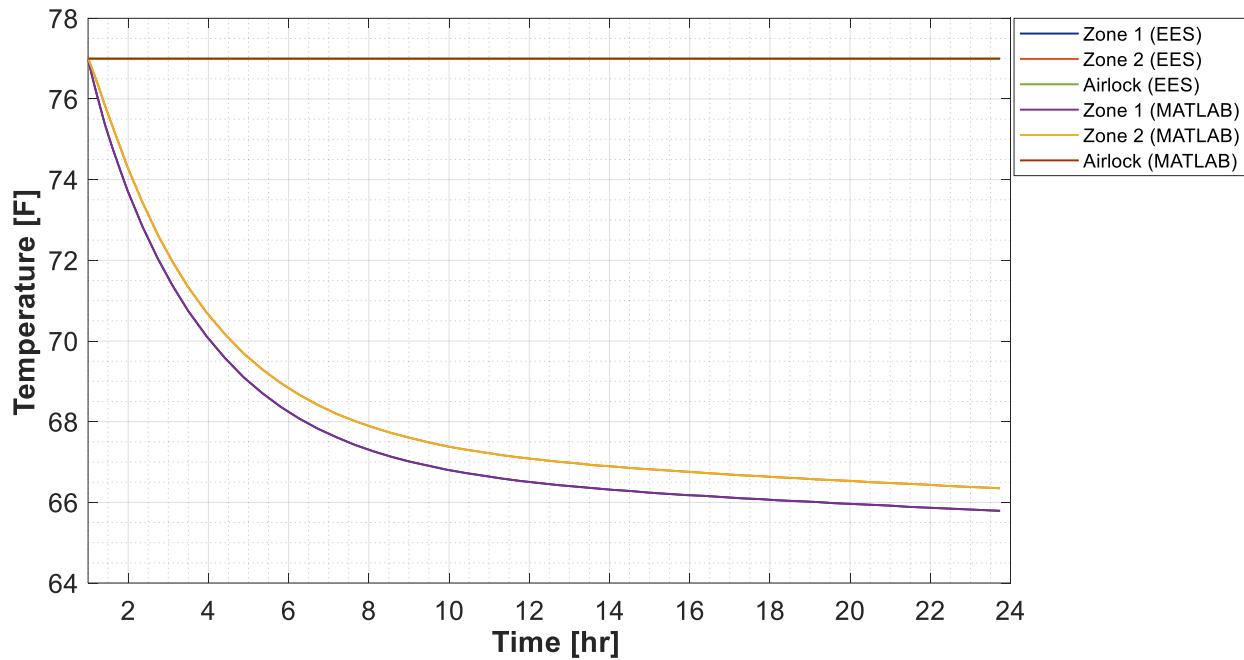


Figure 19- Verification through MATLAB of HIEM model in EES

3.4 Fire Case Study of Thermal Transfer Model

Fire is the only hazard that can be initiated in the interior environment and produce complete failure of the lunar habitat therefore failure of the mission. The different types of fire that were studied are discussed in Section 3.1.1. It is emphasized that fire can only be controlled in its ignition phase before a flashover occurs. To ensure the resilience of the lunar habitat, the hazard must be controlled within the ignition stage.

The information also highlights that the ignition stage time decreases as the combustion rate of the material increases, which is illustrated in Figure 20. A case study of the lunar habitat is presented, where a fire starts in zone 1 at a setpoint temperature of 77°C (77°F). As the combustion rate of the materials increases, the temperature in the zone increases faster.

This information provides insight into the importance of controlling fire as a hazard in the lunar habitat and highlights the need to understand the different types of fire and their combustion rates. This knowledge can help to inform decisions about the design and operation of the lunar habitat and its components to ensure the safety and reliability of the mission

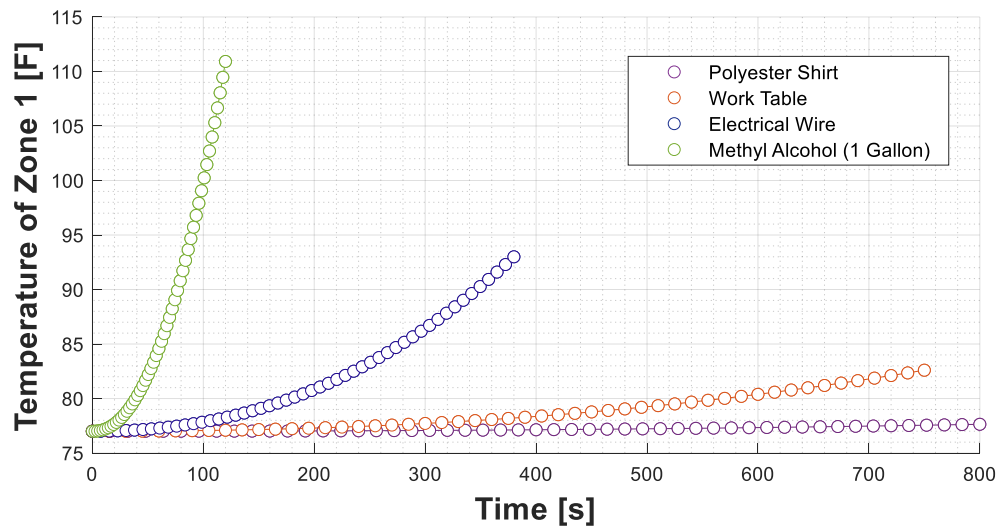


Figure 20- Responds to temperature in zone 1 with different fires

The other zones of HIEM could be affected by this hazard. Figure 21 shows the comparison between a light fire and the most extreme fire, and it is observed that the temperature in zone 2 is similar to that of zone 1. In the polyester case, the offset between the two zones reaches a maximum of 0.6°F at the end of the ignition stage, while in the case of methyl alcohol, the offset is 2.2°F. It is noted that the airlock temperature remains constant in both cases, indicating that the fire has no influence on it. This information highlights the importance of understanding the behavior of fire and its effect on different zones in the lunar habitat and how it can be controlled to ensure the safety and reliability of the mission.

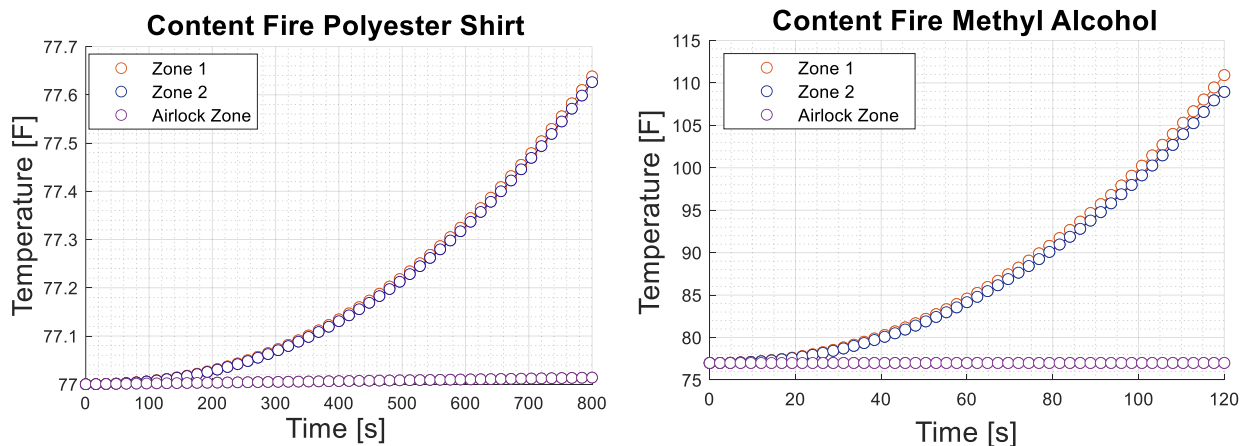


Figure 21-Temperatures of HIEM with respect to fire with respect to polyester (left) and alcohol (right)

3.4.1 Design optimization of the door between zones

To prevent the lunar habitat from complete failure, a door is proposed to be added to divide the two zones. To better understand the capabilities of the MCVT (Modular Coupler Virtual Testbed), a simple standard door design and an optimum door design are presented. The simple door design is chosen based on the standards of regular doors on Earth, while the optimum door design is selected based on the results obtained from the HIEM.

This information highlights the importance of considering the design of the lunar habitat components and how they can contribute to ensuring the safety and reliability of the mission. The proposed door design is intended to provide additional protection against fire hazards and help to prevent complete failure of the lunar habitat. By using the results obtained from the MCVT and the HIEM, the best possible door design can be selected to ensure the safety and success of the mission.

To conduct the analysis, the thermal resistance network in Section 3.2.1 needs to be modified as shown in Figure 22. In particular, the two zones will be separated by a physical door instead of allowing free convection between them. This means that the resistance due to convection is replaced by the resistance due to the door. The value that will change between the designs of the door will be the resistance value of the door (R_{door}).

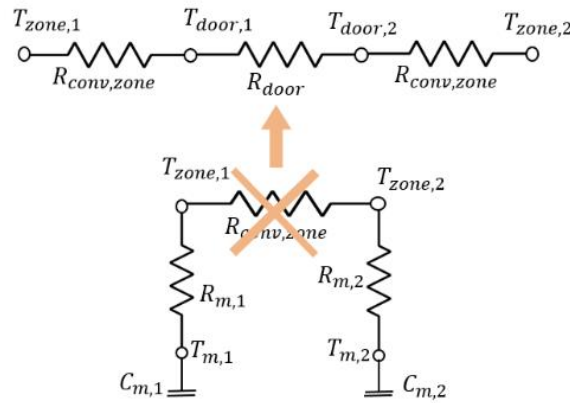


Figure 22- Modification to the thermal resistance network

To design the door, there some parameters that cannot be modified. For instance, the height and the width of the door need to reach the top and the sides of HIEM seen in Figure 23. The variable parameters will be the thickness and the material that is constructed.

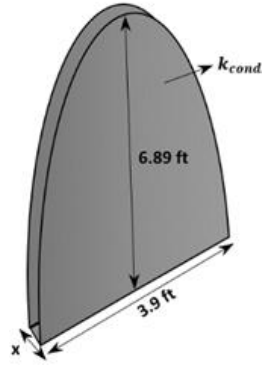


Figure 23- Door schematic

The simple design will follow standard door measurements so it will correspond with a thickness (x) of 0.78 ft (0.2377 m). It will be made out of aluminum with a thermal conductivity ($k_{cond.}$) of 247 W/m-k (142.78 Btu/hr-ft-°F). Following Equation 43 this leads to a thermal resistance of the door of 0.000128 Btu/hr-ft-F (0.000234 W/m-K).

$$R_{door} = \frac{x}{A_s k_{cond.}} \quad (43)$$

Figure 24 shows the results when the fire starts at zone 1 and the door is shut. The temperature of Zone 2 decreases by 3.08°F (-16.62°C). However, the new temperature is outside the comfort zone of the HIEM 64.4°F to 80.5°F (18°C to 26.9°C), with a value of 108.5°F (42.5°C).

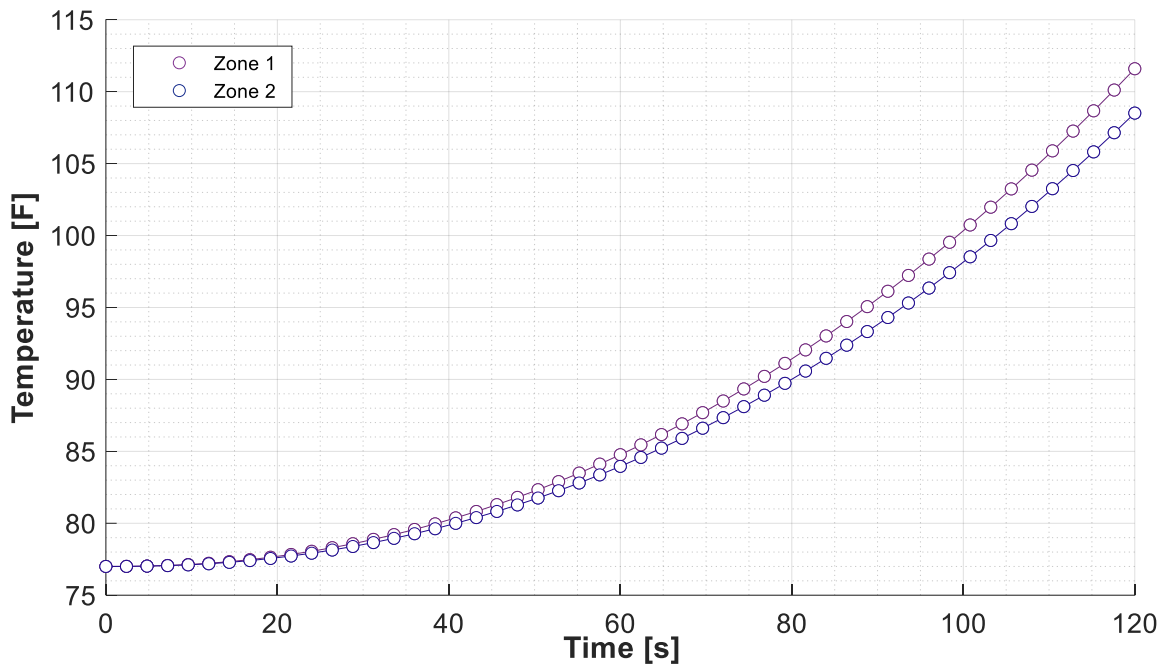


Figure 24- Standard door with methyl alcohol fire starting in zone 1

To find the optimum door the temperature of zone 2 can't exceed 80.5F which leads to the resistance value of the door to be a minimum 8 as Figure 25 shows. The temperature difference between zones at the end of the fire stage is 54.3F with a temperature of zone two of 80.4F.

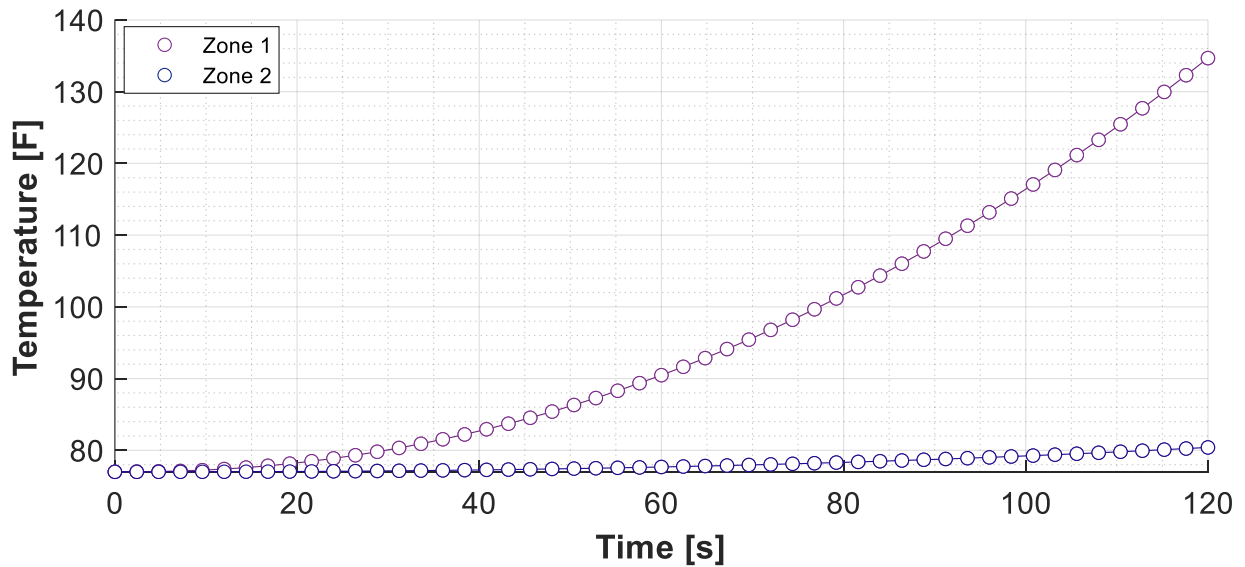


Figure 25- Optimum door with methyl alcohol fire starting in zone 1

To be able to reach that resistance value with the same material as the simple study case the door would need a thickness of 4866.24 ft which is bigger than the habitat. If a simple insulation material issue ($k_{cond}= 0.019 \text{ W/m} \cdot \text{K}$) would be 12.5 ft. It is proposed to use aerospace insulation material [47] with a $K_{cond}= 0.0086 \text{ W/m} \cdot \text{K}$ which would allow for only a thickness of 1.14 ft.

This case study highlights the importance of carefully considering the materials used in the construction of the lunar habitat, as well as their thermal properties. The use of aerospace insulation material allows for a more resilient habitat, capable of handling disturbances such as fire without compromising the safety and comfort of the astronauts. The HIEM provides a tool for studying these kinds of disturbances and helps ensure that the lunar habitat is built to withstand the harsh conditions of space.

4. CYBER-PHYSICAL TESTBED:DESIGN AND CHARACTERISTICS

4.1 Objectives

In order to validate the analytical computational model for the interior habitat presented in Chapter 3, the design of a Cyber-Physical Testbed (CPT) is needed. The CPT replicates some subgroups that were included in MCVT. Specifically, the physical subgroups that are replicated in the CPT include the structural subsystem and the interior environment, with the former being realized through an aluminum structure that provides necessary strength and stability to the habitat (as depicted in Figure 26, top right), and the latter being realized through the use of a bladder made from polyester that creates a livable interior environment with controlled air pressure and temperature (as depicted in Figure 26, top left). Additionally, thermal transfer panels are used to replicate disturbances subsystem to the exterior layer subsystem of the habitat (which would be regolith), as shown in the bottom two pictures of Figure 26.

The validation testing of the Habitat Interior Environmental Model (HIEM) using the Cyber-physical testbed (CPT) will be conducted in three parts. Test A will specifically focus on the bladder and the mini-split heating, ventilation, and air conditioning unit, wherein the normal conditions with just the bladder will be evaluated. The objectives of this test are to validate the CPT code for the Interior Environment (IE) by introducing a specific heating or cooling load through the heat pump system into the bladder and to compare the experimental temperatures and pressures within the IE to those predicted by the CPT HIEM model. This will enable the adjustment of the resistance and capacitor of the bladder in the code to match the physical bladder, thereby ensuring accuracy and reliability in the simulation. A schematic of the system is presented in Figure 27.

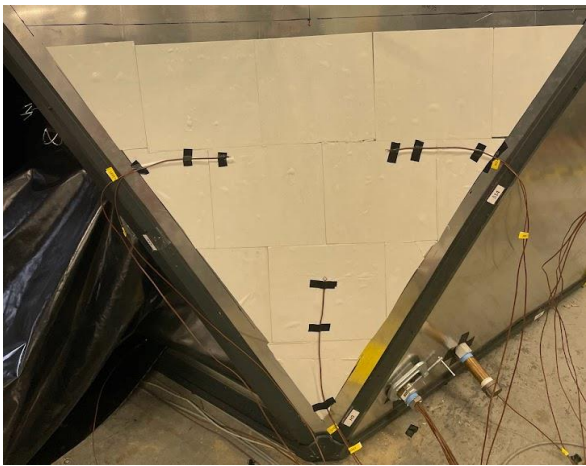


Figure 26- Layers of the CPT testbed structural subsystem (top left), the habitat interior environment subsystem (top right) and the exterior layer subsystem and disturbance subsystem (bottom left and right)

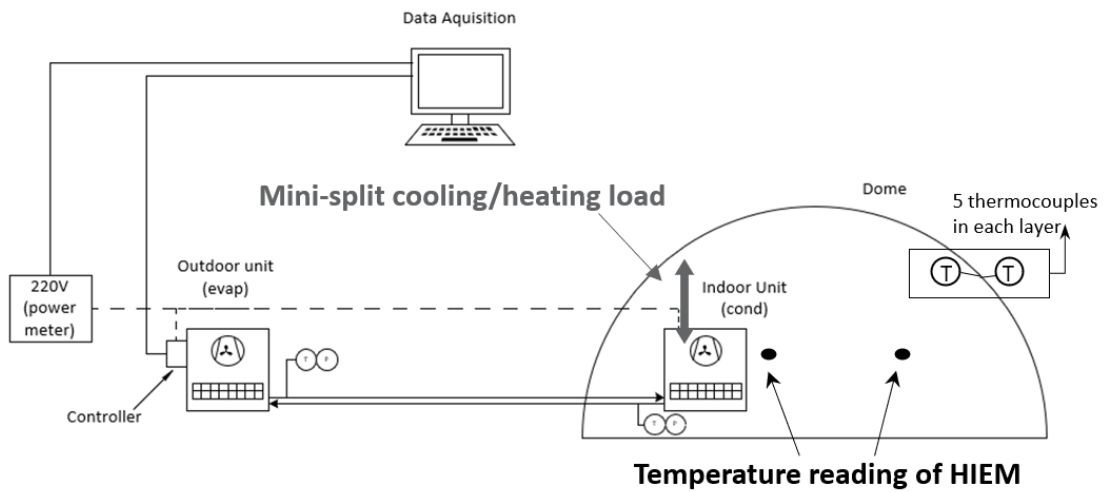


Figure 27-Diagram of Testbed A for validating the normal conditions of the interior environment

The second part of the experimental validation (Test B) focus on characterizing the heat transfer and loss through the different layers of the dome configuration (as illustrated in Figure 28). This step will involve adjusting the thermal resistance, capacitance, and thermal interface material of the structure, as well as the air gaps between the layers, from the structure to the bladder. The aim of this test is to optimize the heat transfer and insulation properties of the habitat's design.

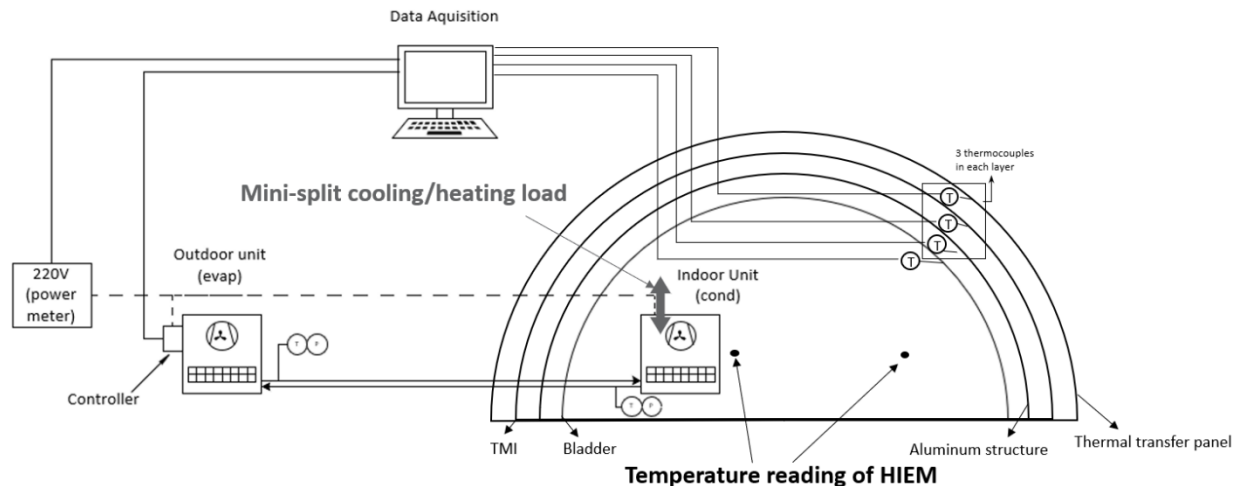


Figure 28-Diagram of the Testbed B of validating the normal conditions of the interior environment

Once optimization of the thermal resistance and capacitance of the physical system have been completed, the third part of the validation testing (Test C, as shown in Figure 29) will involve attaching the thermal transfer panel with Syltherm to the structure. This will introduce a specific heat load to the interior environment, and the temperature changes of the different layers, as well as the air zone temperature, will be measured and compared to the results obtained from the code. The results of this comparison will be used to validate the accuracy of the thermal simulation and to refine the thermal performance of the habitat's design. However, due to manufacturing delays, this experiment was not completed fully. Nonetheless, the loads of the thermal transfer panel were predicted that would go into the interior environment.

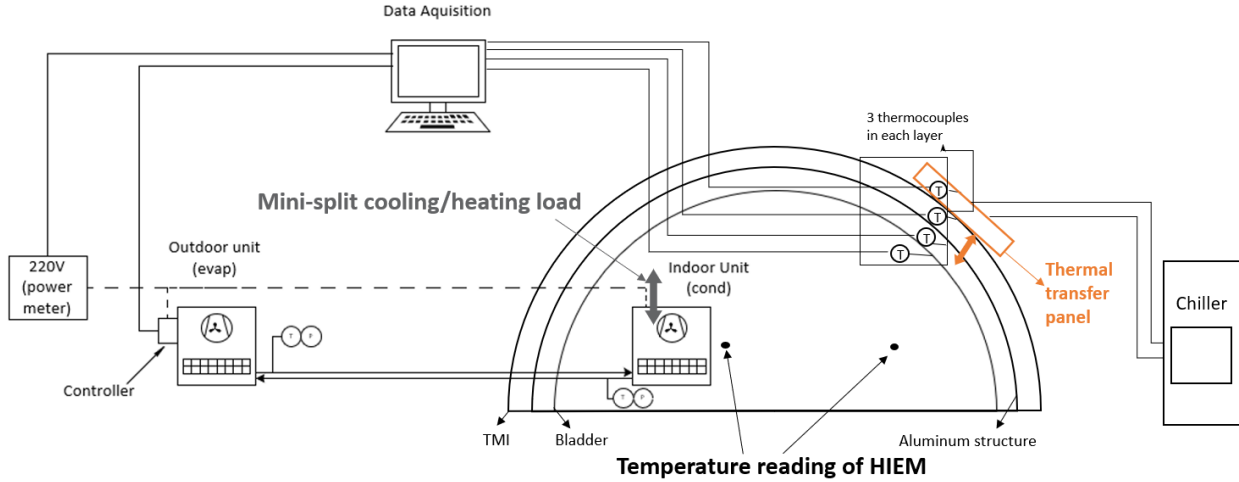


Figure 29-Diagram of the Testbed C of validating the normal conditions of the interior environment

4.2 Cyber physical testbed code

The MCVT HIEM model was modified to incorporate the bladder with a volume of 162.1 ft³ to meet the standards of the CPT HIEM. To accomplish this, a new thermal network was established based on the materials and dimensions used in the dome structure. The zonal air energy balance equation is represented by Equation 44 and illustrated in Figure 30, assuming that the zonal air is uniform throughout and neglecting the zonal air capacitance. It assumes that the zonal air is uniform throughout and neglects the zonal air capacitance. The energy flow is composed of $\dot{Q}_{s,c}$ from the structure subsystem, $\dot{Q}_{g,c}$ from the internal gains and thermal mass, and $\dot{E}_{v,s}$ and \dot{E}_{inf} from the ventilation airflow and infiltration, respectively. This energy flow is balanced by the sensible load \dot{L}_s from the mini-split system.

$$\sum \dot{Q}_{s,c} + \sum \dot{Q}_{g,c} + \dot{L}_s + \dot{E}_{v,s} + \dot{E}_{inf} = 0 \quad (44)$$

In order to verify the dynamics of the code, it is divided into three distinct steps. The first testing phase is performed with the bladder as a boundary condition, whereby the energy flow from the interior environment up to the outside temperature of the bladder is calculated. In Test B, the thermal resistance network is expanded to include the system of Test A, all the way up to the outside layer of the aluminum thermal transfer panel. Finally, Test C involves the complete system, including the load produce by the Syltherm.

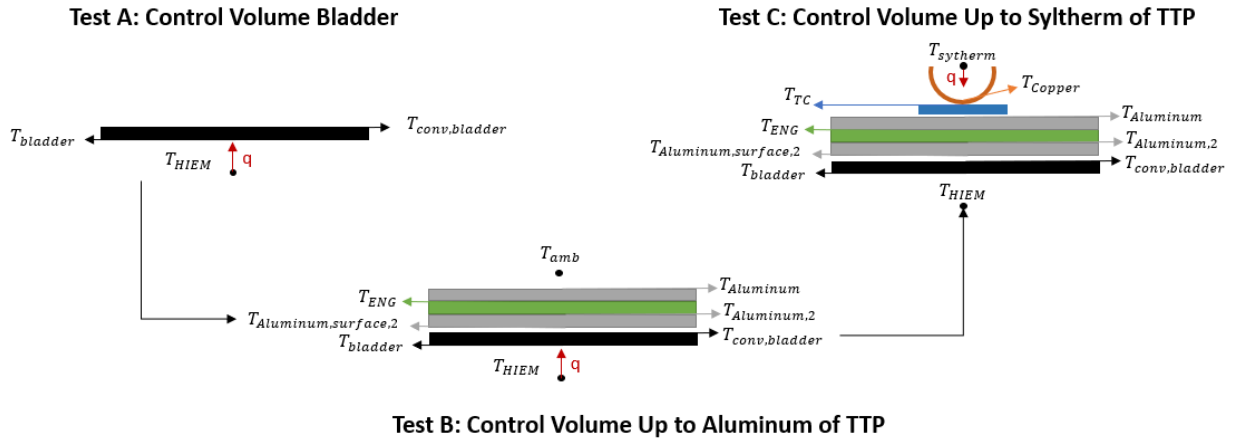


Figure 30-Testing scenarios HIEM CPT code

4.2.1 Cyber-physical testbed model: Test setup A

Due to the structure layer on top, the bladder is not in contact with the ambient air. The temperature of the bladder varies from the outside to the inside of the dome through conduction of the material of the bladder, which in this case is Nylon TPU. The temperature of the air inside the dome interacts with the bladder temperature through convection, resulting in the transfer of heat and energy between the bladder and the air. Maintaining the two zone model from the MCVT HIEM. This process is depicted in Figure 31.

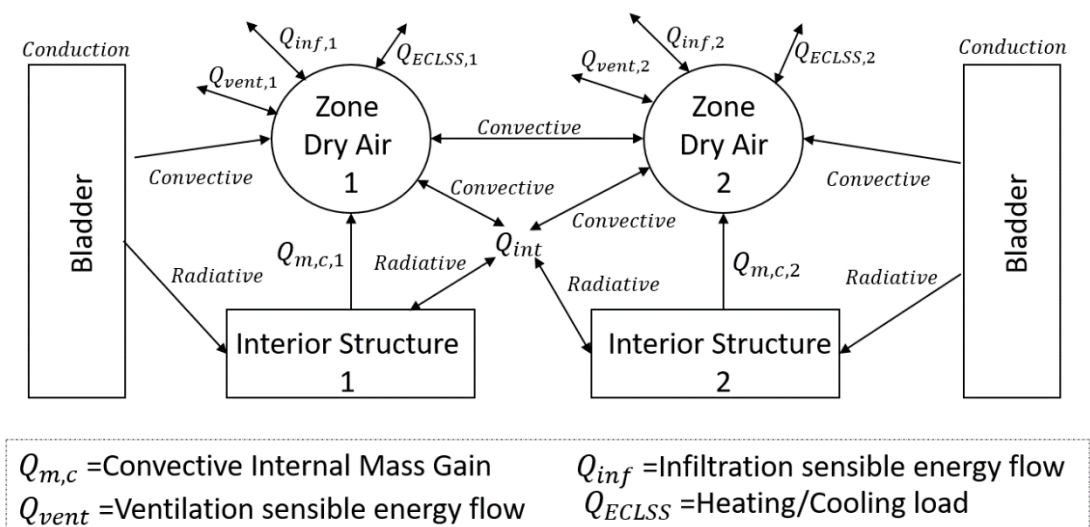


Figure 31- Diagram of heat transfer of Test A

The thermal network utilized for the heat balance and radiant time series method is depicted in Figure 32. This network represents the elements and connections involved in Figure 31.

The following thermal resistance network leads Equations 45-56 where i represents it can be related to zone 1 or zone 2.

$$\frac{dT_{m,1}}{dt} = \left(\frac{T_{bl,in,5} - T_{m,1}}{R_{rad,1}C_{m,1}} \right) + \left(\frac{T_{air,1} - T_{m,1}}{R_{m,1}C_{m,1}} \right) + \frac{\Sigma F_{g,r}Q_g}{C_{m,1}} \quad (45)$$

$$\frac{dT_{m,2}}{dt} = \left(\frac{T_{bl,in,3} - T_{m,2}}{R_{rad,2}C_{m,2}} \right) + \left(\frac{T_{air,2} - T_{m,2}}{R_{m,2}C_{m,2}} \right) + \frac{\Sigma F_{g,r}Q_g}{C_{m,2}} \quad (46)$$

$$\frac{dT_{bl,out,5}}{dt} = \left(\frac{T_{bl,in,5} - T_{bl,out,5}}{R_{bl}C_{bl,out,5}} \right) + \left(\frac{T_{bl,out,4} - T_{bl,out,5}}{R_{bl}C_{bl,out,5}} \right) \quad (47)$$

$$\frac{dT_{bl,out,4}}{dt} = \left(\frac{T_{bl,in,4} - T_{bl,out,4}}{R_{bl}C_{bl,out,4}} \right) + \left(\frac{T_{bl,out,5} - T_{bl,out,4}}{R_{bl}C_{bl,out,4}} \right) \quad (48)$$

$$\frac{dT_{bl,out,3}}{dt} = \left(\frac{T_{bl,in,3} - T_{bl,out,3}}{R_{bl}C_{bl,out,3}} \right) + \left(\frac{T_{bl,out,1} - T_{bl,out,3}}{R_{bl}C_{bl,out,3}} \right) \quad (49)$$

$$\frac{dT_{bl,out,2}}{dt} = \left(\frac{T_{bl,in,2} - T_{bl,out,2}}{R_{bl}C_{bl,out,2}} \right) + \left(\frac{T_{bl,out,1} - T_{bl,out,2}}{R_{bl}C_{bl,out,2}} \right) \quad (50)$$

$$\frac{dT_{bl,out,1}}{dt} = \left(\frac{T_{bl,in,3} - T_{bl,out,1}}{R_{bl}C_{bl,out,1}} \right) + \left(\frac{T_{bl,in,1} - T_{bl,out,1}}{R_{bl}C_{bl,out,1}} \right) + \left(\frac{T_{bl,out,2} - T_{bl,out,1}}{R_{bl}C_{bl,out,1}} \right) \quad (51)$$

$$\frac{dT_{bl,in,5}}{dt} = \left(\frac{T_{bl,out,5} - T_{bl,in,5}}{R_{bl}C_{bl,in,5}} \right) + \left(\frac{T_{bl,in,4} - T_{bl,in,5}}{R_{bl}C_{bl,in,5}} \right) + \left(\frac{T_{air,1} - T_{bl,in,5}}{R_{conv}C_{bl,in,5}} \right) + \left(\frac{T_{m,1} - T_{bl,in,5}}{R_{rad1}C_{bl,in,5}} \right) \quad (52)$$

$$\frac{dT_{bl,in,4}}{dt} = \left(\frac{T_{bl,out,4} - T_{bl,in,4}}{R_{bl}C_{bl,in,4}} \right) + \left(\frac{T_{bl,in,5} - T_{bl,in,4}}{R_{bl}C_{bl,in,4}} \right) + \left(\frac{T_{air,1} - T_{bl,in,4}}{R_{conv}C_{bl,in,4}} \right) \quad (53)$$

$$\frac{dT_{bl,in,3}}{dt} = \left(\frac{T_{air,2} - T_{bl,in,3}}{R_{conv}C_{bl,in,3}} \right) + \left(\frac{T_{m,2} - T_{bl,in,3}}{R_{m,2}C_{bl,in,3}} \right) + \left(\frac{T_{bl,in,1} - T_{bl,in,3}}{R_{bl}C_{bl,in,3}} \right) \quad (54)$$

$$\frac{dT_{bl,in,2}}{dt} = \left(\frac{T_{air,2} - T_{bl,in,2}}{R_{conv}C_{bl,in,2}} \right) + \left(\frac{T_{bl,in,1} - T_{bl,in,2}}{R_{bl}C_{bl,in,2}} \right) + \left(\frac{T_{bl,out,2} - T_{bl,in,2}}{R_{bl}C_{bl,in,2}} \right) \quad (55)$$

$$\frac{dT_{bl,in,1}}{dt} = \left(\frac{T_{bl,in,2} - T_{bl,in,1}}{R_{bl}C_{bl,in,1}} \right) + \left(\frac{T_{air,2} - T_{bl,in,1}}{R_{conv}C_{bl,in,1}} \right) + \left(\frac{T_{bl,in,3} - T_{bl,in,1}}{R_{bl}C_{bl,in,1}} \right) + \left(\frac{T_{bl,out,1} - T_{bl,in,1}}{R_{bl}C_{bl,in,1}} \right) \quad (56)$$

The energy balance on the zone air equations (i being 1 or 2) gives Equation 57 & 58.

$$\frac{(T_{bl,in,4} - T_{air,1})}{R_{conv}} + \frac{(T_{bl,in,5} - T_{air,1})}{R_{conv}} + \frac{(T_{m,1} - T_{air,1})}{R_{m,1}} + \frac{(T_{air,2} - T_{air,1})}{R_{conv}} + \sum F_{g,c} Q_g + Q_{cooling} + \dot{m}_v c_p (T_{amb} - T_{air,1}) + \dot{m}_{inf} c_p (T_{amb} - T_{air,1}) = 0 \quad (57)$$

$$\frac{(T_{bl,in,3} - T_{air,2})}{R_{conv}} + \frac{(T_{bl,in,1} - T_{air,2})}{R_{conv}} + \frac{(T_{bl,in,2} - T_{air,2})}{R_{conv}} + \frac{(T_{m,2} - T_{air,2})}{R_{m,2}} + \frac{(T_{air,1} - T_{air,2})}{R_{conv}} + \sum F_{g,c} Q_g + Q_{cooling} + \dot{m}_v c_p (T_{amb} - T_{air,1}) + \dot{m}_{inf} c_p (T_{amb} - T_{air,1}) = 0 \quad (58)$$

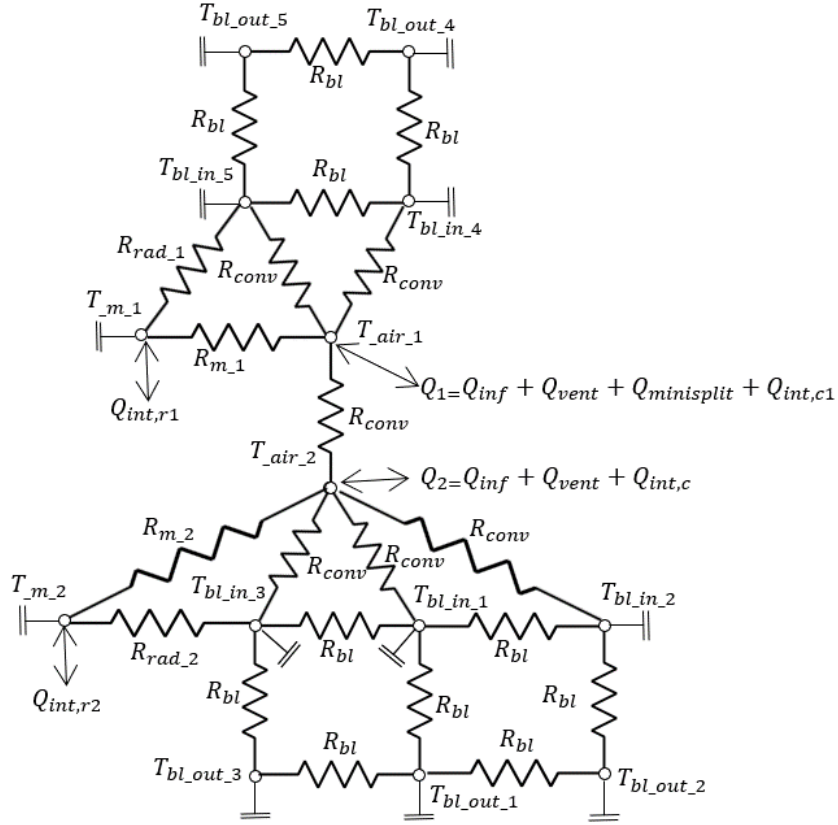


Figure 32-Thermal resistance network for Test A

The conductivity resistance is calculated using equation 59 with the determine parameters for each component where d is the thickness of the material, k the thermal conductivity coefficient of the material and A is the surface area.

$$R_{cond} = \frac{d}{kA} \quad (59)$$

The resistance for convection is calculated through Equation 60 where h is the thermal convection coefficient.

$$R_{conv} = \frac{1}{hA} \quad (60)$$

Reduced Model

The conductivity resistance between each of the sensors is depicted in Figure 32, but considering all the details precisely poses a challenge. To address this, certain assumptions were made. Instead of considering the conductivity from each of the sensors in each layer, the average temperature at each layer is assumed, and only the relationship from layer to layer is considered instead of the conduction of each layer. With this assumption, the thermal network is reduced, resulting in Figure 33.

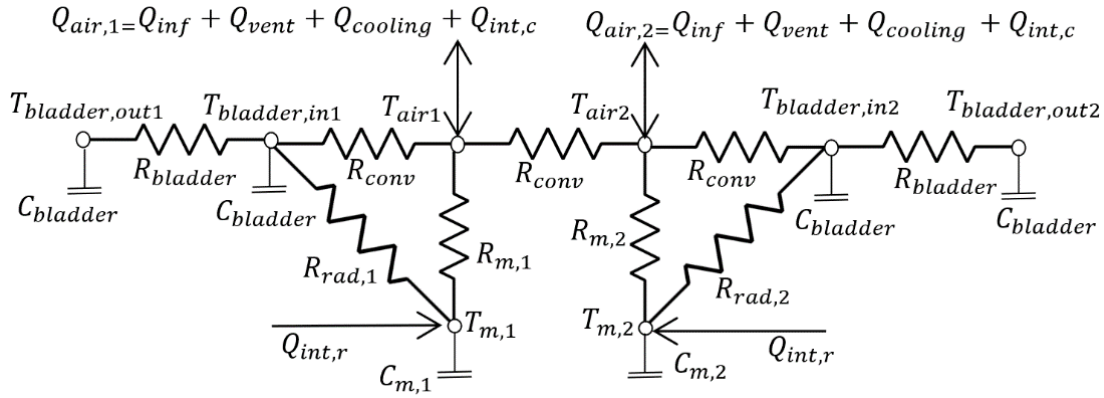


Figure 33- Reduced thermal resistance network for Test A

The following thermal resistance network leads Equations 61-63 where i represents it can be related to zone 1 or zone 2.

$$\frac{dT_{m,i}}{dt} = \left(\frac{T_{air,i} - T_{m,i}}{R_{m,i}C_{m,i}} \right) + \left(\frac{T_{bladder,in} - T_{m,i}}{R_{rad,i}C_{m,i}} \right) + \frac{\sum F_{g,r}Q_g}{C_{m,i}} \quad (61)$$

$$\frac{dT_{bladder,in,i}}{dt} = \left(\frac{T_{bladder,out,i} - T_{bladder,in,i}}{R_{bladder}C_{bladder}} \right) + \left(\frac{T_{air,i} - T_{bladder,in,i}}{R_{conv}C_{bladder}} \right) \quad (62)$$

$$\frac{dT_{bladder,out,i}}{dt} = \left(\frac{T_{bladder,in,i} - T_{bladder,out,i}}{R_{bladder} C_{bladder}} \right) \quad (63)$$

The energy balance on the zone air equations (i being 1 or 2) gives Equation 64 & 65.

$$\frac{(T_{bladder,in,1} - T_{air,1})}{R_{conv}} + \frac{(T_{m,1} - T_{air,1})}{R_{m,1}} + \frac{(T_{air,2} - T_{air,1})}{R_{conv}} + \sum F_{g,c} Q_g + Q_{cooling} + \dot{m}_v c_p (T_{amb} - T_z) + \dot{m}_{inf} c_p (T_{amb} - T_z) = 0 \quad (64)$$

$$\frac{(T_{bladder,in,2} - T_{air,2})}{R_{conv}} + \frac{(T_{m,2} - T_{air,2})}{R_{m,2}} + \frac{(T_{air,1} - T_{air,2})}{R_{conv}} + \sum F_{g,c} Q_g + Q_{cooling} + \dot{m}_v c_p (T_{amb} - T_z) + \dot{m}_{inf} c_p (T_{amb} - T_z) = 0 \quad (65)$$

4.2.2 Cyber-physical testbed model: Test setup B

Once the characterization of the bladder is completed then it is proceeded to understand the heat transfer between all the different layers. The system is composed of the layers seen in Figure 34.

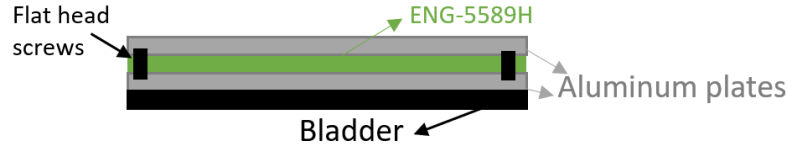


Figure 34-Diagram of the layers of the CPT

The calculations for heat transfer between the layers will make the following assumptions: the Syltherm temperature is constant, there is a constant thermal conductivity coefficient, and a uniform heat flux from the Syltherm. The system will be assumed to be at steady-state conditions, with two-dimensional conduction and negligible heat transfer from the sides of components. The properties will be assumed to be constant, and there will be negligible radiation exchange with surroundings [29].

The dimensions measured of the components and thermal conductivity coefficient are:

- Bladder: Surface area ($A_{bladder}$) 3.3911m², a thickness ($d_{bladder}$) of 0.00001 m, and thermal conductivity ($k_{bladder}$) of 0.24 W/mK.
- Aluminum Structure: Surface area ($A_{aluminum}$) 0.89989 m², a thickness ($d_{aluminum}$) of 0.00001 m and thermal conductivity ($k_{aluminum}$) of 180W/m-K

- ENG-5589H: Surface area (A_{ENG}) 0.89989 m² a thickness (d_{ENG}) of 0.0015 m and thermal conductivity (k_{ENG}) of 2 W/m-K
- Aluminum Plate: Surface area ($A_{aluminump}$) 0.89989 m², a thickness ($d_{aluminump}$) of 0.00001 m and thermal conductivity ($k_{aluminump}$) of 92 W/m-K

With the previous assumptions the following thermal network is created seen in Figure 35.

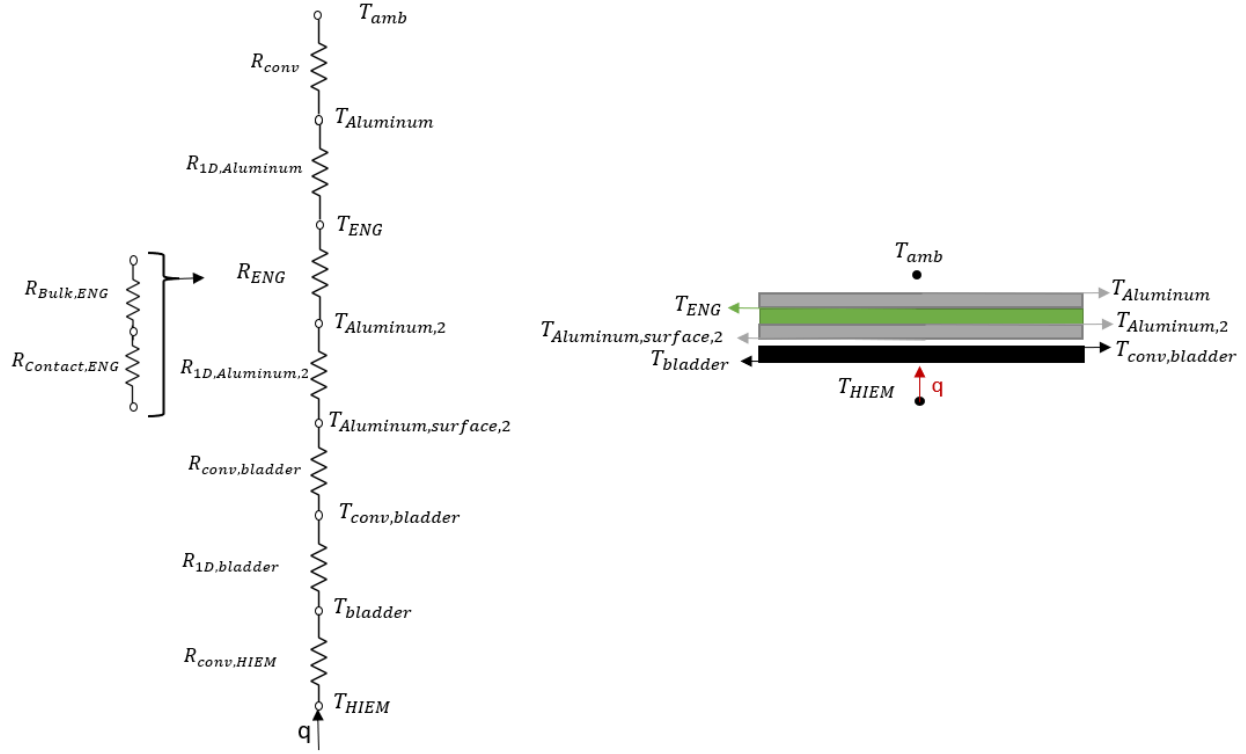


Figure 35- Thermal resistance network for Test B

Determine the heat flux performance of the thermal transfer panel. To calculate the temperature of the interior environment Equation 66 is needed to calculate the heat release rate [48].

$$\dot{Q} = \frac{T_{HIEM} - T_{amb}}{R_{conv} + R_{1D,Aluminum} + R_{ENG} + R_{1D,Aluminum,2} + R_{conv,bladder} + R_{1D,bladder} + R_{conv,HIEM}} \quad (66)$$

The resistance for the interfaces is form of two components. First component is the thermal contact resistance that is the ratio of apparent temperature drop to the nominal heat flux over the apparent contact area ($R_{constriction}$) seen in Equation 67 [48]:

$$R_{constriction} = \frac{F}{2Nk_m a_m} \quad (67)$$

where N number of contacts and k_m harmonic mean conductivity. The F is the constriction alleviation factor and is given by Equation 68 where a is the mean contact radius and b is the air gap of the interface also seen in Figure 36. The harmonic mean conductivity is given by Equation 69 where k_1 and k_2 is the conductivity of each of the materials.

$$F = 1 - \frac{a}{b} \quad (68)$$

$$k_m = \frac{2k_1 k_2}{k_1 + k_2} \quad (69)$$

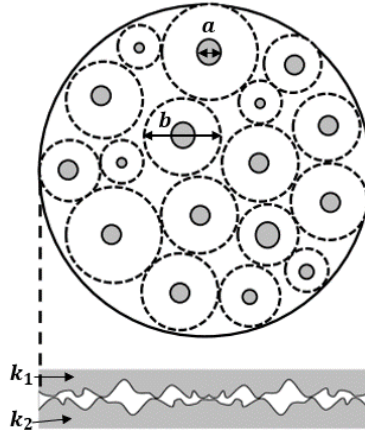


Figure 36-Microscopic view of the contact vs the air gaps of the interface between two materials

The other component is the gas gap resistance which is in terms of the gas gap conductance which the properties of the rough aluminum alloy is seen in Equation 70.

$$R_{gas,conductance} = \frac{1}{h_{gas}A} \quad (70)$$

The gas gap conductance is calculated through h_{gas} seen in Equation 71.

$$h = \frac{k_{gas}}{\delta + g_1 + g_2} \quad (71)$$

where δ is the mean gap distance (seen in Equation 72) and g is the temperature jump distance (represents imperfect energy transfer between gas molecules and wall seen in Equation 73).

$$\delta = 1.184\sigma \left(-\ln \frac{3.132P}{H} \right)^{0.547} \quad (72)$$

$$g = \left(\frac{2 - \alpha}{\alpha} \right) \left(\frac{2}{\gamma + 1} \right) \left(\frac{k_{gas}}{\mu c_v} \right) \theta \quad (73)$$

Using the properties from Table 12 the gas conductance is 4790 W/m²K meaning this is around 50% more than the solid spot conductance. This means that the interfaces in the thermal transfer panel are critical and need to be analyzed experimentally to find an optimum solution.

Table 11-Properties of air

Property	Air
k_{gas}	0.0262 W/mK
γ	1.4
μ	18.5x10 ⁻⁶ kg/ms
c_v	718 J/kgK
θ	0.064x10 ⁻⁶ m
α	0.9
μ	18.5x10 ⁻⁶ kg/ms

(74)

$$R_{Interface,1} = R_{constriction} + R_{gas,conductance}$$

The total interface thermal resistance is Equation 74.

The value of the interface thermal resistance could be greater than the conductance thermal resistance meaning that the interface needs to be improved.

4.2.3 Cyber-physical testbed model: Test setup C

Once the characterization of the resistance and capacitors are done through test A and B it is proceeded to testing the overall system with test C. For this system the heat balance as seen in Figure 37 includes all the layers and the thermal transfer panel as a thermal load that goes into the system and Figure 38 shows the thermal resistance network.

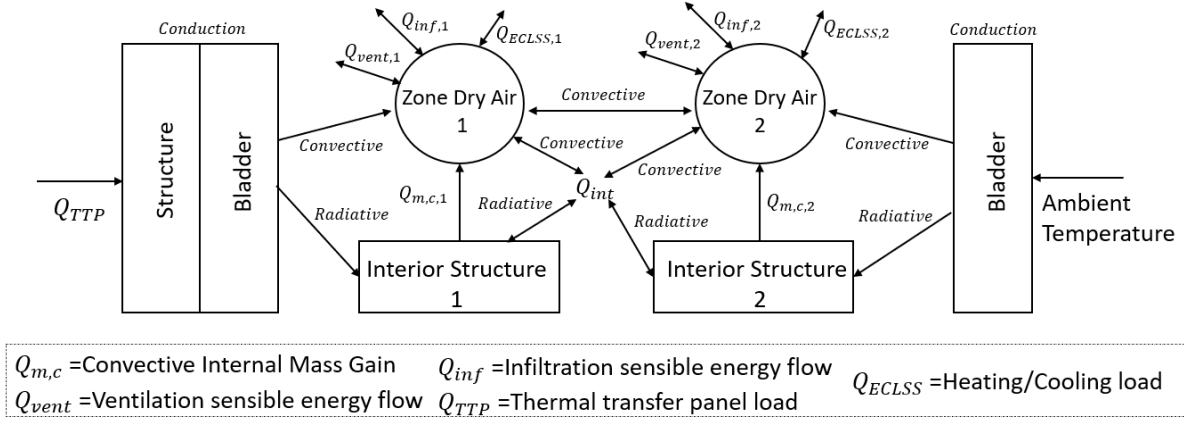


Figure 37-Diagram of heat transfer of Test C

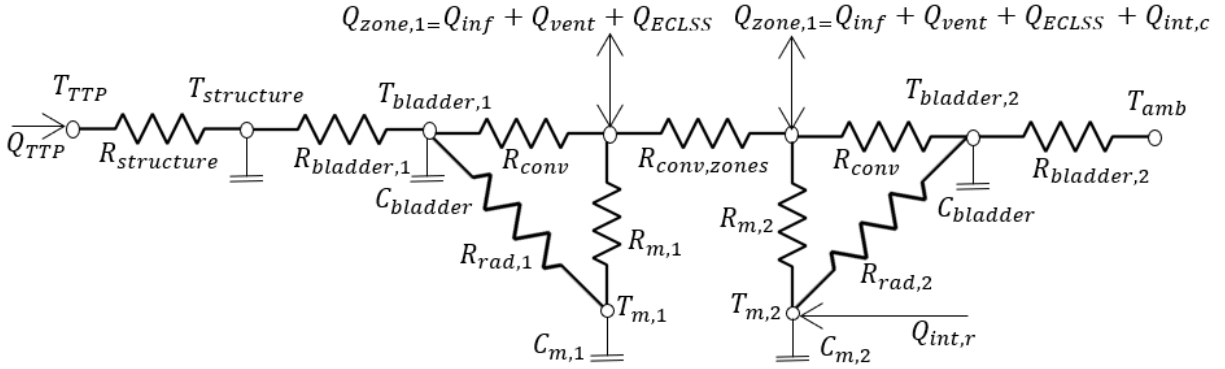


Figure 38-Thermal resistance network for Test C

Which leads to Equations 75-78.

$$\frac{dT_{m,i}}{dt} = \left(\frac{T_{z,i} - T_{m,i}}{R_{m,i}C_{m,i}} \right) + \left(\frac{T_{bladder,i} - T_{m,i}}{R_{rad,i}C_{m,i}} \right) + \frac{\sum F_{g,r}Q_g}{C_{m,i}} \quad (75)$$

$$\frac{dT_{structure}}{dt} = \left(\frac{T_{TTP} - T_{structure}}{R_{structure}C_{structure}} \right) + \left(\frac{T_{bladder,1} - T_{structure}}{R_{bladder,1}C_{structure}} \right) \quad (76)$$

$$\frac{dT_{bladder,1}}{dt} = \left(\frac{T_{structure} - T_{bladder,1}}{R_{bladder,1}C_{bladder,1}} \right) + \left(\frac{T_{z,1} - T_{bladder,1}}{R_{conv}C_{bladder,1}} \right) \quad (77)$$

$$\frac{dT_{bladder,2}}{dt} = \left(\frac{T_{amb} - T_{bladder,2}}{R_{bladder,2}C_{bladder,2}} \right) + \left(\frac{T_{z,1} - T_{bladder,2}}{R_{conv}C_{bladder,2}} \right) \quad (78)$$

The energy balance on the zone air equations (i being 1 or 2), the thermal transfer panel temperature yields an algebraic set of equation seen by Equation 79 and 80.

$$\frac{(T_{bladder,i} - T_{z,i})}{R_{conv}} + \frac{(T_{m,i} - T_{z,i})}{R_{m,i}} + \frac{(T_{air,1} - T_{air,2})}{R_{conv}} + \sum F_{g,c} Q_g + Q_{cooling} + \dot{m}_v c_p (T_{amb} - T_z) + \dot{m}_{inf} c_p (T_{amb} - T_z) = 0 \quad (79)$$

$$\frac{(T_{structure} - T_{TTP})}{R_{structure}} + \sum Q_{TTP} = 0 \quad (80)$$

To determine the temperature of the TTP, which is the temperature at the outside of the structural subsystem, the following differential equation needs to be solved using the thermal resistance network shown in Figure 39. The calculations are based on several assumptions, including a constant temperature for the Syltherm, a constant thermal conductivity coefficient, and uniform heat flux from the Syltherm. The system is assumed to be at steady-state conditions, with two-dimensional conduction resistances (negligible heat transfer from sides of components) and constant properties, and negligible radiation exchange with the surroundings. Additionally, heat transfer through aluminum L angles is neglected since since $A_{aluminum} > A_{alum,angles}$. The material properties are also specified below.

- Copper: Surface area (A_{Copper}) 0.115 m², a thickness (d_{copper}) of 0.00254 m, and thermal conductivity (k_{Copper}) of 401 W/m-K
- Syltherm: Surface area ($A_{syltherm}$) 0.0307 m², a thickness ($d_{syltherm}$) of 0.01905 m, and thermal conductivity ($k_{syltherm}$) of 0.1129 W/m-K
- TC-6020: Surface area (A_{TC}) 0.0307 m² a thickness (d_{ENG}) of 0.0095 m and thermal conductivity (k_{ENG}) of 2.72 W/m-K

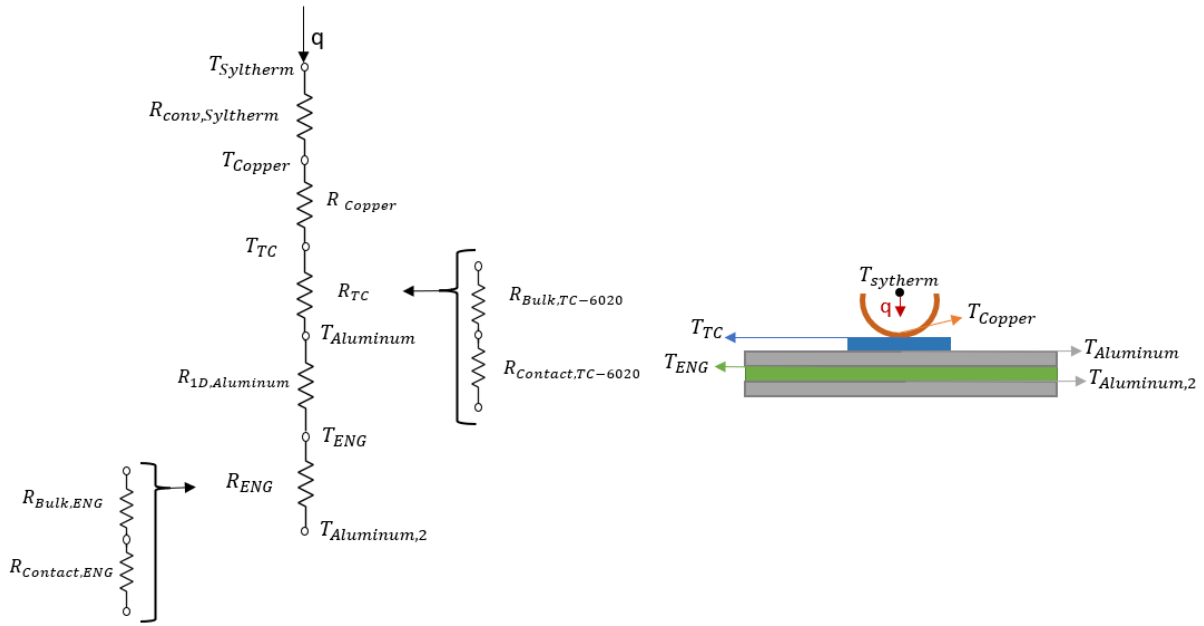


Figure 39-Test C thermal resistance network

Knowing the load from the Syltherm it can be determine the temperature at the aluminum structure know in Figure 39 has T_{aluminum,2}. To calculate that temperature, it is first needed to calculate the load of the Syltherm which is done by Equation 81.

$$\dot{Q}_{syltherm} = \dot{m}_{syltherm} c_p \Delta T_{syltherm} \quad (81)$$

Where $\dot{m}_{syltherm}$ is the flow rate of the syltherm going through the copper pipe, $\Delta T_{syltherm}$ is the temperature drop of the Syltherm and c_p is the coefficient of pressure of the syltherm.

Knowing the load it can be determine the heat flux performance of the thermal transfer panel. To calculate the temperature of the surface of the aluminum panel Equation 1 is needed .

$$\dot{Q} = \frac{T_{surface} - T_{syltherm}}{R_{Syltherm} + R_{Cu,cond} + R_{Interface,1} + R_{Alu,cond} + R_{Interface,2}} \quad (82)$$

For the thermal interface material, the resistance value is calculated into two parts. The contact thermal resistance which is the contact between the thermal interface material (TIM) and the contacting surfaces due to non-perfect wetting ($R_{Contact}$) seen in Equation 83. The contact resistance can be estimated neglecting the thermal resistance of the thermal interface material (TIM) compared to the thermal conductivity of the solid material ($k_{TIM} \ll k_{solid}$) [48]. Then there is the thermal resistance due to conduction across the bond line thickness (R_{Bulk}) seen in Equation 84.

$$R_{Contact} = \frac{\sigma}{2k_{TIM}} \frac{A_{real}}{A_{nominal}} \quad (83)$$

$$R_{Bulk} = \frac{d_{Bond\ Line\ Thickness}}{k_{TIM}} = \frac{1.31 \cdot 10^{-4} \left(\frac{\tau_y}{P}\right)^{0.166}}{k_{TIM}} \quad (84)$$

where σ is the rms roughness, the τ_y is the yield stress and P is the pressure. Then, $A_{nominal}$ is the nominal contact area and A_{real} is the whole geometrical surface area

To calculate the total effective area of the system is the addition of all the contact surfaces to the aluminum plate Equation 85 is used which are the aluminum L-angles, the thermal interface material and the copper.

$$A_{Total, effective} = A_{Al, angle} + A_{TC} + A_{copper} \quad (85)$$

4.3 Test setup A: Bladder control volume

To evaluate the normal conditions of the HIEM model a cooling or heating load will be integrated into the bladder through the mini-split system.

A mini split heat pump is a type of heating and cooling system that consists of two main components: an indoor unit and an outdoor unit. The indoor unit is positioned inside the structure being cooled or heated (in this case, inside the bladder), and the outdoor unit is located outside the bladder in the lab. The two units are connected by refrigerant lines. The mini split heat pump works by transferring heat from the interior of the structure to the outdoor unit using an evaporating refrigerant. The refrigerant is then compressed to a higher pressure and rejected back into the interior of the structure through the indoor heat exchanger, which cools or heats the air depending on the desired temperature. In this case, the mini split heat pump is integrated into the HIEM model to evaluate the normal conditions of the interior environment.

To validate the model of the heat pump, pressure sensors, mass flow meter and thermocouples must be installed for measurement. The inlets and outlets of the heat exchangers require temperature and pressure readings to determine the state of the working fluid, thus determining its enthalpy. The measurements will correspond to the four defined state points in the model as seen in Figure 40. A mass flow meter is necessary to measure the flow rate of the refrigerant in the outlet of the compressor. This mass flow rate data will then be used to calculate the heat transfer loads in the heat exchanger.

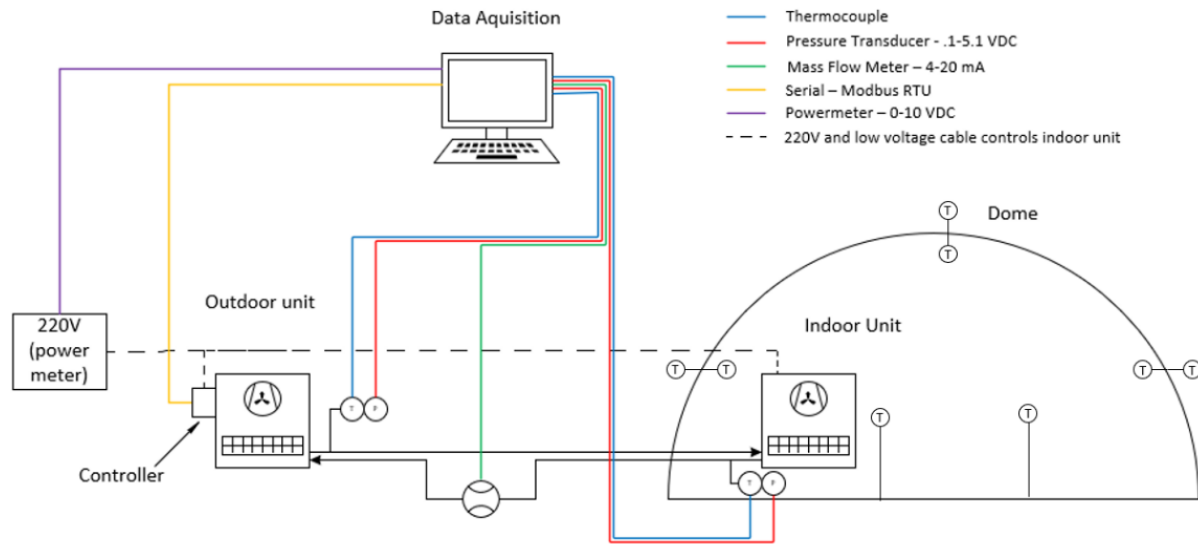


Figure 40-PI&D of test setup A (adapted from [53])

The placement of thermocouples inside the dome includes five thermocouples placed in the interior walls of the bladder, halfway up from the floor in each extreme, and one at the top of the bladder. Additionally, the same location outside the bladder will have a thermocouple. Lastly, two thermocouples will be placed inside the bladder for air temperatures. Then there is two air thermocouples for redundancy and to replicate the MCVT HIEM model.

Table 12- Sensor's specification for Test A

Number Sensors	Signal	Sensor Type	Model	Specifications	Tolerance
14	Inlet temperature	Thermocouple Type T	Omega K	-200°C to 350°C	±1.0°C
2	Control pressure	Voltage output	Setra Model 207 (High Pressure)	0 to 500 psig	±0.325 psig
2	Control pressure	Voltage output pressure transducer	Setra Model 207 (Low Pressure)	0 to 250 psig	±0.325 psig
1	Control flow	Turbine flow meter	Emerson Micro Motion Elite Coriolis	0 to 110 kg/hr	±0.110 kg/hr
1	Power control	Voltage output	Ohio Semitronics Model GW5	0 to 20 kW	±0.0008 kW

The location of the thermocouples around the bladder is shown in Figure 41, and two thermocouples are used to measure the air temperature of the interior habitat, with each one placed in one of the zones. The stands for these thermocouples are also shown in Figure 41 along with their placement location.

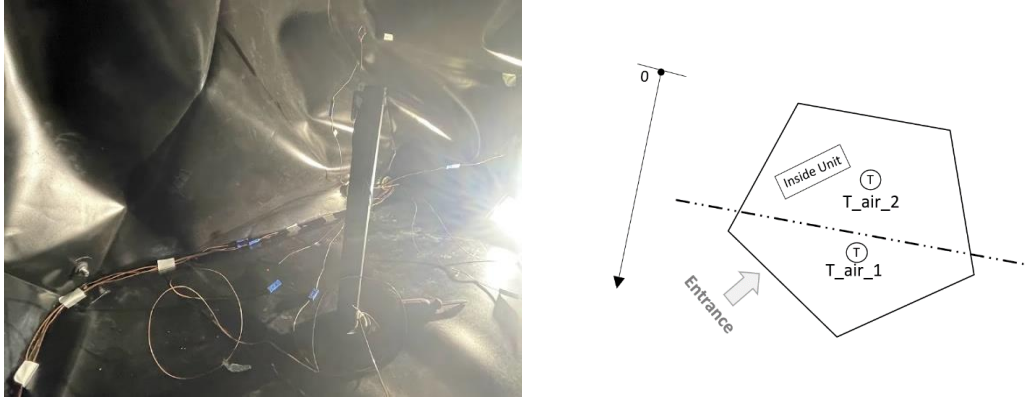


Figure 41-Physical sensor inside the bladder and diagram of the location of air temperature readings

There are five additional thermocouples placed inside the bladder, with one located in each corner and the fifth one at the center of the bladder's ceiling. These thermocouples are connected to the data acquisition system through a feedthrough mechanism, as shown in Figure 42. This mechanism allows for the cables to pass through the dome structure without compromising its pressurization.

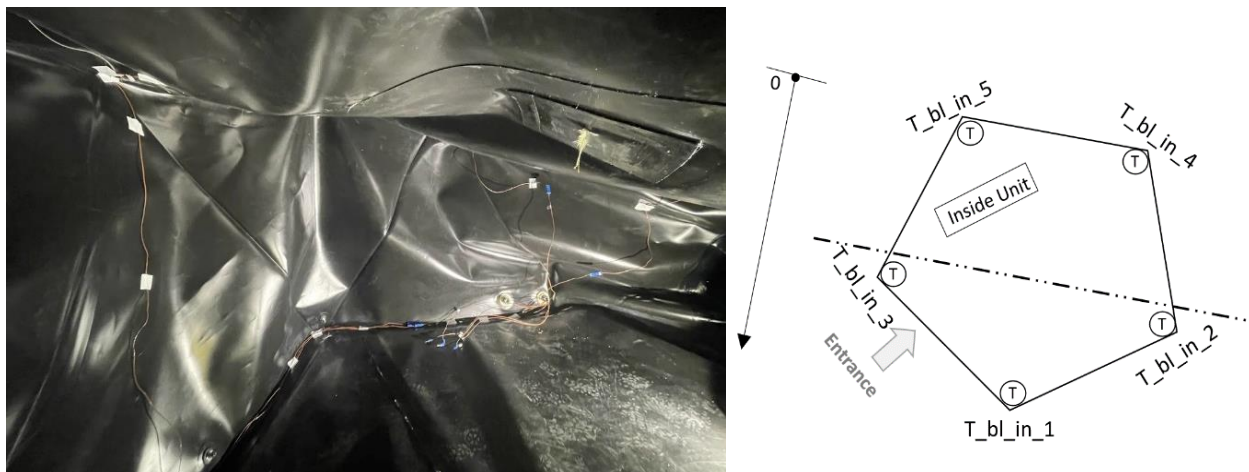


Figure 42-Physical sensor inside the bladder and diagram of the location of bladder in temperature readings

The last remaining five thermocouples are placed in the outside part of the bladder and covered with TIM, so it reads the bladder temperature and not the air between the bladder and the structure as seen in Figure 43.

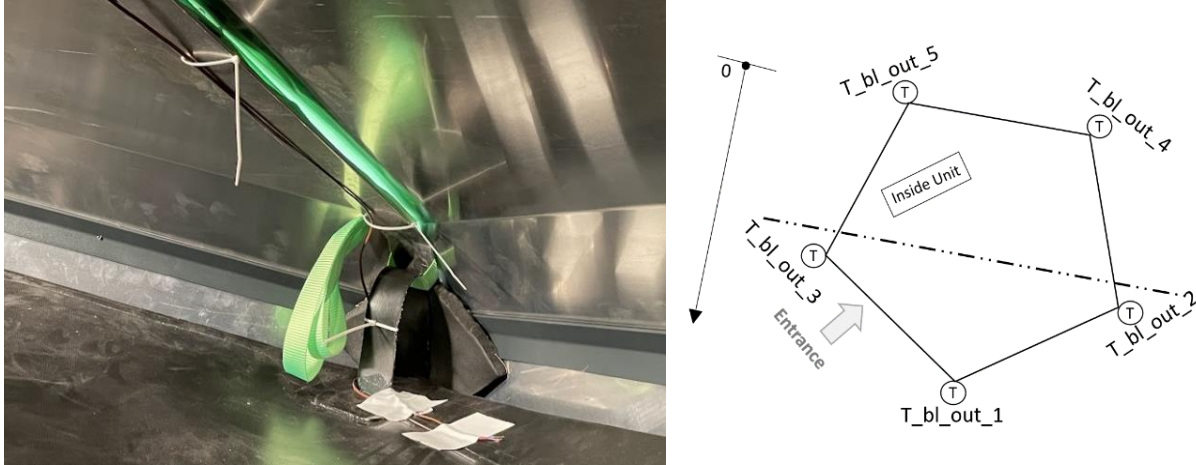


Figure 43- Physical sensor outside the bladder and diagram of the location of bladder out temperature readings

The DAQ converts the voltage produced by the thermocouple into a temperature value, which can then be processed and analyzed in real-time. The SpeedGoat system is also equipped with a watchdog timer to prevent the system from crashing in the event of a software or hardware failure. It also works seamlessly with Simulink Real-Time. The data from the sensors and thermocouples is then logged and analyzed to validate the thermal model and evaluate the performance of the mini split heat pump. The m+p international DAQ is required to read the thermocouple data. It is a specialized device that converts the temperature readings from the thermocouple sensors into a digital signal that can be processed and analyzed. The pressure and power sensors are connected through the I/O modulus of SpeedGoat that directly goes to the Simulink.

To read the data a Simulink code was created to start and change the fan speed of the heat pump as well as to recollect the readings from all the sensors seen in Figure 44.

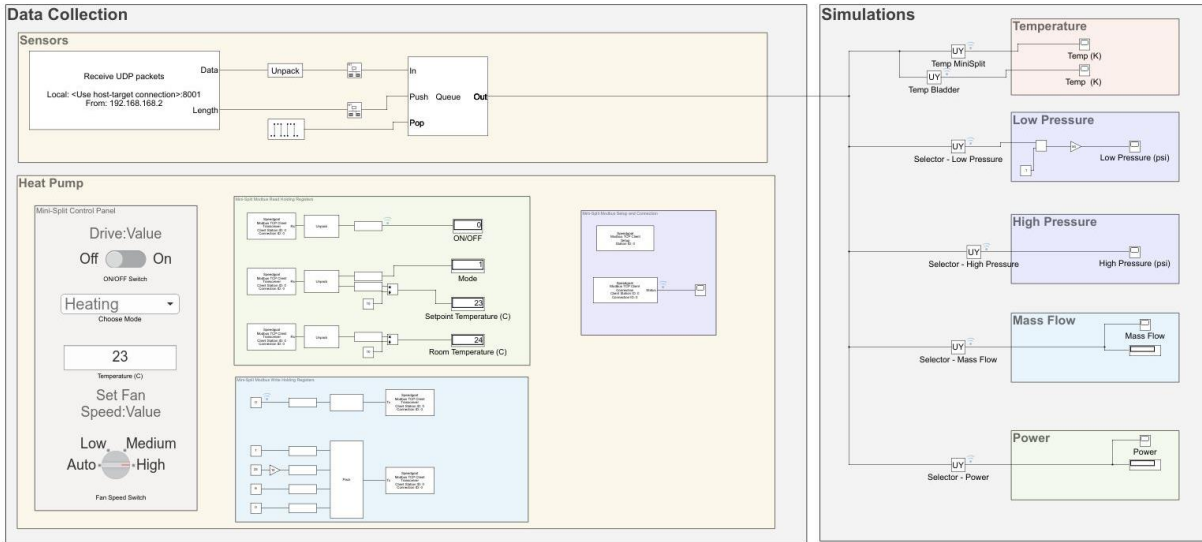


Figure 44-Simulink code of CPT sensor reading (adapted from [53])

Before starting the data acquisition when the testbed is in place some previous procedures need to be address. The calibration phase should take in place which consist in finding the right scaling factors to convert the output of each sensor (voltage) in physical signals (pressure, temperature, and flow) for it can be found in Appendix A.

Figure 45 shows the testing procedure which starts of by starting up the heat pump and pressurizing the bladder. By pressurizing it means trying to have as much contact from the bladder to the structure. Then the initial conditions are set in the Simulink model seen in Figure 44. Lastly the data is recollected and making sure that when a steady state of the temperature is reach there aren't temperature fluctuations higher than 2%. Appendix B has the detailed procedure.

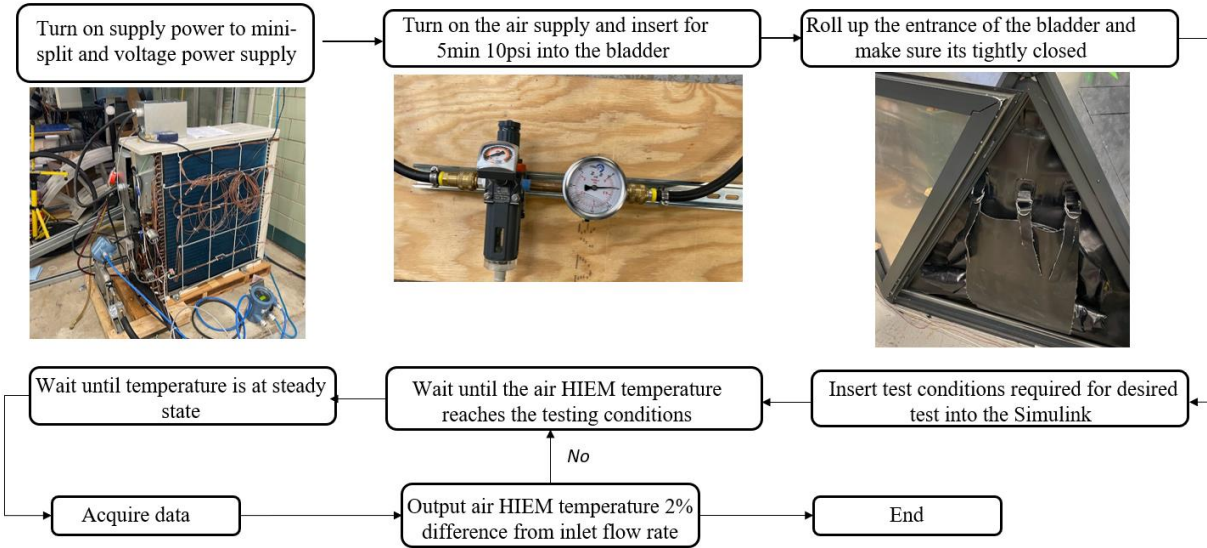


Figure 45-Testing procedure for Test A

4.4 Test setup B: Aluminum of the TTP control volume

The present study utilizes a test setup to assess the heat transfer of interface materials. The setup involves the placement of three thermal couples within each layer, as depicted in Figure 46. This redundant arrangement ensures consistent temperature readings at the same location within each layer.

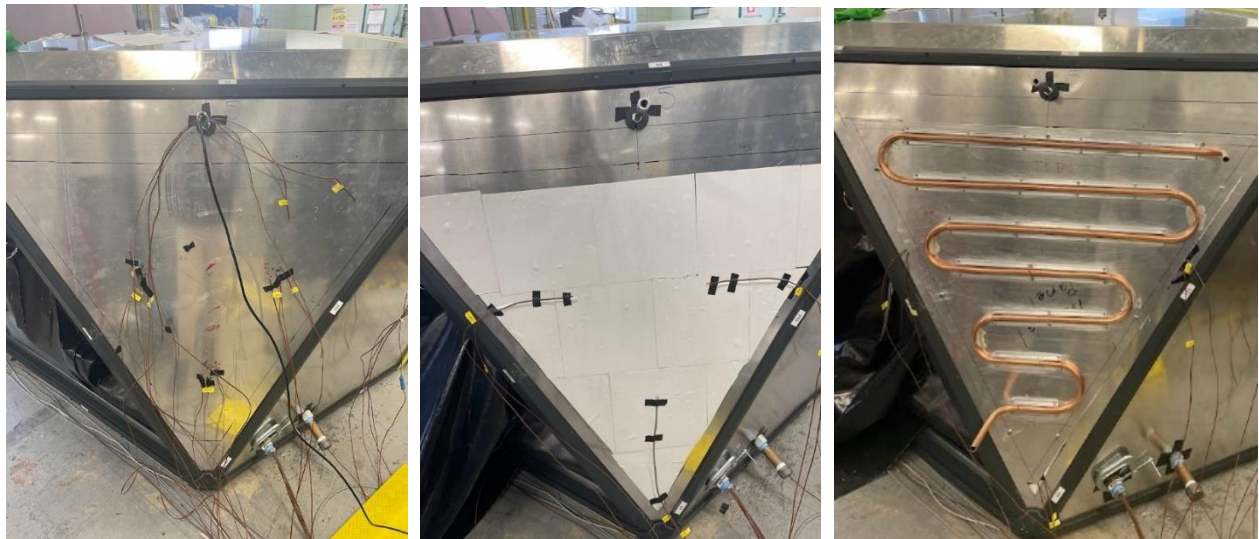


Figure 45- The different layers beyond the bladder of the CPT. The structural subsystem (left), the thermal interface material (middle) and the thermal transfer panel (right)

To evaluate different heating loads, an electric heater and lamps were placed inside the habitat as well. The heater Slant/Fin has a max heating capacity of 1.5kW. Also black box stand is used which has four lamps and each of the lamps has 250 W seen in Figure 47. The objective of this study is to evaluate the performance of a mini-split system under specific heating loads in a habitat, which in turn produces a periodic cooling load. The study also aims to validate whether the interior environment takes into account the loads of the mini-split system and whether it can predict internal loads. The representation of the internal loads includes lamps, which represent four humans performing activities inside the habitat, and a radiator, which represents the internal load addition of all computers, chairs, and materials that could be present in a habitat. By conducting this study, it is expected to gain a better understanding of the mini-split system's performance in the interior environment.



Figure 46-The box which contains four lamps (left) and the heater to the right of the unit of the mini-split (right)

4.5 Thermal transfer panel design

In a cyber-physical testing environment, a transfer system is utilized to establish a connection between the cyber and physical components by applying physical input. Specifically, the thermal transfer panel (TTP) consists of a controllable chiller and thermal coil connected to pipes that transfer Syltherm fluid to the testbed to achieve the desired temperature at the interface. However, the design of the TTP must undergo testing and validation prior to implementation.

The Cyber-Physical Testing (CPT) involve the characterization of the TTP using a pressure box and the simulation of disturbance scenarios to test the performance of the dome. The pressure box is a device that tests the panel's performance by subjecting it to controlled changes in temperature and pressure to simulate real-world conditions. The purpose of this testing is to ensure that the TTP will function properly under various conditions.

Once the TTP has been functionally tested, the optimization phase begins, which leads to the development of the dome. The dome comprises 9 thermal transfer panels that produce specific conditions in the interior environment to simulate disturbances. Redesigning the TTP from the pressure box to the dome requires rethinking various factors, including differences in surface area, panel shape, pressure drops, and ease of manufacturing given the increased number of panels in the dome. Figure 48 shows a preliminary design of the TTP of the dome compared to the pressure box.

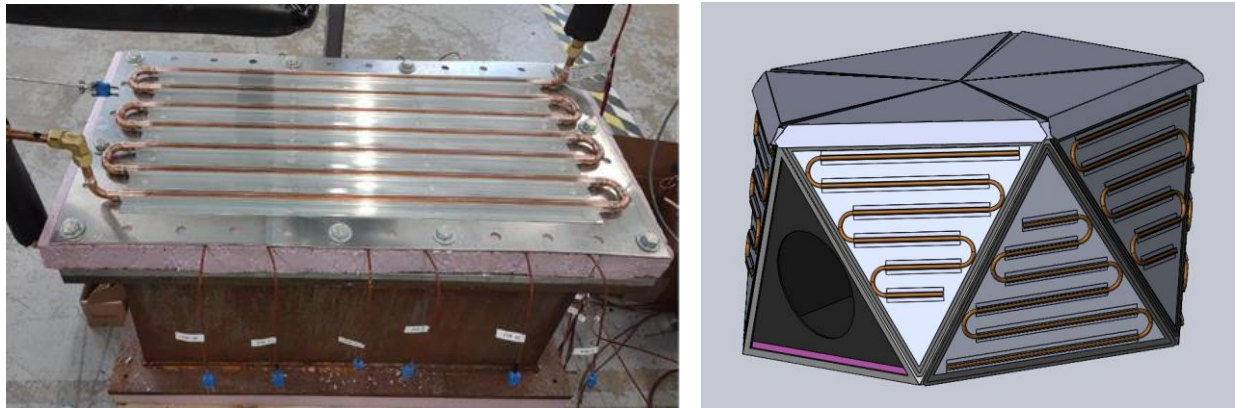


Figure 47- The pressure box testbed (left) and the CAD model of the dome testbed(right)

The lab configuration is depicted in Figure 49, where the chiller is located in room HLAB 90 and supplies Syltherm to the transfer panels. The piping system runs through the main pipe system in room 80 and splits into two. The fluid can either go to the pressure box for the first phase of the CPT or to the dome for the second phase of the CPT. However, only one of these systems can be operated at a time.

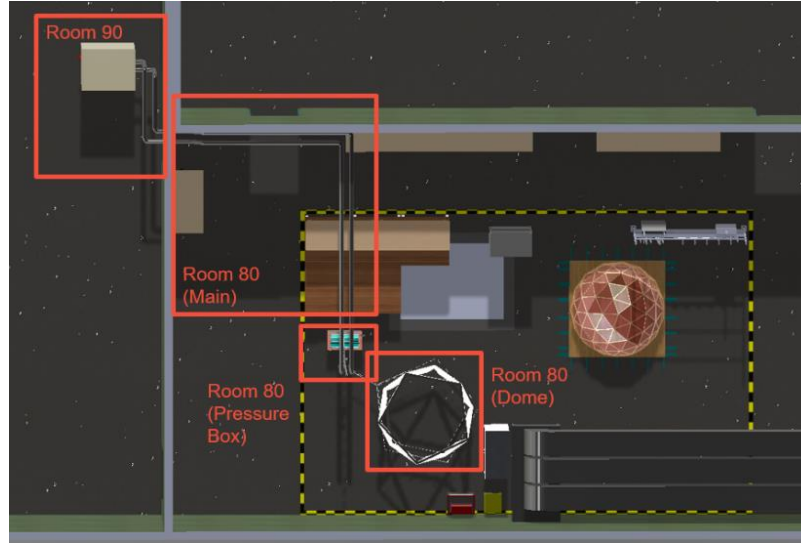


Figure 48- CAD model of the configuration of the lab

To design the thermal transfer panel, it is essential to first understand the pressure drops of the system. This involves calculating the pressure drop in the piping system to determine the available pressure before reaching the thermal transfer panel. The pressure drop calculation should consider potential losses, such as partially open valves, which can cause significant head losses and affect the proper functioning of all nine panels.

The pressure drop in a piping system is typically determined by two parameters: head loss (h_L) and frictional pressure drop (P_f). Head loss refers to the energy lost due to friction between the fluid and the pipe walls, while the frictional pressure drop is the difference in pressure between the inlet and outlet of the pipe resulting from the friction between the fluid and the pipe walls. The calculation of h_L and P_f requires various parameters, including the flow rate (Q), pipe diameter (D), pipe length (L), pipe roughness (ϵ), fluid density (ρ), and fluid viscosity (μ). The equations used to calculate h_L and P_f are based on the Darcy-Weisbach equation, which states that the head loss (h_L) is proportional to the square of the fluid velocity, pipe length, and fluid properties, and the Moody diagram, which provides a graphical representation of the relationship between the frictional factor and the Reynolds number, a dimensionless number that represents the flow regime.

For the calculation of h_L and P_f in this system, it is assumed that the pipe roughness is that of copper, which is approximately 0.00000328 (ϵ). The fluid properties, including the density (ρ) and viscosity (μ) of Syltherm, are provided by the manufacturer [49].

The first step is to determine the friction factor (f) (Equation 86) assuming a completely turbulent flow through the Moody friction factor equations.

$$f = \left(1.14 + 2 \log_{10} \left(\frac{D}{\varepsilon} \right) \right)^{-2} \quad (86)$$

To confirm that the flow is indeed completely turbulent, the friction factor will be calculated using the transition region Equation 87 and compared to the previous calculation to determine any differences.

$$f = \left(-2 \log_{10} \left(\frac{\varepsilon/D}{3.7} + \frac{2.51}{Re(f^{0.5})} \right) \right)^{-2} \quad (87)$$

Then the heat loss is calculated with Equation 88 and then the frictional pressure drops with Equation 89.

$$h_{Lf} = f \left(\frac{L}{D} \right) \left(\frac{V^2}{2g} \right) \quad (88)$$

$$\Delta p_f = \rho g h_{Lf} \quad (89)$$

Fluid head loss through a fitting can be calculated by the following Equation 90 where h_{Lc} is the pressure loss in terms of fluid head do to the connections, K is the manufactures factor for the fitting, V the velocity of fluid and g the acceleration due to gravity.

$$h_{Lc} = K * \frac{V^2}{2g} \quad (90)$$

The connection pressure drop is calculated with the same formula of the frictional pressure drop just with a different head loss. Then the total pressure drop is the addition of these two seen in Equation 91.

$$\Delta p_{total} = \Delta p_f + \Delta p_c \quad (91)$$

To verify the flow regime, the friction factor is calculated for the transition region equation. This ensures that the flow is completely turbulent and accounts for any changes in the calculation. In the analysis, it's typically assumed that the effect of fitting losses is minor and can be ignored for initial analysis of the piping system. However, if the piping design includes partially open

valves, it's crucial to include the head loss and effect of the valve in the analysis, as it can significantly impact the overall head loss in the system.

To verify the calculation approach for the pressure drops the data it is first calculated theoretically the pressure drops of the pressure box and compare it to the experimental data [50]. Assuming that the temperature of the Syltherm is at 25 °C.

Vertical pipes have a bigger pressure drop compared to horizontal pipes due to gravity. In a vertical pipe, fluid must overcome the gravitational force to flow from top to bottom, which requires additional pressure to maintain the flow. The additional pressure drop is known as the "pressure head" and is proportional to the height of the fluid column. On the other hand, in a horizontal pipe, fluid does not have to overcome the gravitational force and can flow freely, resulting in lower pressure drop. This is seen in the pressure drops in room 90 (Figure 50). Pipes 2 and 6 are the largest due to their vertical orientation. Pipes 3 and 7, which are of similar length but horizontal, result in a smaller pressure drop, but are still in second place. Additionally, as the mass flow decreases, the pressure drop in all pipes decreases as well.

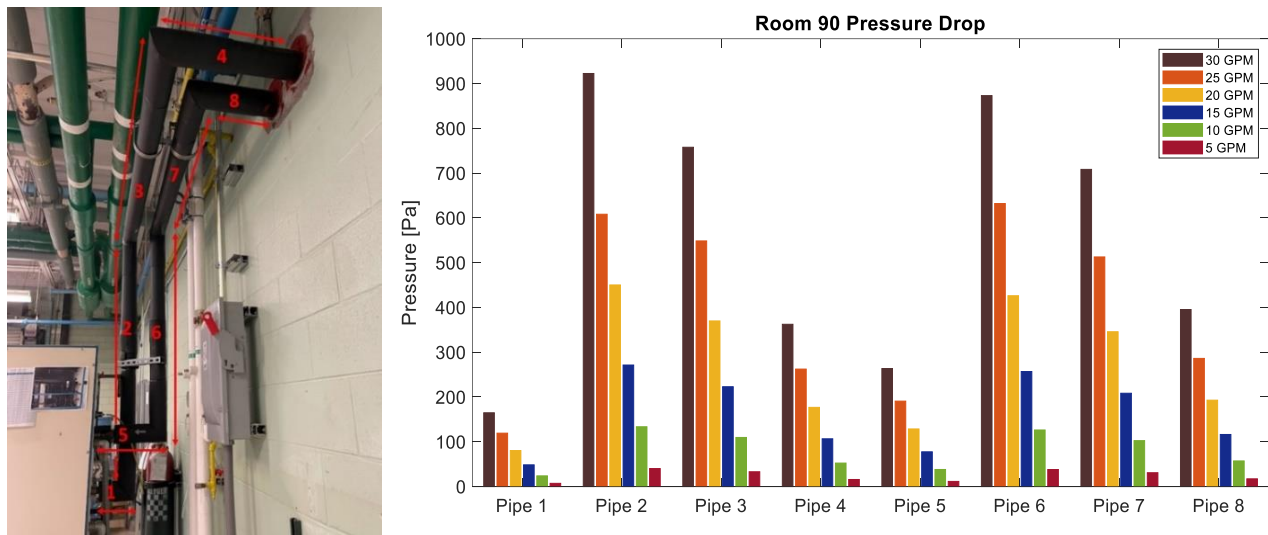


Figure 49-The piping system of room 90 (left) and the pressure drops (left)

Figure 49 corresponds to the pressure drop at different GPM of room 80 main pipe system. Pipes 5 and 6 have a bigger pressure drop than the vertical pipes because there 100 inches and 112 inches bigger than the other pipes. Figure 51 shows the pressure loss of the piping specifically to the pressure box.

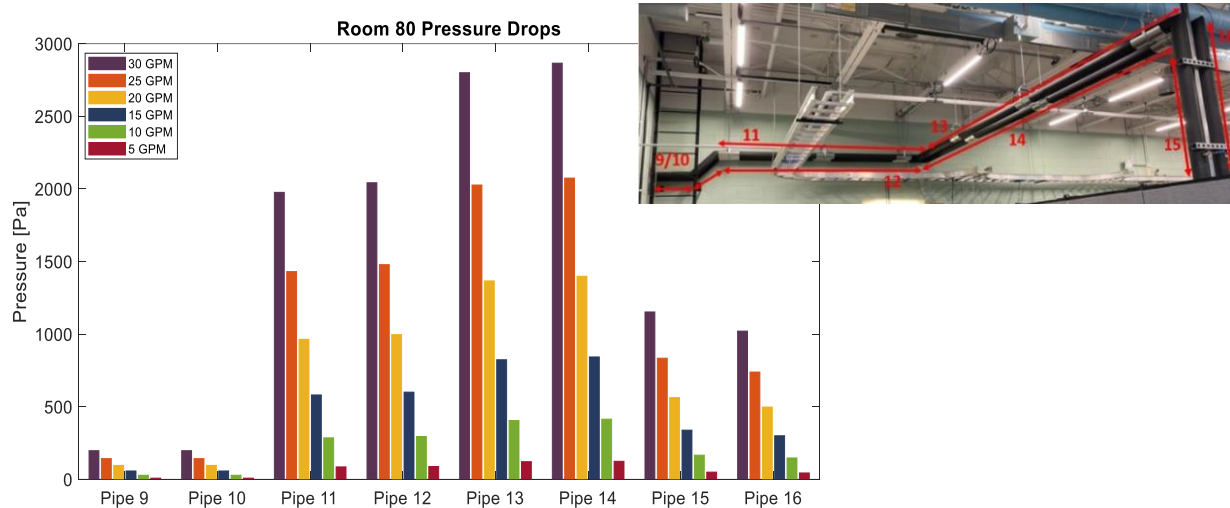


Figure 50- The main piping system of room 80 (left) and the pressure drops (left)

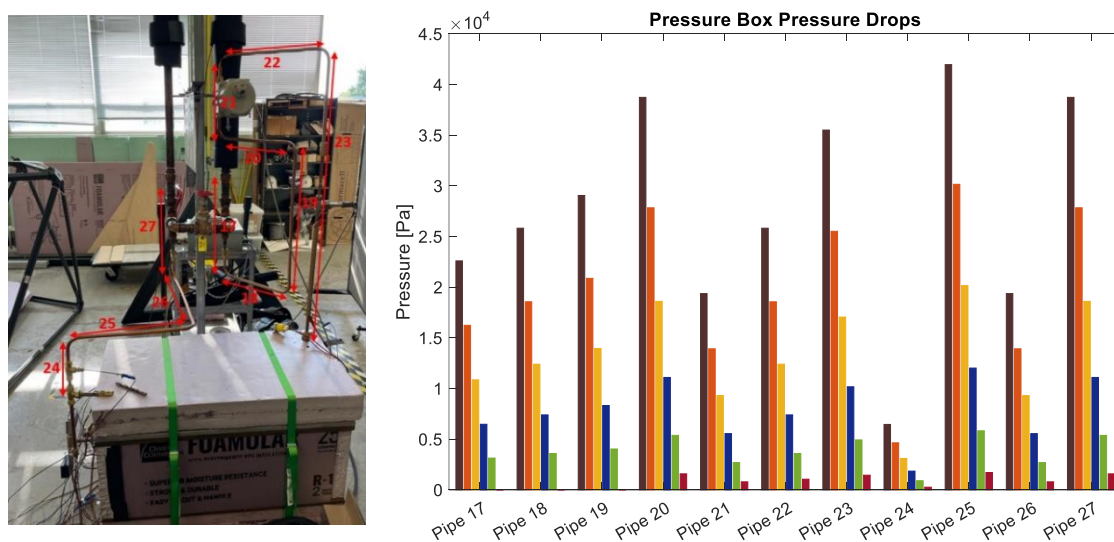


Figure 51- The pressure box piping system of room 80 (left) and the pressure drops (left)

The connections of the pressure box are considered negligible in the calculation of pressure drop as Figure 53 shows the values are insignificant even at 30 GPM.

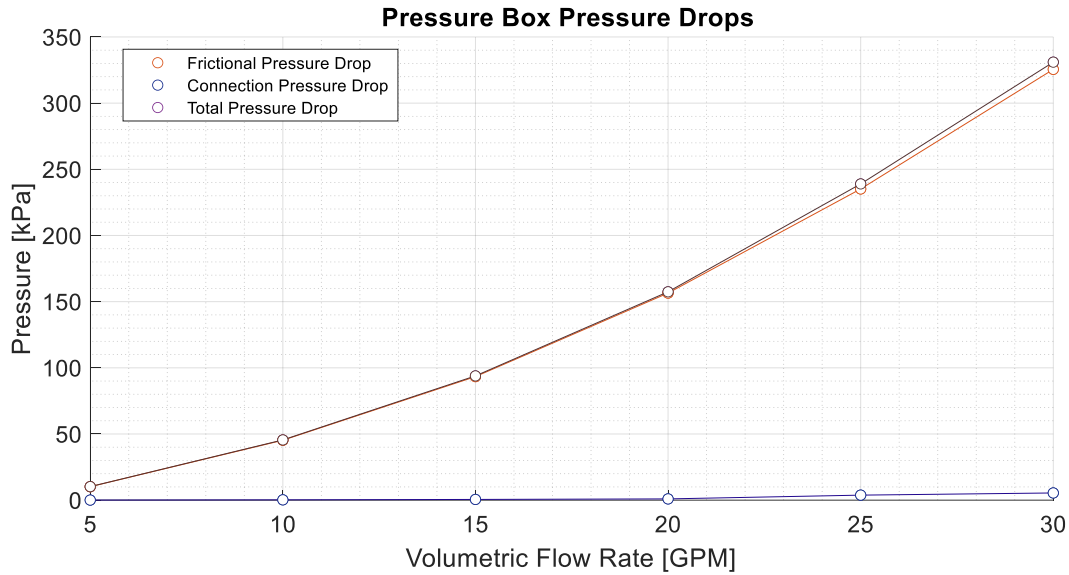


Figure 52- Pressure drops calculated analytically of the pressure box

After validating the theoretical method for pressure drop calculation, it can be applied to the design of the thermal transfer panel. The pressure drops calculations from room HERL90 to room HERL80 main pipe system will be used to guide the dome design. Specifically, the pipe system for the dome needs to be designed as well. The preliminary design for the dome, shown in Figure 54, is assumed for these calculations.

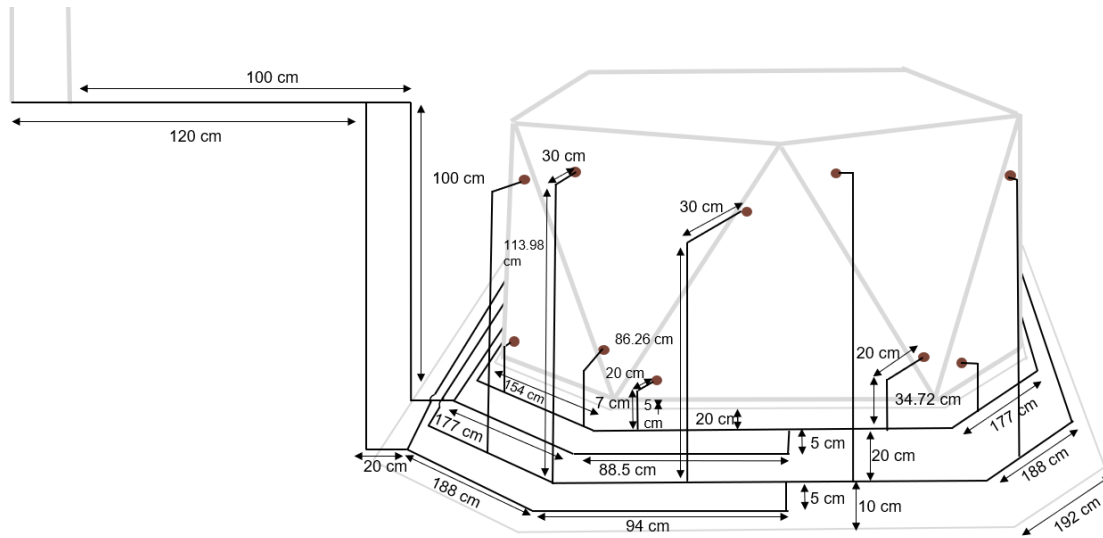


Figure 53-Preliminary design of the 9 thermal transfer panel piping

In order to properly conduct the experiments, it is important to consider the placement of sensors and valves in the design of the dome pipe system. This will ensure accurate readings and control of the various components and elements within the system. Figure 55 shows the preliminary design of the connection of the sensors and valves.

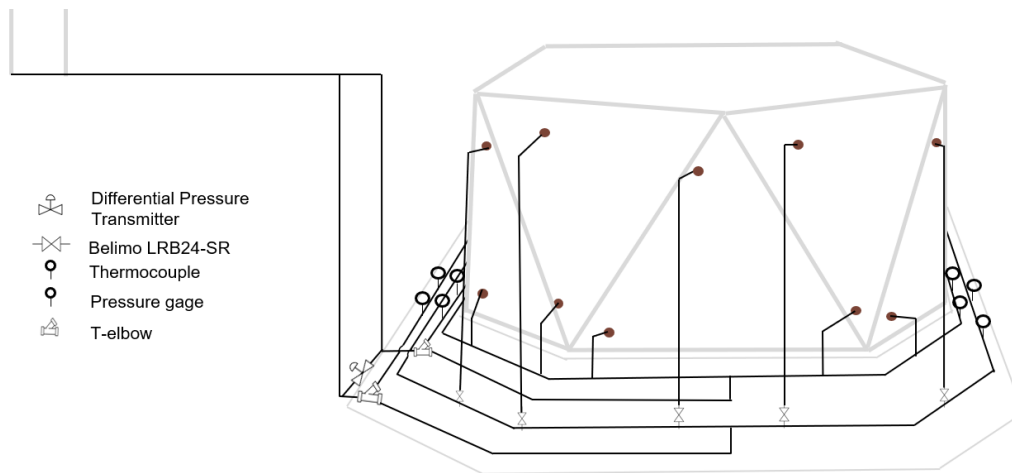


Figure 54- Preliminary design of the 9 thermal transfer panel sensors

Figure 56 shows the results of the dome plus room pressure drop as well as the flow rate supplied based on pump curve of the chiller.

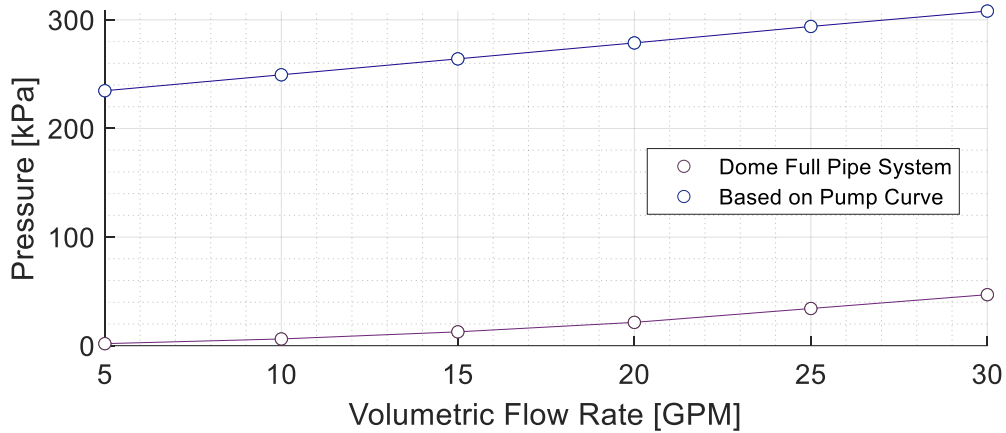


Figure 55- Pressure drops of the overall system vs the heat pump curve

Based on Figure 56, the pressure drop is shown as the difference between the maximum available pressure and the pressure required for the maximum capacity of the chiller. This information is used to design the 9 thermal panels that will be connected in parallel to the chiller that are explained in Section 4.5.1. The maximum capacity of the chiller is 30 gallons per minute (GPM), which means that each panel can receive a maximum flow rate of 3.33 GPM. A preliminary study was conducted using a pipe size of 0.5 inches in diameter, similar to the pressure box design. A coil made of soft copper was also designed, with a minimum radius of 1.5 inches, as shown in Figure 57.

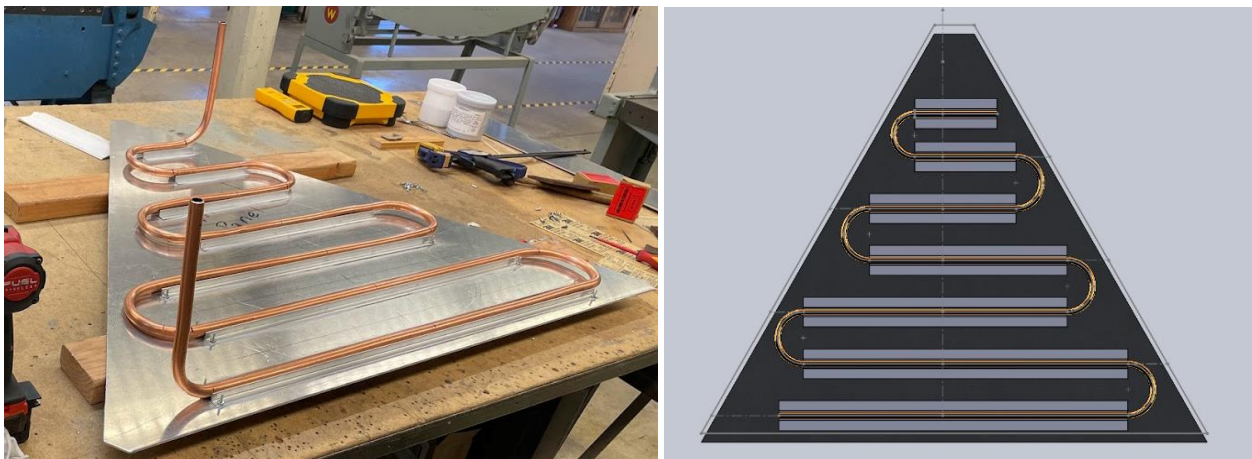


Figure 56- Physical thermal transfer panel (left) and the CAD model (right)

After having the theoretical confirmation that the system can function properly then a finalize CAD model (see Figure 58).

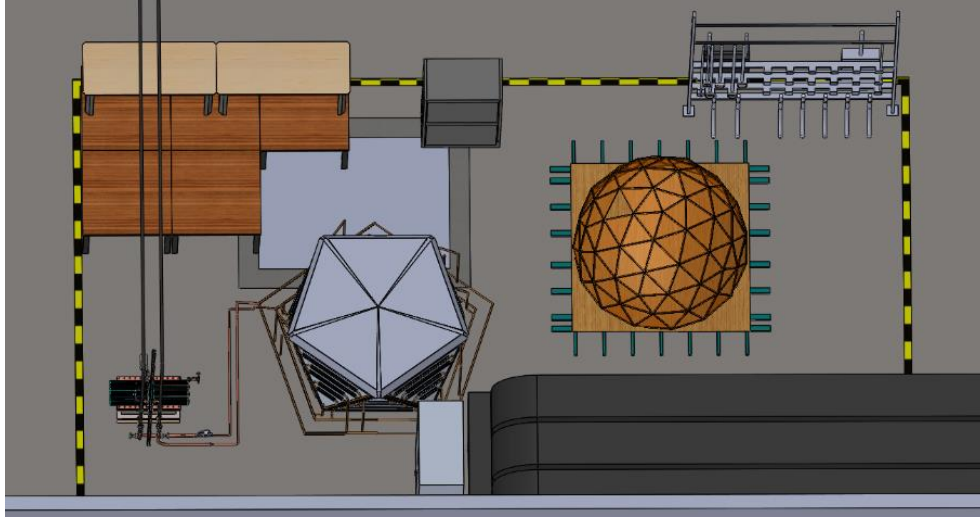


Figure 57- Final CAD of the room configuration with full piping system

4.5.1 Components of thermal transfer panel

The thermal transfer panels consist of several components, including aluminum angle L, copper pipe, aluminum plates, and thermal transfer interface materials. These components are used to construct the panel, as shown in Figure 59.

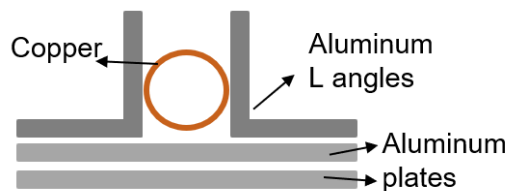


Figure 58- Components of thermal transfer panel

The aluminum angle L serves to bind the material and prevent deformation, which enhances the rigidity of the copper pipes. Additionally, it provides increased contact points for conduction. The aluminum plates were selected because of their previous successful use in the pressure box and their high thermal conductivity, as well as being lighter than copper. Two

aluminum plates were used, one for the structure of the dome subsystem and the other for the regolith subsystem. Copper pipes were chosen due to their common use in the industry for heat transfer systems, given their high thermal conductivity [48]. The 1/2-inch diameter was selected based on pressure drop calculations through the Darcy equation and accounting for connection losses in the entire dome system, as previously mentioned.

The chosen thermal transfer material for Phase A (as seen in the figure) is TC-6020 thermally conductive encapsulant. This material was selected for its ability to dissipate heat away from a component to a suitable heat sink, in this case, the aluminum plate. Additionally, it provides protection from harsh environments, vibration, and thermal [33]. Addition cure silicones are used to provide a deep section cure, enabling complete encapsulation for environmental protection while maintaining an effective heat path.

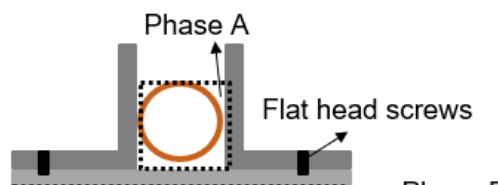


Figure 59- Diagram of TIM location

Based on Figure 61, which displays a range of thermal conductivity material solutions with varying viscosities and cure chemistries in different delivery formats, a high conductivity material with low viscosity is required for this application. Low viscosity is preferred to ensure that the material can easily fill all the areas around the pipe and reduce the creation of air gaps. Therefore, option 12 would be the best choice for this application.

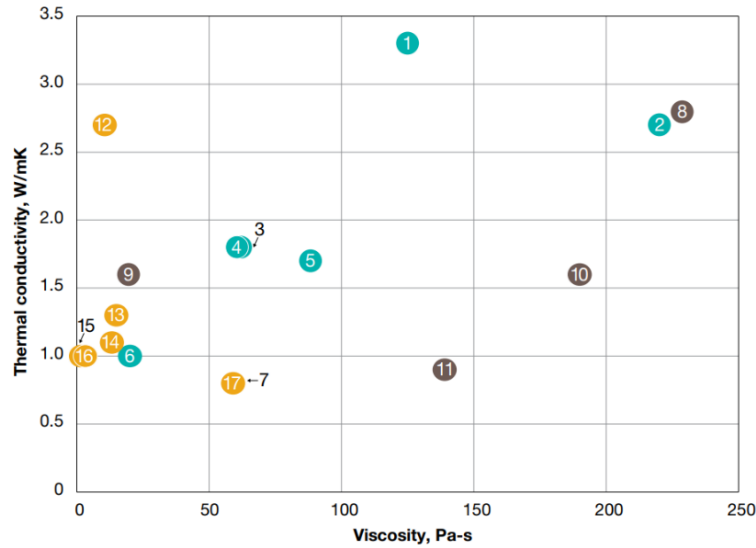


Figure 60-Thermal interface material from Dow thermal conductivity vs Viscosity [49]

4.5.2 Thermal transfer panel experimental setup

In the second phase of the dome thermal transfer panel testing, two subphases will be conducted. The first subphase involves testing a single panel to characterize its thermal load, followed by attaching the remaining eight panels. The corresponding piping and instrumentation diagram (PI&D) and list of sensors for the single thermal transfer panel can be found in Figure 62.

To ensure accurate data acquisition, it is critical to verify that the sensors are reading correctly. One method to achieve this is through redundancy by placing another sensor next to it to cross-check the value. As shown in the figure, the pressure gauge sensors are double-checked using the pressure sight sensors and the pressure differential transmitter. It is also important to characterize the pipelines of the system, taking into account pressure drops that may occur due to connections in the pipes during the experiment when acquiring data.

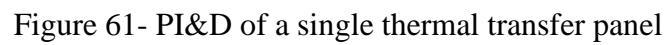
The ball valves are positioned for the purpose of assembly and disassembly, as well as to shut off lines that are not required to run simultaneously. Additionally, there is a bypass system in place to enable the flow to return to the beginning of the assembly. Next in line is a flow meter that serves to monitor the variance in flow between the chiller and the testbed due to the considerable distance between the two. Adjacent to it, there is an in-pipe thermocouple and a pressure gauge sensor. These two sensors are utilized to track the changes in flow and transform

the volumetric flow rate obtained from the flow meter to mass flow rate, accounting for any density changes.

An empty T is available for use in a separate experiment, such as pre-laminar panel testing, for sensor calibration or testing new components before integrating them into the system. Another T is present, containing two ball valves, with one system directing flow into the pressure box (indicated by blue lines) and the other directing flow into the triangular panel (indicated by green lines). Both systems are followed by couplings. Moving on to the triangular panel, there is a wire thermocouple that will be placed on top of the copper pipe and insulated. This sensor serves to characterize the temperature drops from the ball valve and T junctions between this position and the previous thermocouple. As such, an exact reading from this sensor is not necessary. Finally, there is a proportional solenoid valve, which will be utilized to characterize its performance as it will be used to shut off some of the panels when all are in operation.

Table 13- Sensor list for thermal transfer panel piping

Number Sensor	Signal	Sensor Type	Model	Specifications	Tolerance Value
4	Inlet temperature	Thermocouple Type T	Omega K	-200°C to 350°C	±1.0°C
3	Control pressure	Voltage output pressure transducer	Setra AXD	1psi to 50 psi	±0.25% FS
2	Control flow	Turbine flow meter	Hoffer	0.5 GPM to 60 GPM	± 0.20 % FS
2	Inlet temperature	RTD probe	Omega K	-50°C to 500°C	± 0.00385 °C



5. VALIDATION OF ANALYTICAL VERSUS EXPERIMENTAL RESULTS

The validation of the results will be corresponding to the HIEM CPT model that it uses the same principals seen in the HIEM MCVT model. The data recollected from the heat pump system will be at each of the states of the refrigerant which corresponds to Figure 63.

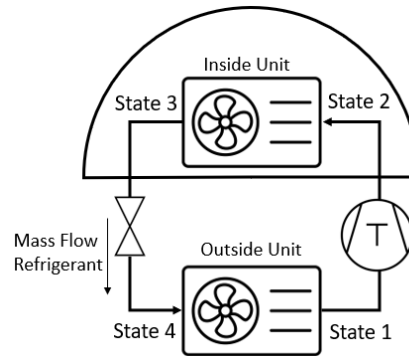


Figure 62-Experimental data of the mini-split pressures (a) and mass flow (b), inside unit temperatures (c) and outside unit temperatures (d) at maximum heating mode

5.1 Maximum heating scenario: Test A

The experiment was conducted for a duration of 2 hours at a constant temperature set point of 25 °C for the mini split system. The initial raw data obtained from the pressure sensors was converted from voltage readings to Pascals, whereas the data obtained from the flow meter was converted from volume flow rate to mass flow rate in grams per second (Figure 63). According to the data, the heating process exhibits three consistent stages. However, because the outside unit is in heating mode, it functions as an evaporator, while the inside unit functions as a condenser. This results in matching temperatures between the units, as well as matching flow mass and pressure. Therefore, the pressure and mass flow are activated and deactivated simultaneously. The pressure however between around 800 second and around 1,200 seconds has a considerable amount of noise.

The temperature fluctuations throughout the two-hour experiment are depicted in Figure 64, indicating simultaneous changes in temperature. However, the second air thermocouple located inside the bladder exhibited some noise at approximately 4,000 seconds and 200 seconds.

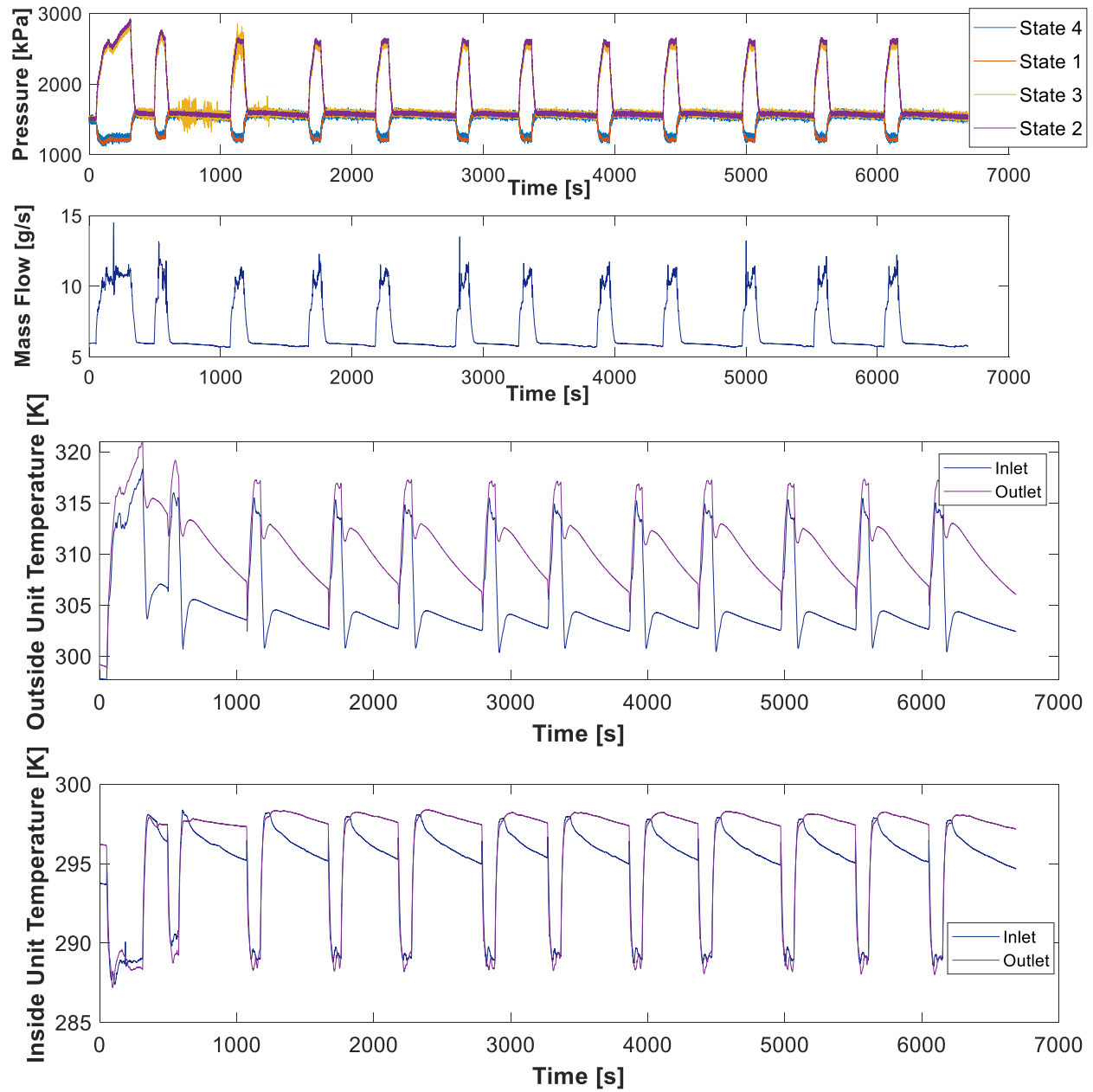


Figure 63- Experimental data of the mini-split pressures (a) and mass flow (b), inside unit temperatures (c) and outside unit temperatures (d) at maximum heating mode

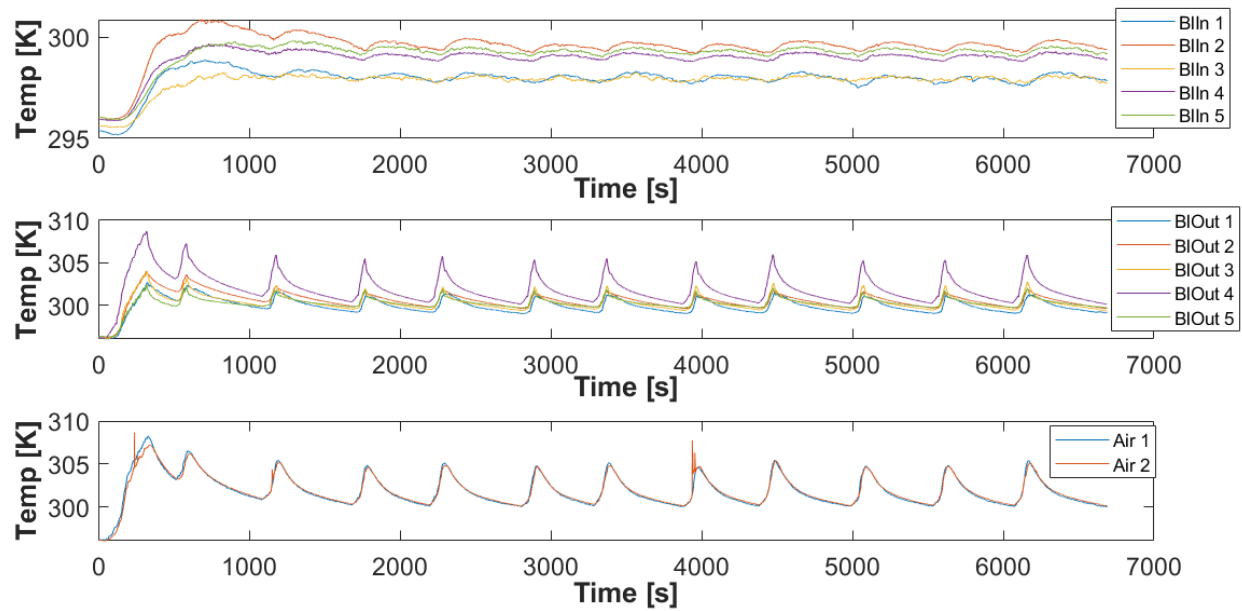


Figure 64- Heating at 25 C data of thermocouples of the bladder in temperature (a), bladder out temperature (b) and bladder air temperature (c)

5.1.1 Filtered data

To obtain the results shown in the figures below, the data had to be filtered for pressure signals, reduced to the periodic state (that will be used to validate the model), and down sampled to one-second intervals has illustrated in Figure 66.

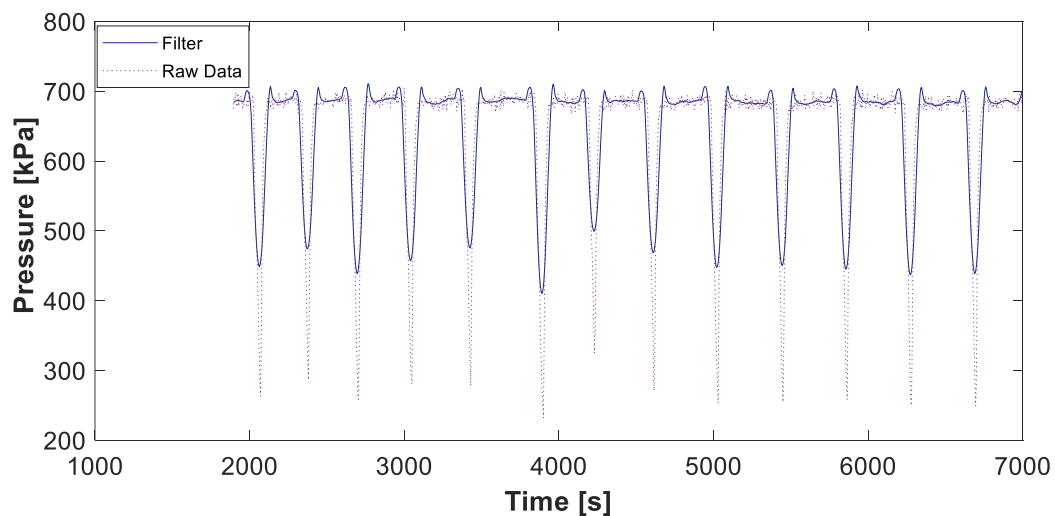


Figure 65- Filter data versus raw data of pressure at State 1 of the vapor compression cycle

5.1.2 Heating load

To calculate the load of the condenser for the mini-split, a vapor compression cycle model needs to be created. This model considers the four basic components, namely the evaporator, compressor, condenser, and expansion valve. During the modeling process, certain assumptions are made, which include isenthalpic expansion, no pressure drops through the heat exchangers, and constant superheat and subcooling. Thermophysical properties are calculated using CoolProp [51].

The condenser model utilized the lumped method, assuming it to be entirely two-phase refrigerant. For accurate heat transfer prediction on the air-side, the partially-wet/partially-dry method was implemented. The condenser is divided into two separate lumped analyses, fully wet and fully dry, with the separation point determined iteratively by analyzing the point where the condenser surface temperature equals the dewpoint temperature of the moist air. The entire heat exchanger is simulated using the ϵ -NTU method (Equation 92-94) and assumes constant pressure is equal to saturation pressure. The effectiveness (ϵ), number of thermal units (NTU), and overall conductance (UA) are used in Equation 92 and 93. Then in Equation 94 T_{cai} is the air side inlet temperature of the condenser, T_{cond} the temperature of the refrigerant of the condenser and \dot{m}_a the flow rate of the air. The air-side and refrigerant side heat transfer coefficients are solved using the correlations seen in Appendix C.

$$\epsilon = 1 - e^{-NTU} \quad (92)$$

$$NTU = \frac{UA}{\dot{m}_a} \quad (93)$$

$$\dot{Q}_{cond} = \epsilon \cdot \dot{m}_a \cdot c_{pa} \cdot (T_{cai} - T_{cond}) \quad (94)$$

Figure 67 shows that the mini-split cycles on and off, resulting in a semi-empirical quasi-steady with a heating load of around 1.5 kW. The sudden spikes in the load correspond to when the mini-split system turns on. This periodic behavior suggests that the mini-split may be oversized for the habitat, as it is designed according to AHRI Standard 210-240. That it has a rated cooling capacity of 1.5 RT. For cooling its rated at 57 Hz compressor speed. Indoor dry bulb of 80 °F, indoor wet bulb of 67 °F, and outdoor dry bulb of 95 °F. Inside unit takes up 1/3 of the dome. Figure 67 illustrates the difference between the experimental and analytical results, considering only the heating portion of the load from the experimental data. The predictions of the heating

loads from the analytical model are in line with the experimental data with an absolute error of 7.1%, except for a deviation at approximately 2,500 seconds. The variation in the systems could be due to the assumptions made in the analytical model, including assuming constant superheat and subcooling based of the rated conditions of the system. This implies that the system has an ideal expansion valve and an accurate refrigerant charge, respectively. In reality, variations occur and can be accounted for by using more detailed measurements of the unit.

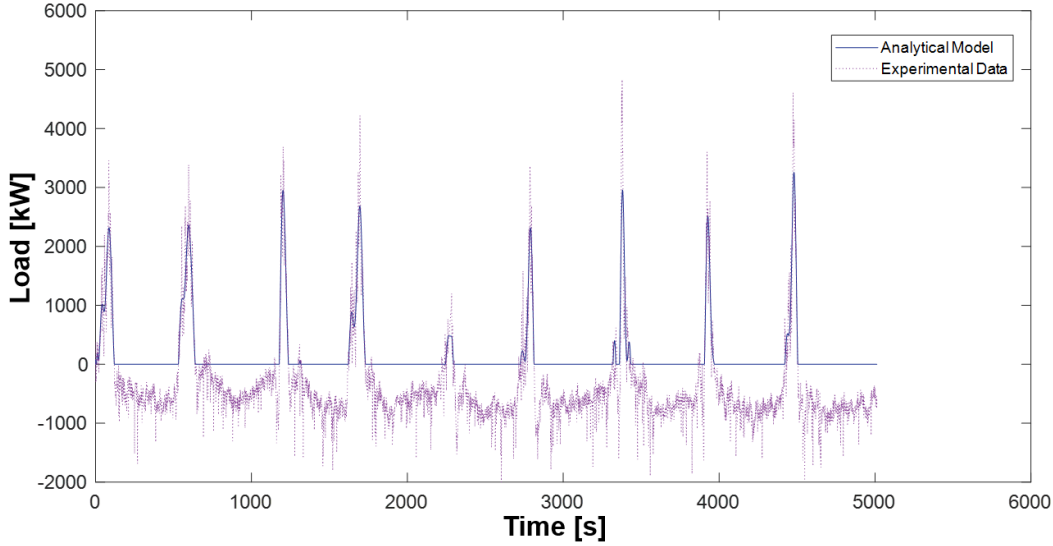


Figure 66-Heating load experimental data versus analytical model

5.1.3 Infiltration Load

The supply air into the habitat is used to calculate the infiltration load, by calculating the flow rate and the temperature differences seen in Equation 95. To test the system's response to heating, the temperature is increased inside the bladder and then monitored for an hour to see how it drops until it reaches steady state [24].

$$\dot{m}_e = \frac{\rho_{01}}{p_{01}^{1/\gamma}} \left(\frac{2}{\gamma + 1} \right)^{\frac{1}{\gamma-1}} A_e \sqrt{\frac{2\gamma p_{01}^{1/\gamma}}{(\gamma + 1)\rho_{01}}} p_0^{\frac{\gamma+1}{2\gamma}} \quad (95)$$

where \dot{m}_e is the mass flow rate exiting (kg/s), ρ_{01} is the initial density (kg/m^3), γ is the ratio of the specific heat of air, p_{01} is the initial pressure of the pressure box (the pressure of the pressure

box at the beginning of the experiment, Pa), p_0 is the interior pressure of the pressure box (Pa), and A_e is the effective area of the orifice (m^2).

To test the infiltration the mini split was set to a setpoint temperature of 25 Celsius. When the temperature reached a periodic steady state, the mini split was turn off as it is seen for the first 400 seconds of the data recollection in Figure 68. Do to leakages of the bladder the temperature is increased instantly and causing the temperature to 20 Celsius (the room temperature) in 2000 seconds.

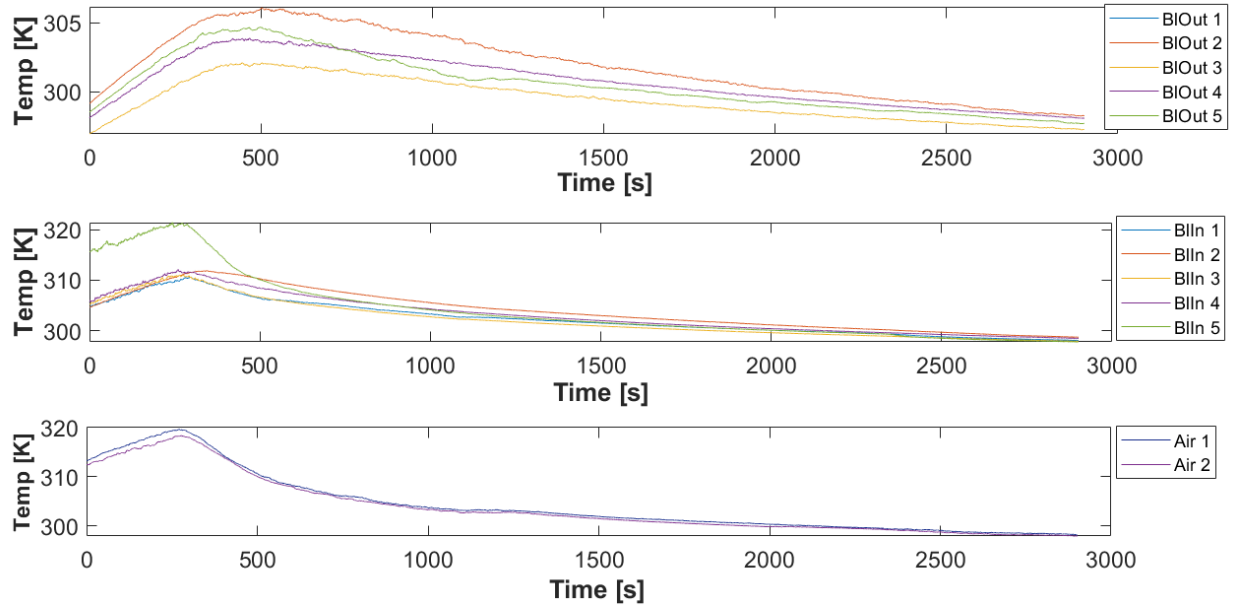


Figure 67- Temperatures of the bladder out thermocouples (a) , bladder in temperatures (b) and bladder air temperatures (c) of the heating infiltration testing

5.1.4 System Parameter Identification

The thermal resistances for each layer in the wall panel were estimated using their respective material properties and dimensions (thicknesses) explain in Chapter 3 [52] seen in Table 14.

First, the model was tuned to match the quasi-steady-state experimental results by adjusting the steady-state parameters, which included the thermal resistance and capacitance of the bladder made of polyester. An error function was set up using Equation 96, and the cumulative error Error_{ss} for 120 steady-state data points at different temperatures was minimized using the

MATLAB function `fmincon`, which finds the minimum of a constrained nonlinear multivariable function using numerical optimization techniques to iteratively search for the optimal values of the variables that minimize the objective function while satisfying the constraints. The resistance and capacitor values were experimentally measured and theoretically obtained from different manufacturers, ranging from 0.00001 W/(K) to 0.8 W/(K) and 110 J/(K) to 6 J/(K), respectively [52]. These were used as lower and upper bounds in the optimization function for the resistance, and the initial guess values for resistances and capacitors can be found in Table 14. The internal mass capacitor value was also optimized using the same approach, and practically the same value was obtained as the one given theoretically, with a range from 223 J/(K) to 45 J/(K) [52].

$$\text{Error}_{ss} = \sum_{i=1}^{120} \left[\sqrt{(T_{blin,expt} - T_{blin,model})^2 + (T_{blout,expt} - T_{blout,model})^2 + (T_{air,2,expt} - T_{air,2,model})^2} \right] \quad (96)$$

Table 14- Optimization of resistance values

	Literature value	Optimize value	Units
$R_{bladder}$	0.000037465	0.000028716	K / W
$C_{bladder}$	2.54	9.62	J/ K
C_m	26.5692	26.5572	J/ K

The goal is to match as close as possible the air temperatures by taking account that thermocouples have a systematic error of approximately 1 K.

Capturing the infiltration load accurately can be challenging due to the numerous factors that can vary across different experiments, including the humidity level of the bladder and the laboratory conditions. Calculating the infiltration load involves determining the difference between the energy required to maintain the desired temperature inside the space and the actual energy consumed by the HVAC system. However, the presence of various sources of error can affect the accuracy of this calculation.

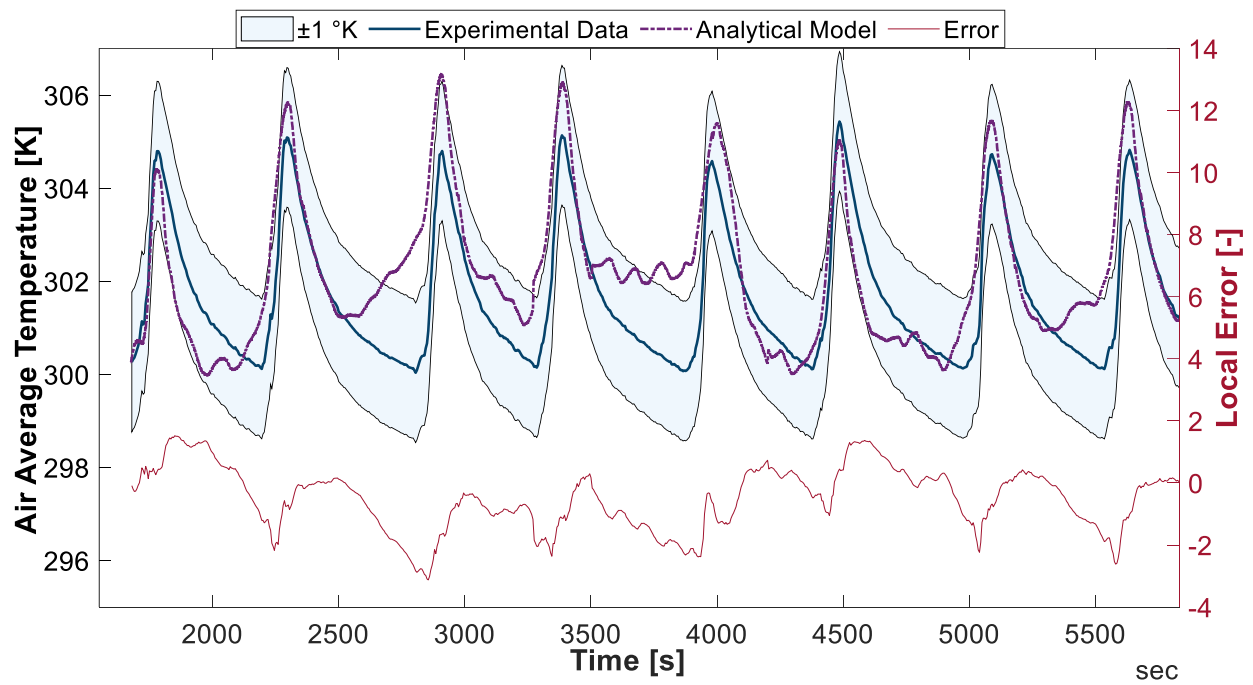


Figure 68- Experimental vs analytical model with the local error for average air temperature

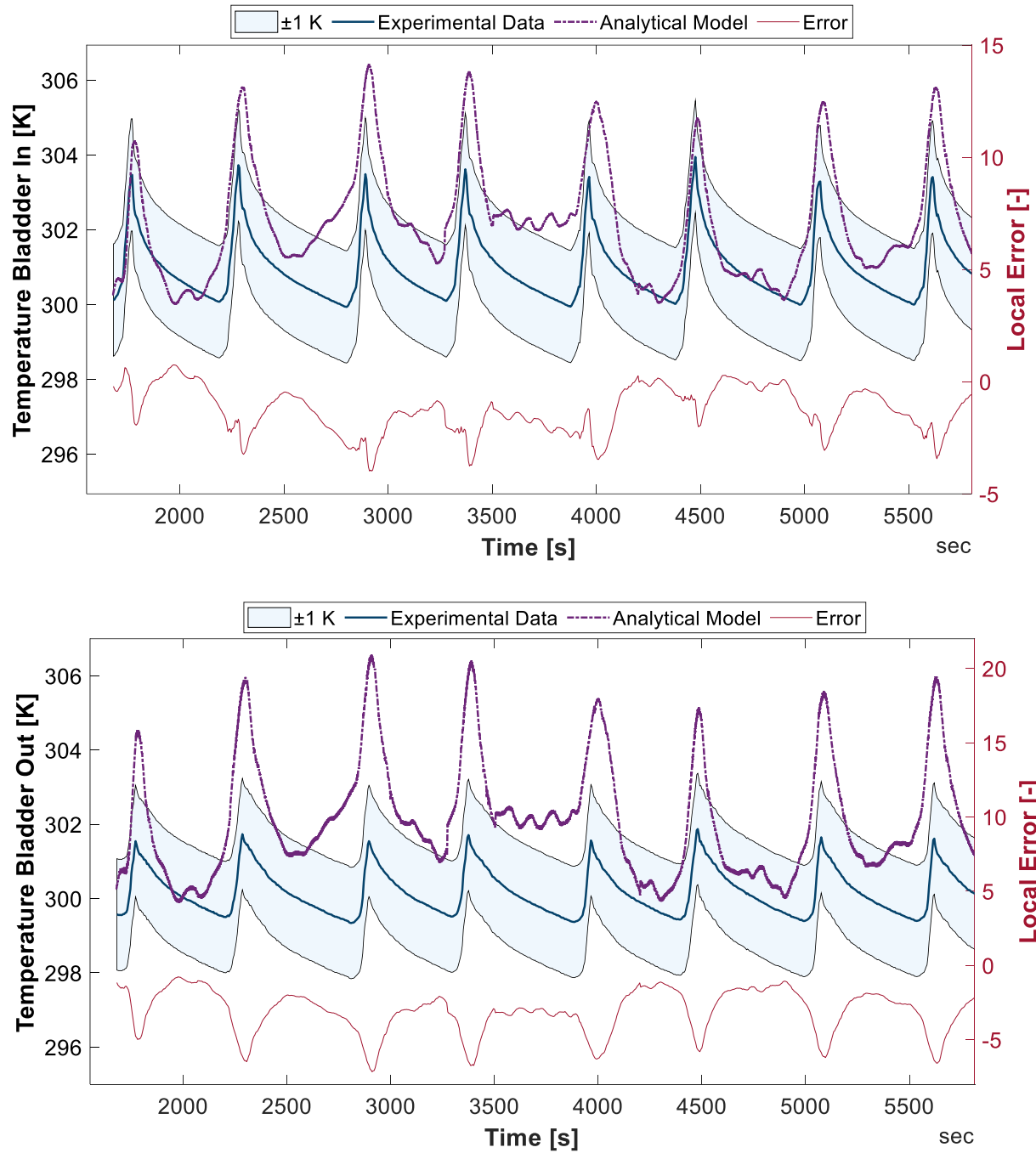


Figure 69-Experimental vs analytical model with the local error for bladder in temperature (a) bladder out temperature (b) in max heating scenario of the mini-spit system

As it can be seen in Figure 69, the higher temperature decay observed in the experimental data versus the model can be attributed to the air leaving the bladder, which can impact the infiltration load. To accurately estimate the infiltration load, it is necessary to account for factors such as the building envelope, air exchange rates, mechanical ventilation, environmental conditions, and experimental conditions. This can be achieved through the use of appropriate measurement techniques and analytical tools that can adjust for these factors and minimize sources of error in the calculation.

Figure 70 the error could be from the thermocouples reading the air temperature except of reading the bladder temperature. As the dome blows up the nylon is tighter causing the epoxy to come out and making the thermocouple read the air temperature.

5.2 Emergency Heating Scenario: Test B

Running the mini-split system at an emergency scenario means that the unit is designed to operate in extreme conditions, such as during a fire or in extremely cold temperatures, where it is essential to maintain a certain level of heat in the space. In this mode, the mini-split system is programmed to continue providing heat even after it has reached the set point temperature, and it will adjust its heating output to maintain the temperature around the set point of 24 Celsius without shutting down for 30 minutes. It is important to note that running the mini-split system in emergency mode for extended periods can result in increased energy consumption, and it may cause the unit to wear out more quickly.

The data presented in Figure 71 depicts the results obtained from running the mini-split unit in heating emergency mode. It is observed that during the initial stage, the mini-split system takes longer to activate compared to normal heating scenarios, requiring an additional 120 seconds to turn on.

The transient state is also prolonged, as the unit initially operates at full power and mass flow, gradually adjusting to the bladder's conditions. The longer transient state is likely due to the emergency mode, requiring the unit to work harder to maintain the set temperature.

After approximately 1100 seconds, the mini-split reaches a steady state, and the inside and outside unit temperatures remains constant as well as the pressures and mass flow of the refrigerant. However, at the end of the experiment, there is a sudden drop in temperature, pressure, and mass

flow. This sudden drop is due to the unit shutting down abruptly, which is due to safety feature made by the manufactures so the unit doesn't break.

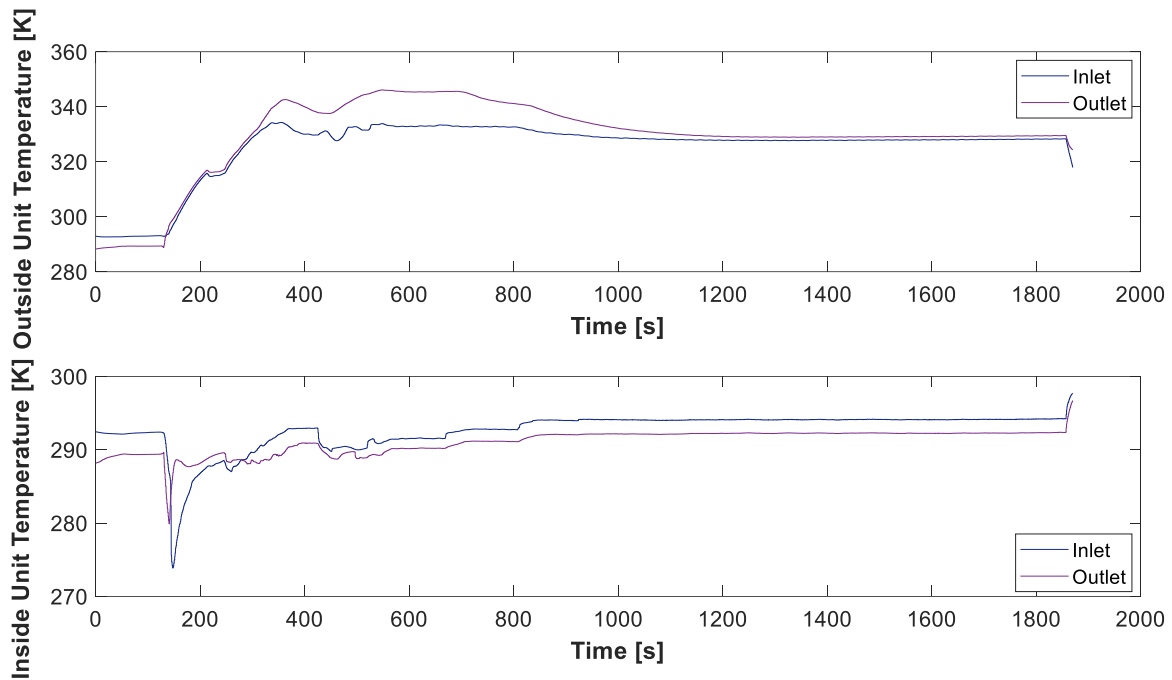


Figure 70- Experimental data of the mini-split running outside unit temperatures (a) and inside unit temperatures (b) at emergency mode Part 2

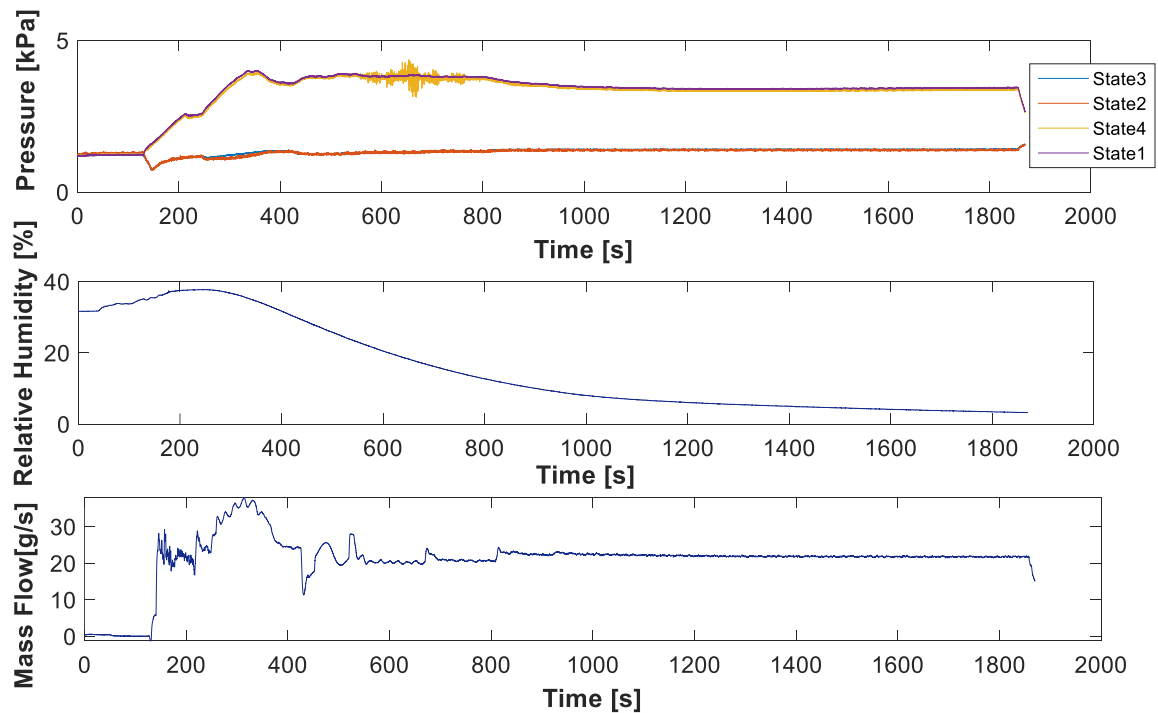


Figure 71-Experimental data of the mini-split pressure (a), relative humidity (b) and mass flow (c) running at emergency mode Part 1

It seems that there is a temperature gradient in the bladder (Figure 73) with respect to their proximity to the mini-split, with the bladders closer to the mini-split having higher temperatures. This observation is based on the readings from thermocouples placed at positions 2, 5, and (Figure 73) 4. It is also noted that there were some data acquisition issues with the temperature readings from bladder 5 at the beginning of the simulation, which were resolved when heating started.

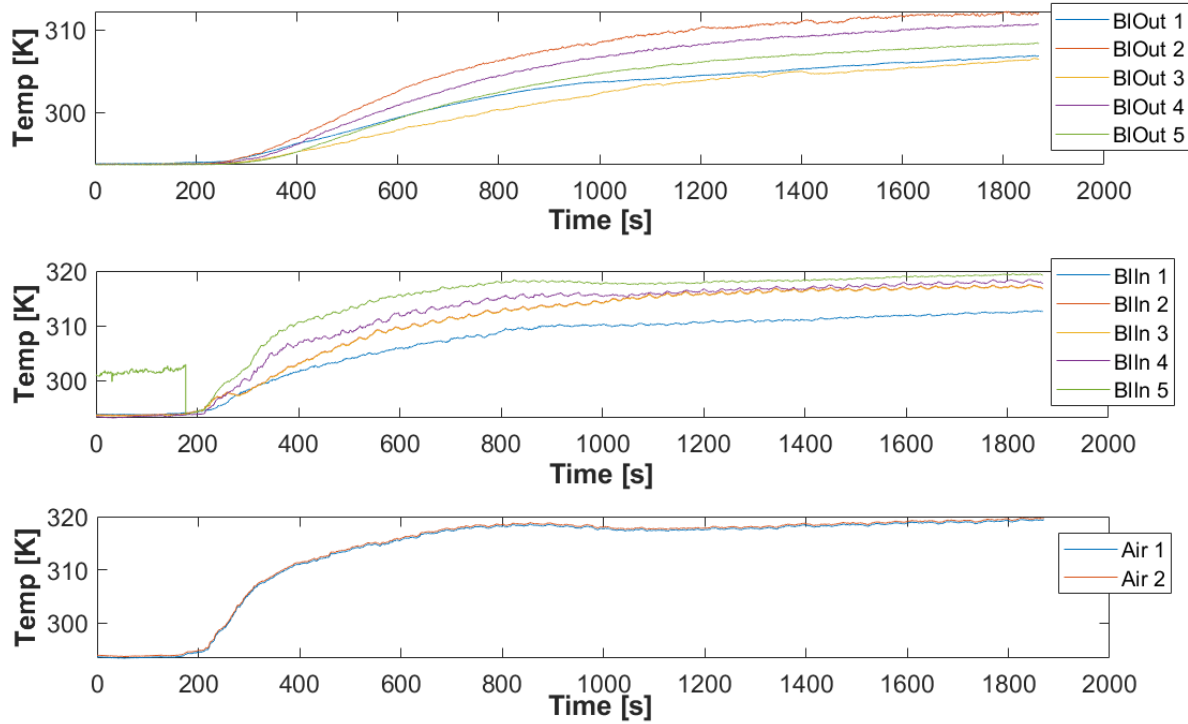


Figure 71-Experimental data of the thermocouples of the bladder out temperature (a), the bladder in temperature (b) and air temperature (c) at emergency mode

Figure 74 indicates that a significant amount of heat transfer is being lost from the bladder to the structure, compared to the rest of the layers. This suggests that the convection gap between the two layers is considerable. At the end of the simulation, the outside layer of the bladder is at a temperature of approximately 312K, while the structure maintains an average temperature of 298K. The remaining layers show a temperature drop of approximately 2K.

As more layers are being considered for Test B, an optimization process is necessary. This optimization aims to maintain the resistance values obtained from Test A. Although a significant temperature change occurs from the bladder to the structure, the convection resistance in this case varies with temperatures and cannot be optimized to a fixed value, as previously stated. Therefore, only the resistance of the aluminum panel can be optimized in this case seen in Equation 97.

$$Error = \sum_{i=1}^N \left[\sqrt{(T_{aluminum,panel,expt} - T_{aluminum,panel,model})^2} \right] \quad (97)$$

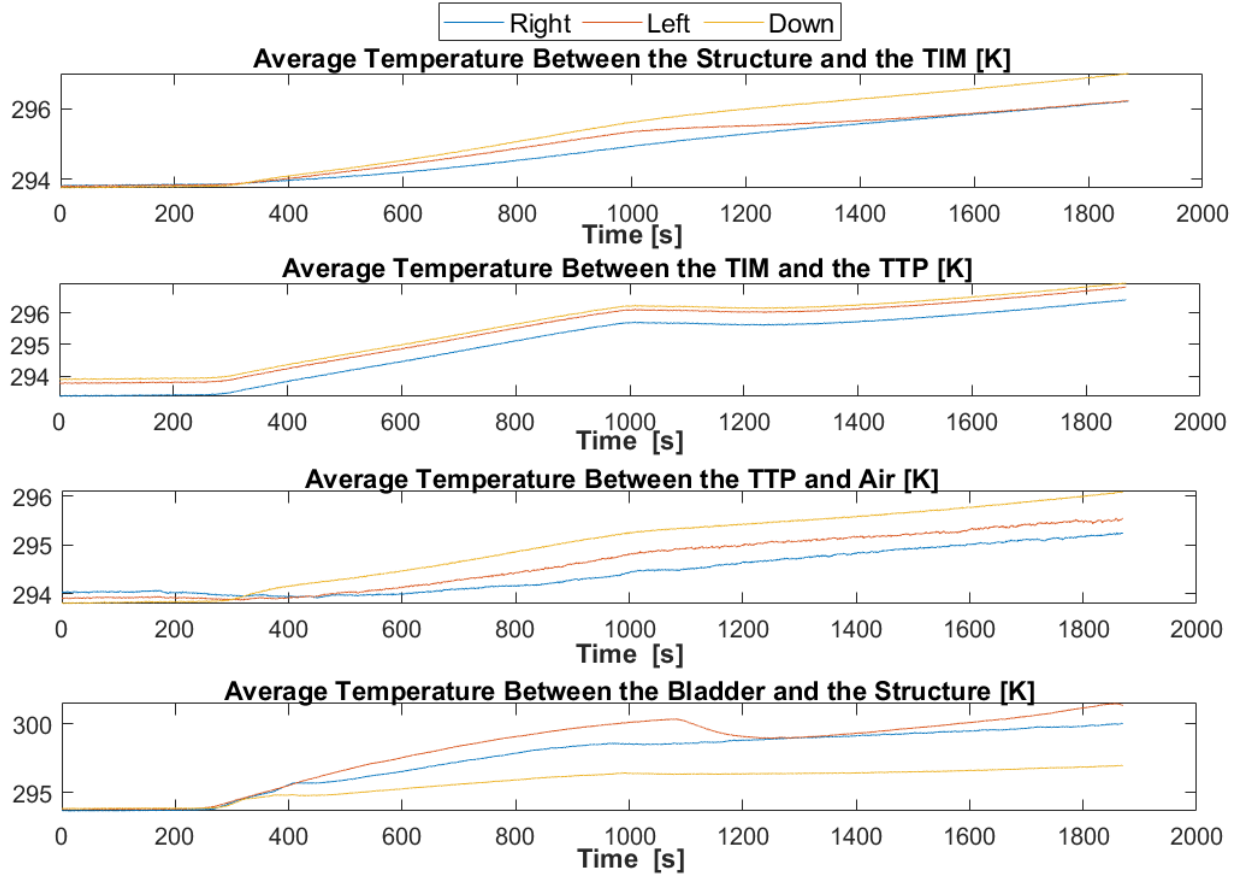


Figure 72-Experimental data of the thermocouples at the layers of the CPT at emergency mode

The thermal resistance of the aluminum panel was initially assumed to be 0.00001K/W, but after optimization, it was increased to 0.00002 K/W that is within the boundary condition of 0.02 to 0.00001 K/W. The resulting analytical model was then compared to the temperature data obtained from the experiments. The conclusion drawn from Figure 75 on the top, which compares the average air temperatures of the bladder and provides accurate results due to an understanding of the thermal load the mini-split brings into the dome. However, the results in Figure 75 on the bottom vary more due to convection between the structure and the bladder, as well as convection between the aluminum plate and lab conditions. It is assumed that the lab conditions remain constant throughout the experiment, but it's possible that the temperature in the lab dropped, which may explain why the initial data matches more closely than later data since the analytical model is

trying to reach the lab conditions of 296K. Also, it is possible that the heat transfer being considered is higher than what is occurring due to losses between each of the layers, which could be caused by the conduction gaps. To better understand this behavior, further tests will be conducted.

The mini-split appears to be exhibiting unusual behavior, potentially due to superheating caused by abnormal pressure readings. Additionally, there is a minimal temperature difference between the inlet and outlet temperatures of the inside and outside units even after 1000 seconds, which may be due to the unit being oversized. To investigate further, the fan will be operated at low speed in the next experiment and a load will be added to the system to determine if the mini-split can reach a periodic state.

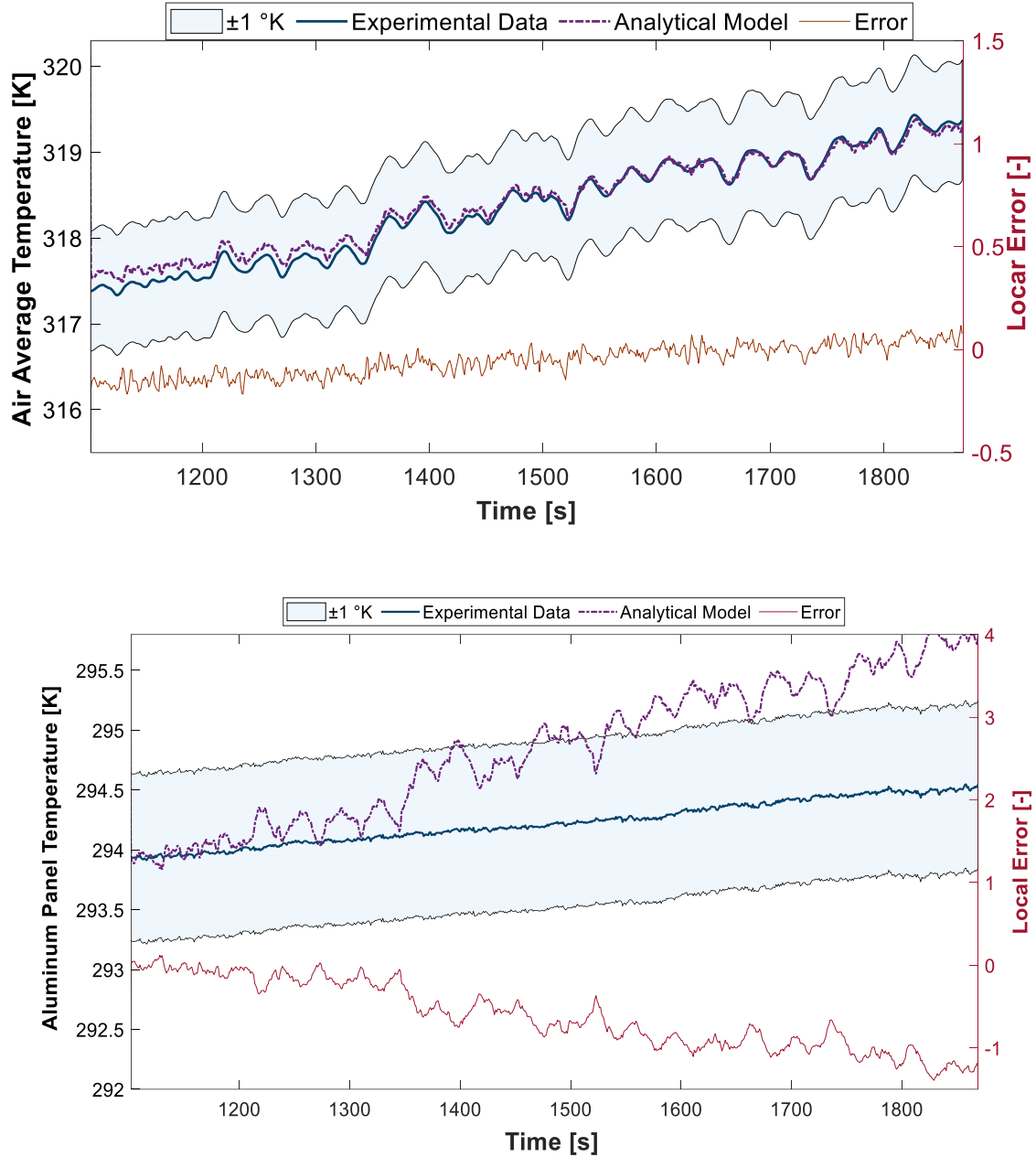


Figure 73-Experimental vs analytical model with the local error for air bladder temperature (top) and aluminum plate temperature (b) in emergency scenario of the mini-split

5.3 Heating load Scenario: Test B

In order to assess the accuracy of the analytical model in predicting the effect of an internal load in the bladder, a 1.5kW heater and four 250W lamps were used to simulate the load. Figure 76 illustrates the experimental setup, where the mini-split was turned off with a constant pressure

and no flow rate. As the temperature of the bladder increased due to the internal load, the temperatures inside the unit also increased. The temperature of the outlet of the outside unit also increased as the refrigerant was warmed up, although it was still lower than the temperature inside the unit. On the other hand, the temperature at the inlet did not increase due to the presence of the expansion valve between the inlet and the outlet. These observations were then compared to the predictions of the analytical model to evaluate its accuracy in simulating the effects of an internal load in the bladder.

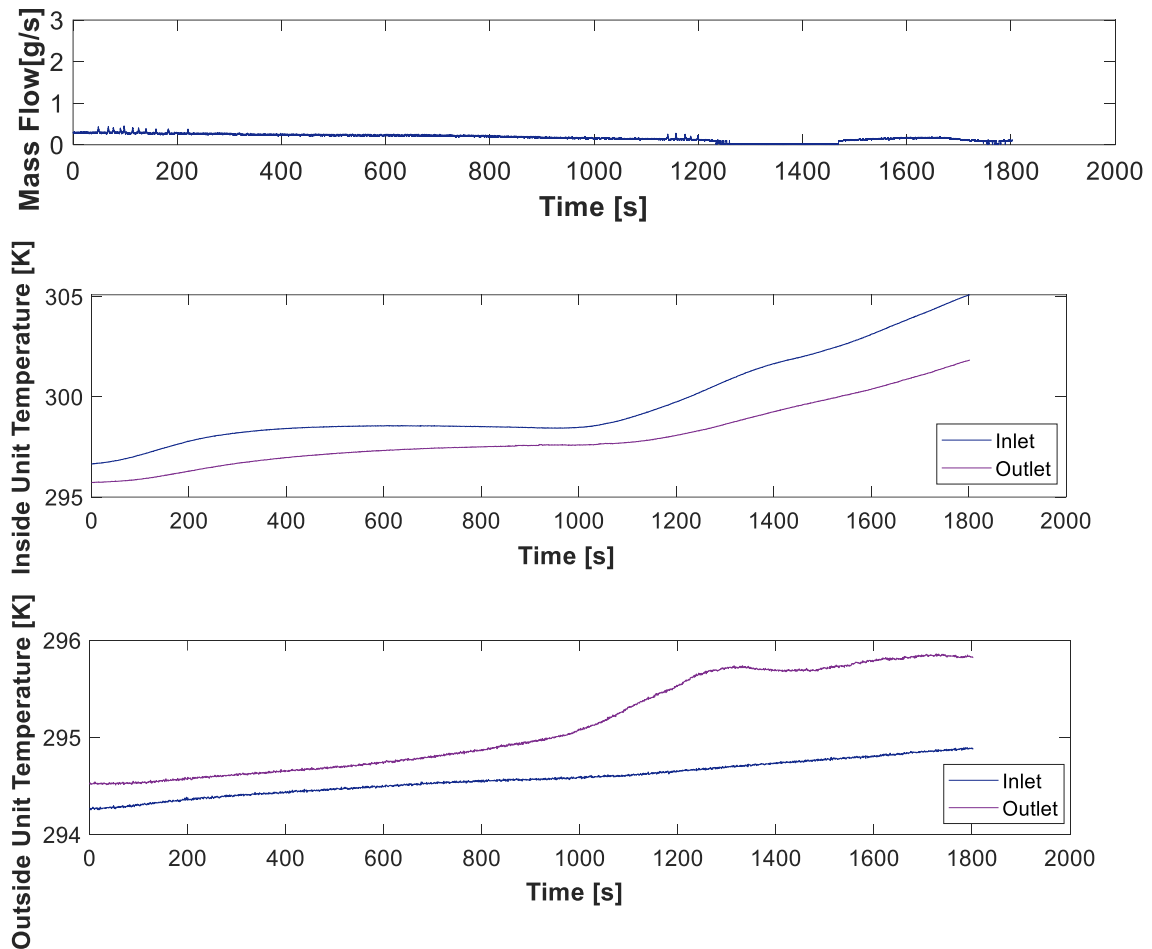


Figure 74-Experimental data of the mini-split not running

Initially, the temperatures showed a slow increase, likely due to power outages caused by high amperage (Figure 76). However, after a better approach was implemented to provide power to the heater and lamps, the temperature began to increase rapidly at around 1200 seconds. This trend in temperature closely matched the results from previous experiments.

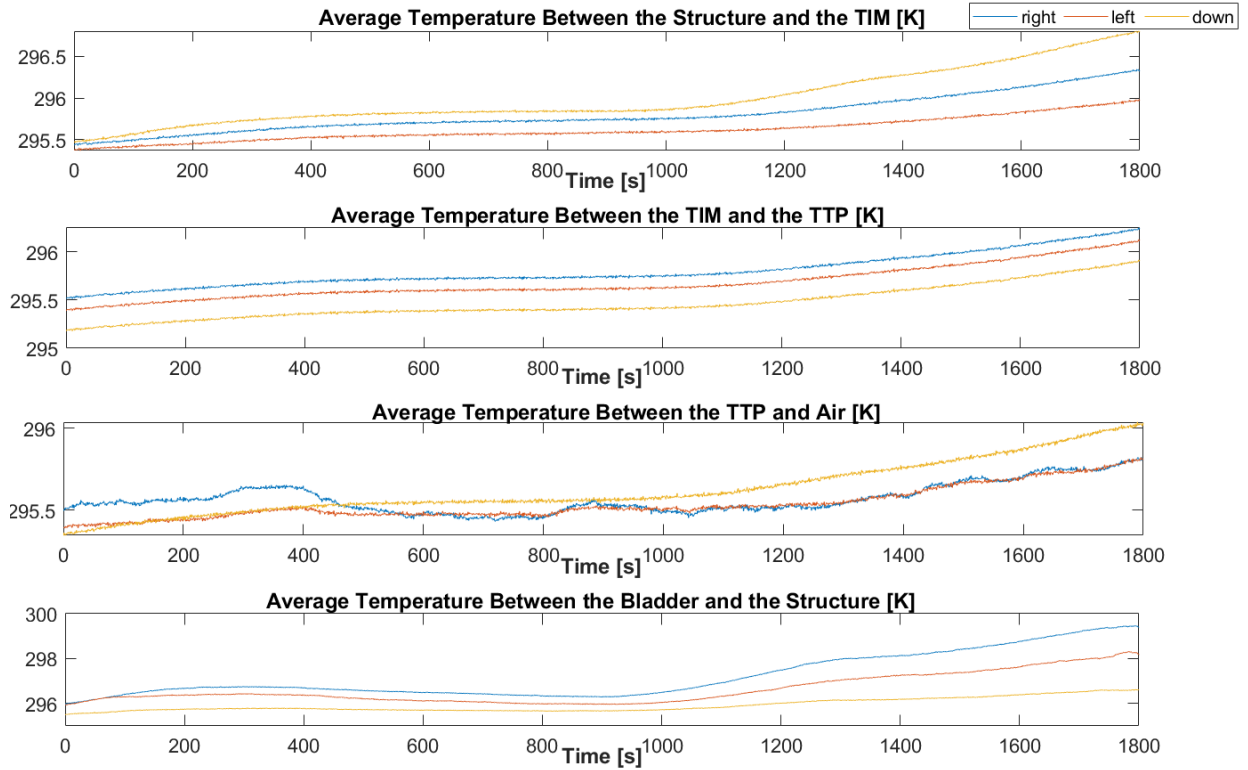


Figure 75-Experimental data of the thermocouples at the layers of the CPT with heaters

Figure 77 illustrates that the temperature of the bladder at location 5 is significantly higher and exhibits a different dynamic compared to the other temperatures. This is likely due to the location of the thermocouple, which is directly above the heater and therefore receives more heat. The dynamics observed in the temperature of the bladder at location 5 are consistent with those observed in the bladder air temperatures.

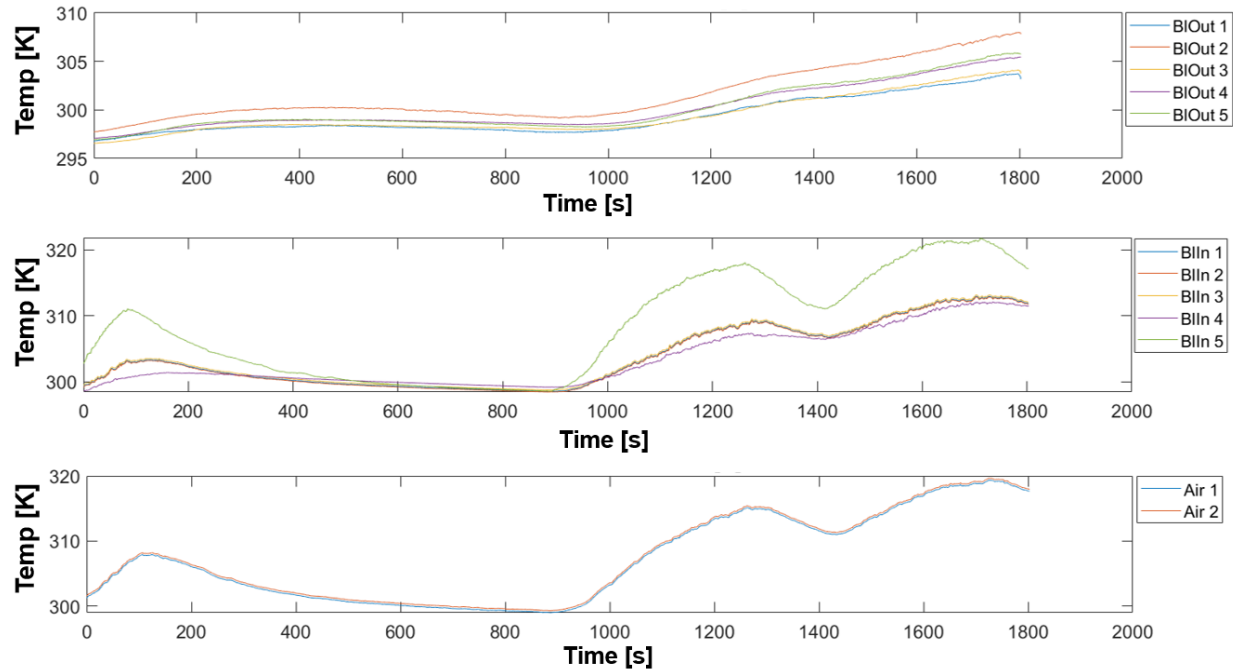


Figure 76-Experimental data of the thermocouples of the outer bladder temperature (a), inner bladder temperature (b) and air bladder temperature (c) with no-mini split

The experimental data is compared to the analytical model computation in Figure 79 of the thesis. The top Figure of 79 shows the average air temperature, which gives results similar to the experimental data except for the beginning. The offset at the beginning is due to the initial conditions during the model computation. The comparison of aluminum panel temperature in the bottom Figure of 79 shows more discrete results. Heat transfer across an interface takes place through both solid contacts and interstitial gaps, such as air. In this scenario, the conduction through contact spots is minimal since the bladder only slightly touches the structure. Therefore, most of the heat transfer occurs through gas conduction. Radiation heat transfer through the interstitial gap is disregarded since it is only significant at temperatures above 300 degrees Celsius, as is the convection through the gaps. As the gaps vary considerably throughout the dome, it is challenging to determine an average value to predict it.

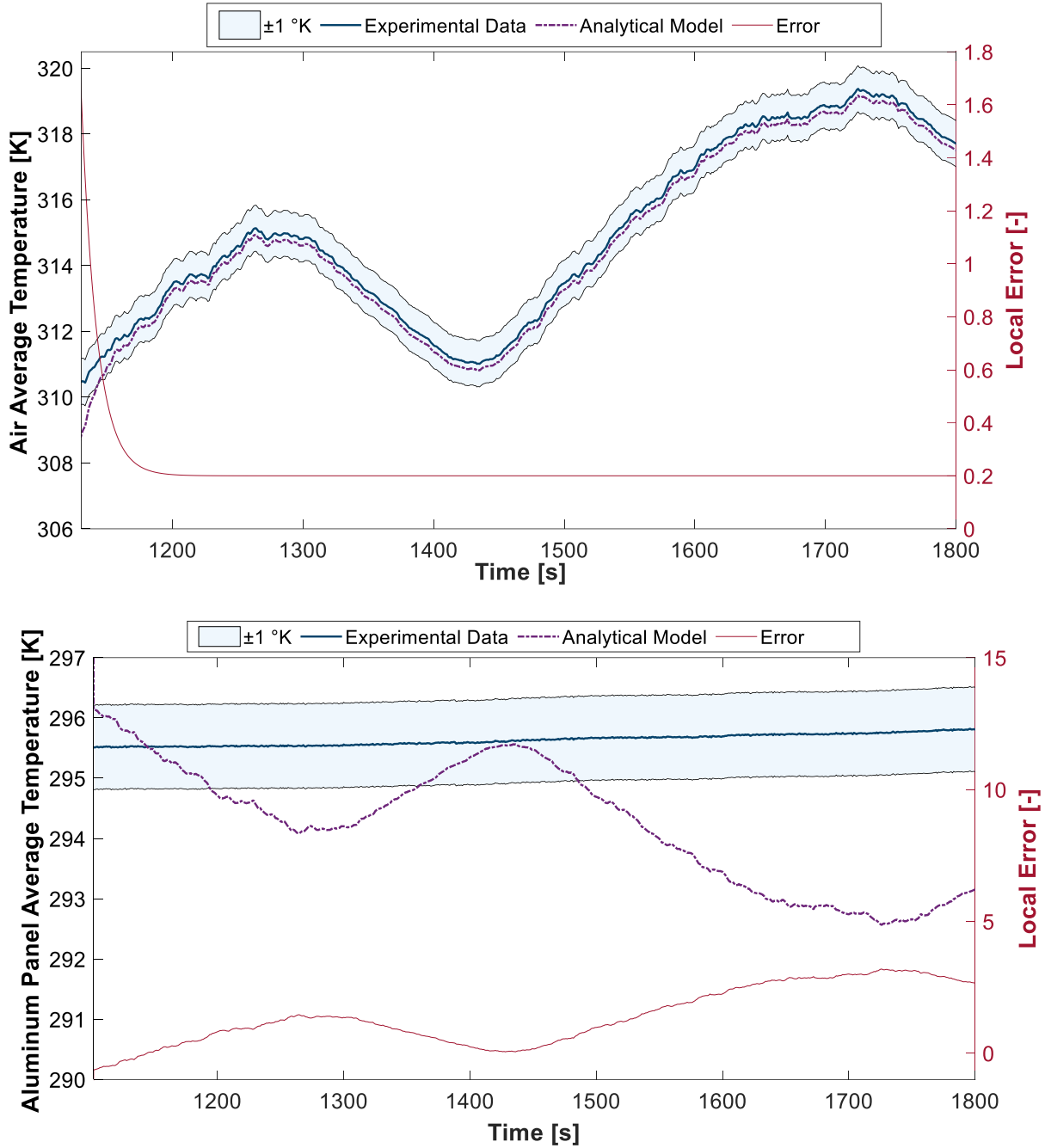


Figure 77-Experimental vs analytical model with the local error for air bladder temperature (a) and aluminum plate temperature (b) with heaters

5.4 Cooling Scenario at setpoint 16 C with heating load: Test B

Figure 80 when a heating load is added, the mini-split remains off until the air temperatures reach 320K, after which the mini-split is turned on and the temperatures start to drop non-linearly

due to the mini-split operating in a transient state. At 1,200 seconds, there is a peak where both the outside and inside units have around 20K of temperature difference between its outlet temperature and inlet temperature, indicating the optimal point to calculate the thermal load going into the system. However, the mini-split does not maintain the same behavior and the temperatures of the unit match again, leading to the conclusion that the compressor may be flooded.

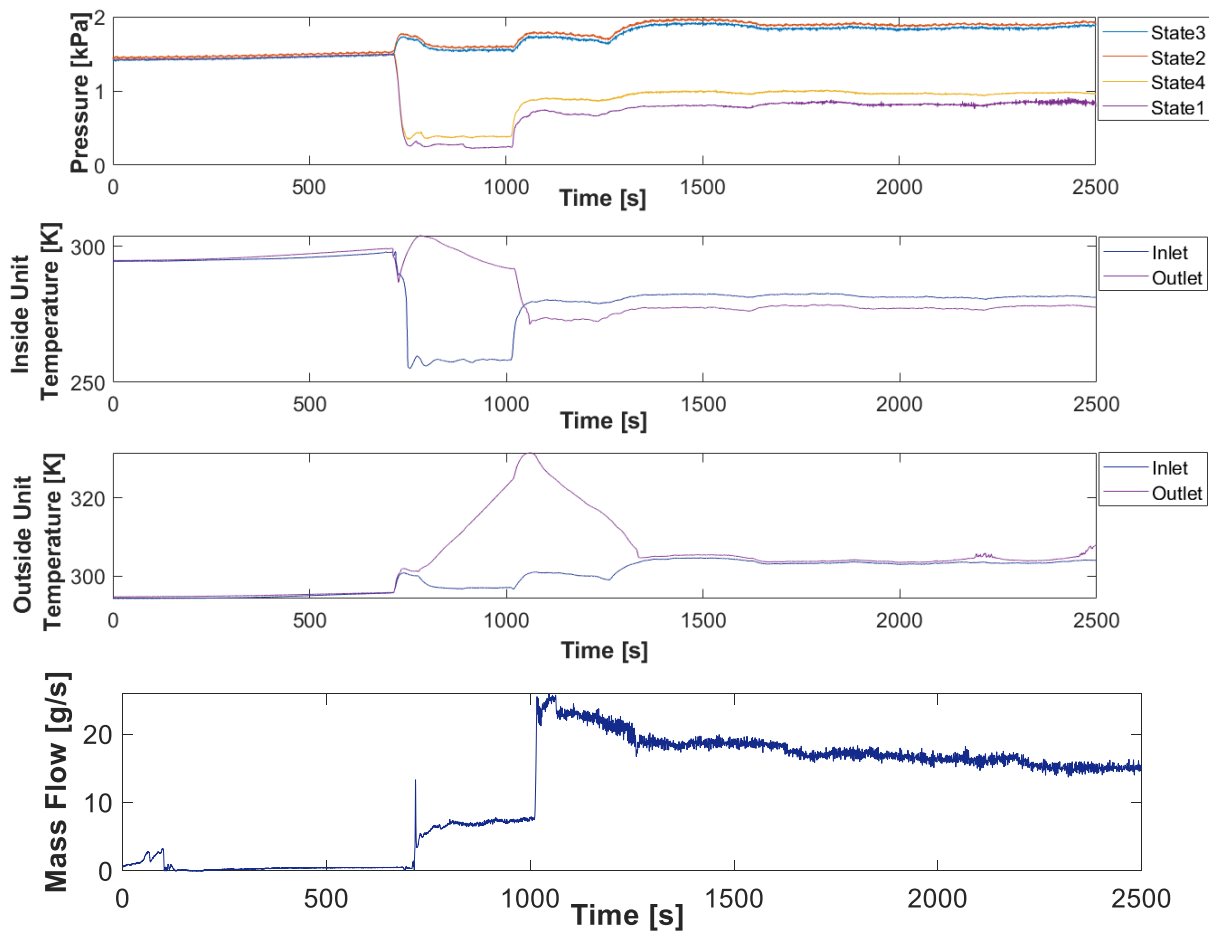


Figure 78-Experimental data of the mini-split running at cooling mode

The experiment showed that at the beginning of the heater's operation, the temperature in the bladder increased by approximately 20 K, while the temperature in the structure increased only by around 5 K, and the rest of the layers had an increase of about 1 K (Figure 81). This temperature distribution is consistent with previous testing and indicates a significant conduction gap between the bladder and the structure. Additionally, the experiment reached a periodic steady state after approximately 1200 seconds, where the air temperature fluctuation was within a couple of degrees.

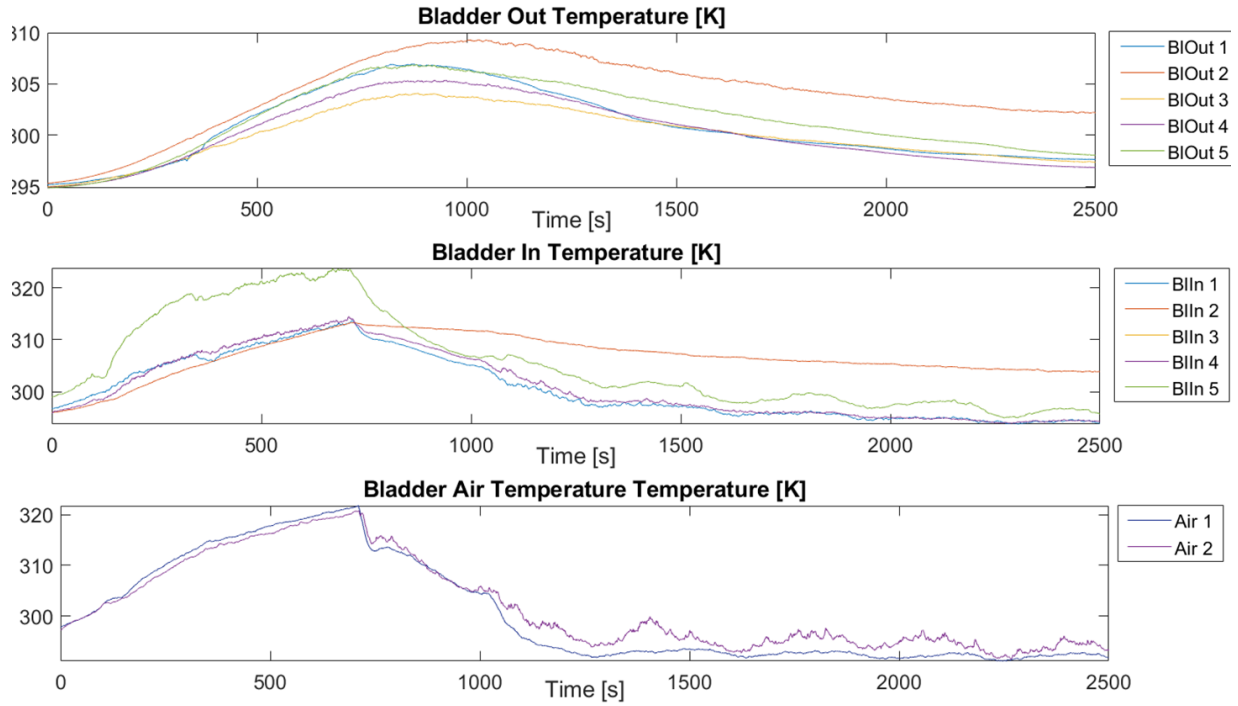


Figure 79-Experimental data of the thermocouples of the bladder at cooling mode

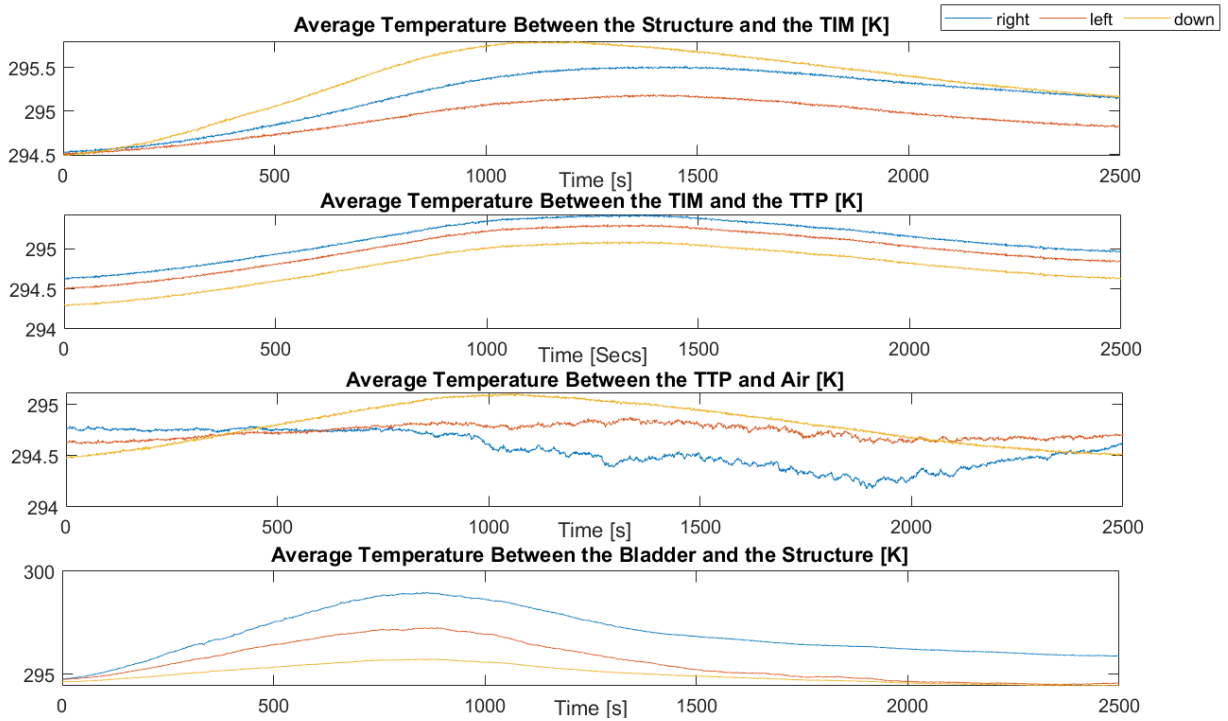


Figure 80-Experimental data of the thermocouples at the layers of the CPT at cooling mode

To calculate the cooling load of the system, it is necessary to obtain the periodic steady state of the mini-split, which occurs after approximately 1200 seconds of operation. The evaporator model also uses the lumped method. The entire heat exchanger is simulated using the ϵ -NTU method seen in Equation 98 assuming the constant pressure is equal to inlet pressure.

$$Q_{evap} = \epsilon \cdot \dot{m}_a \cdot c_{pa} \cdot (T_{cai} - T_{evap}) \quad (98)$$

Figure 83 illustrates the comparison between the thermal load calculated from experimental data collected from the mini-split and the corresponding analytical model. The results show that, similar to the heating load, the analytical model accurately predicts the cooling load of the system when the mini-split operates as expected since the absolute error is 6.3%.

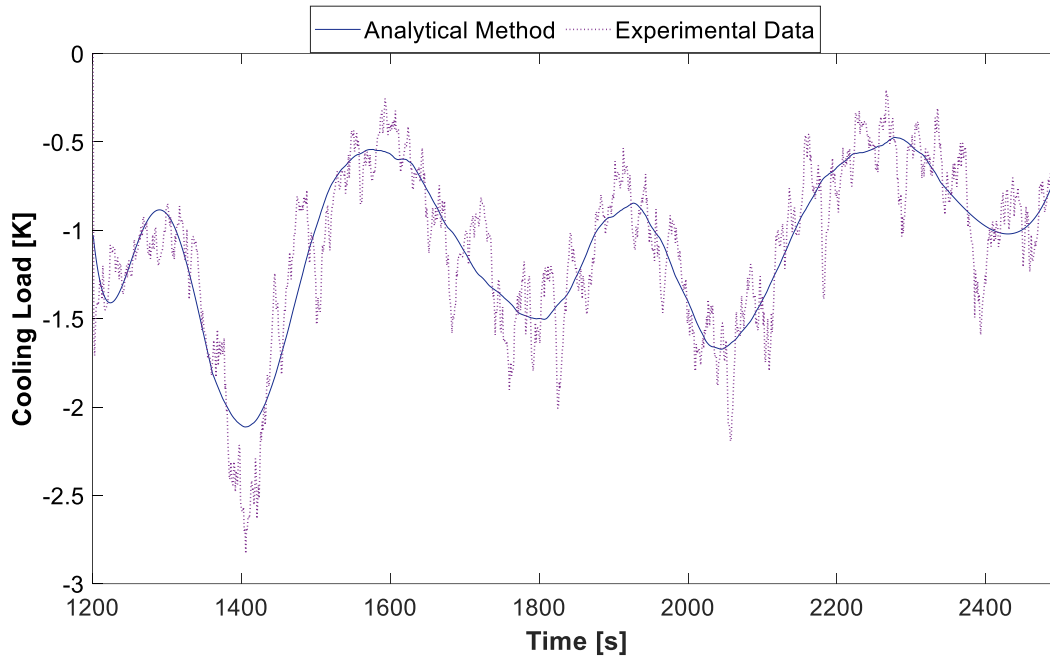


Figure 81-Cooling load experimental data versus analytical model

Lastly, the analytical air temperatures were compared with the corresponding experimental measurements, as well as the temperature of the aluminum plate. The results shown in Figure 84 that the analytical model accurately predicts the air temperatures, as previously observed in testing. However, unlike previous data, the temperature of the aluminum panel did not follow the same dynamics between the analytical and experimental results. Instead of returning to room temperature, the temperature remained constant and even dropped to around 295 K. This

discrepancy suggests the presence of conduction gaps between the layers, which may be contributing to the observed differences in temperature behavior.

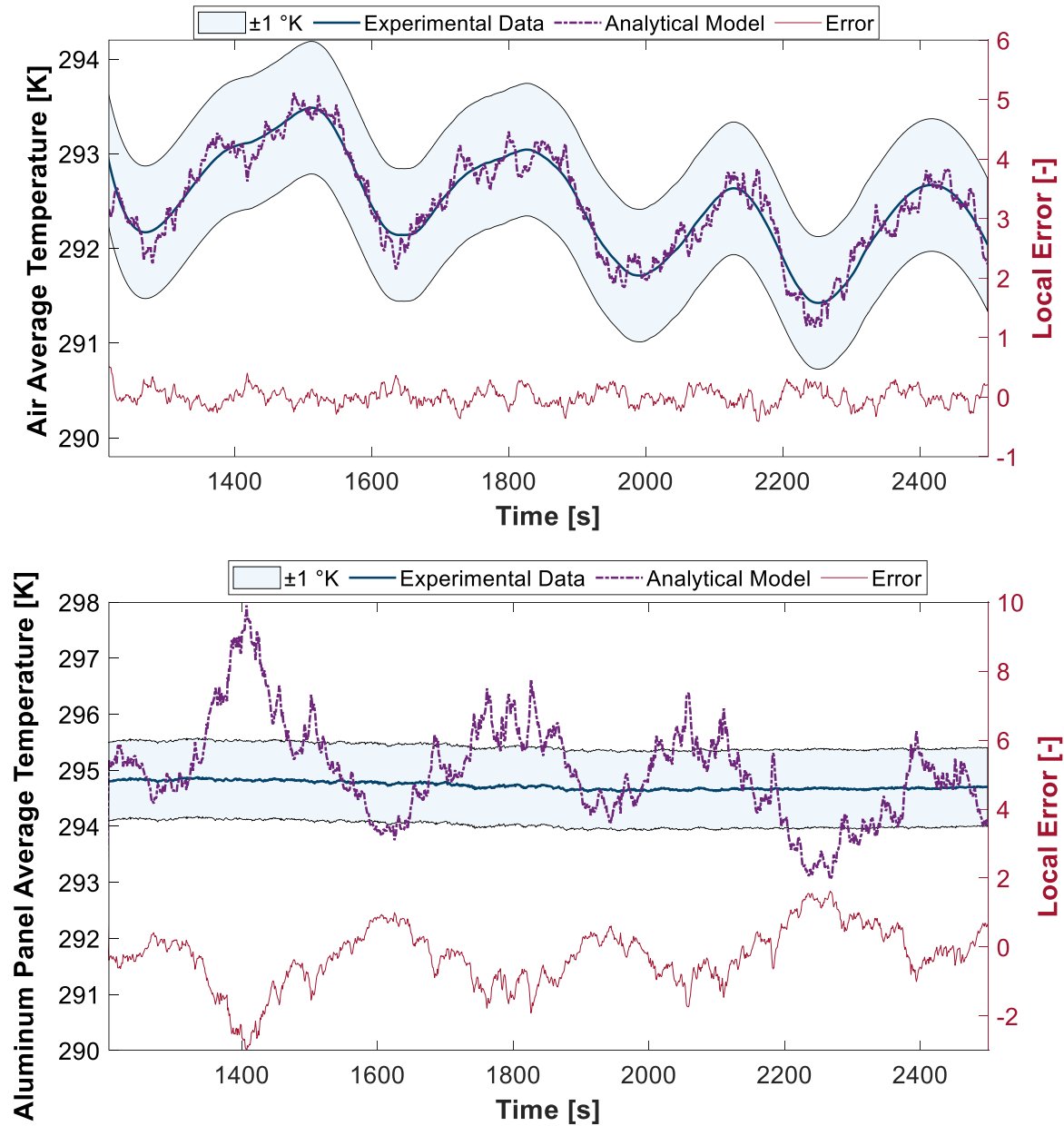


Figure 82-Experimental vs analytical model with the local error for air bladder temperature (a) and aluminum plate temperature (b) with cooling load

5.5 Thermal Transfer Panel: Test C

Following the execution of Test C, which involved the thermal transfer panel, Figure 85 displays the correlation between the analytical and experimental data for the panel's pressure drop calculations. The results indicate an absolute error of 0.03 between the two sets of data.

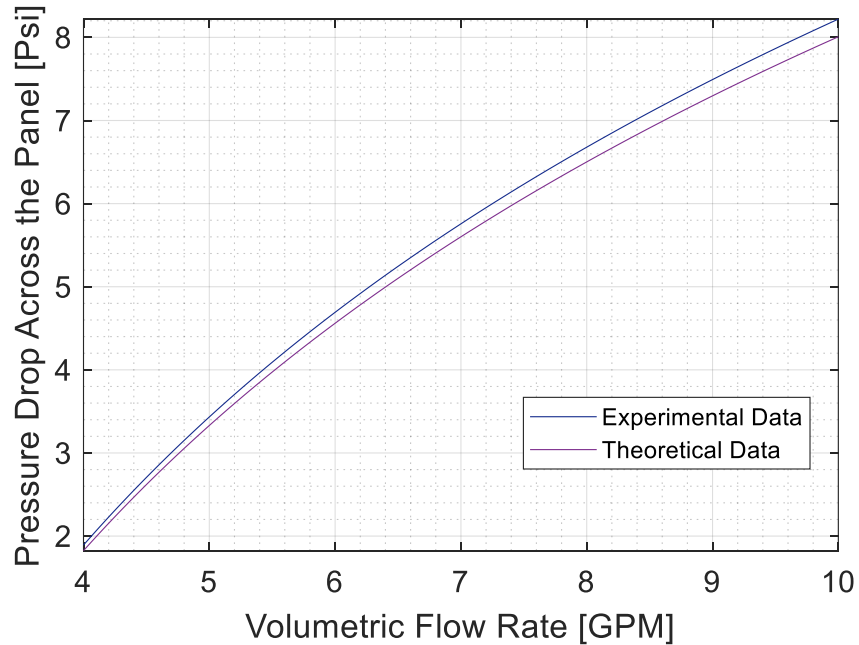


Figure 83-Pressure drop across thermal transfer panel

Figure 86 illustrates that as the temperature of the syltherm decreases, the volumetric flow rate increases slightly. Additionally, when the temperature of the syltherm reaches extreme values, either negative or positive, the pressure drop is higher. This implies that as the temperature deviates further from the laboratory conditions of approximately 22C, the pressure drop becomes more significant.

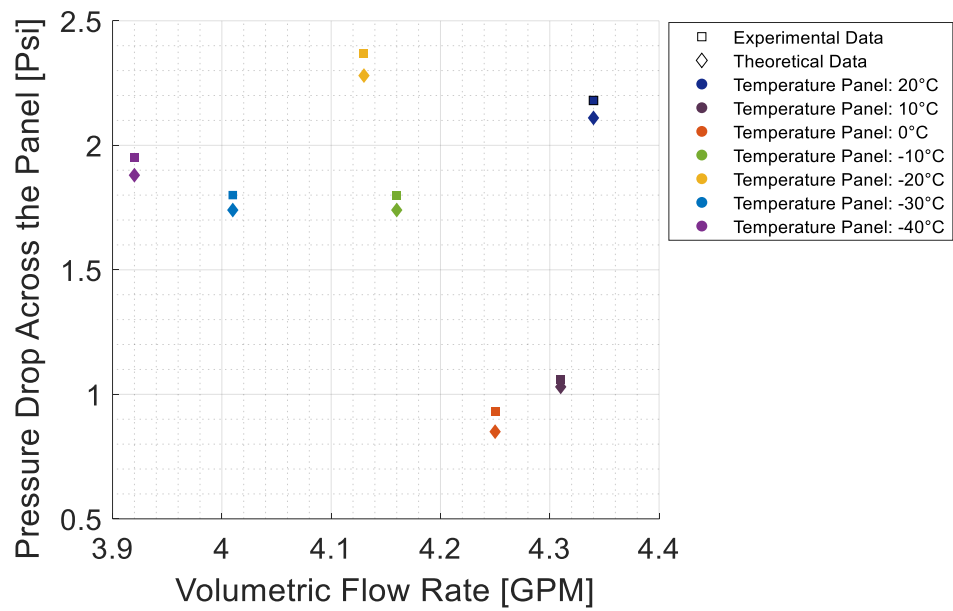


Figure 84-Temperature vs pressure drop of the system

Although the heat load increases slightly with the flow rate see in Figure 87, the difference is not significant. At certain points, such as at 18 degrees Celsius, both flow rates have the same value.

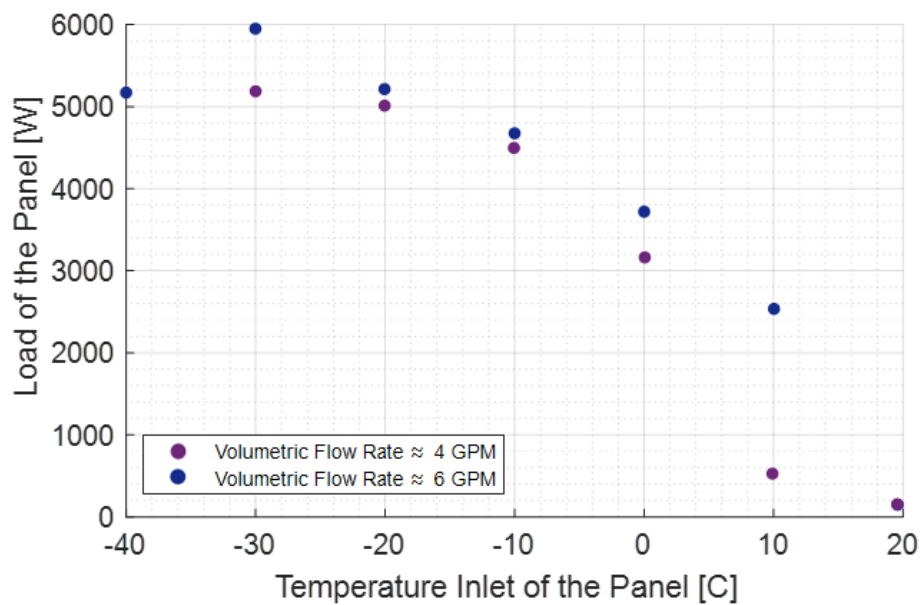


Figure 85-Load of thermal transfer panel at different flow rates

6. CONCLUSION AND FUTURE WORK

6.1 Conclusion

This thesis has presented the development of a numerical simulation of a lumped habitat interior environment in real time, with the requirements set by MCVT, using a methodology based on a thermal network approach. The simulation takes into account convection, radiation, and conduction, ventilation, and incorporates a humidity model, as well as leakage loads, internal gains, and cooling/heating loads from the HVAC system. Three different numerical approaches were tested, with the MATLAB implementation being found to be the most reliable.

The HIEM was found to be highly accurate in predicting the instantaneous temperature variations inside the bladder with a relative error of less than 3%. However, this accuracy is highly dependent on accurately predicting the loads in the environment such as ventilation, leakage, mini-split, and heaters, among others. For a relative error of less than 3%, the heat pump load needs to have an absolute error no greater than 10%. The heat transfer characteristics of the aluminum plate in the thermal transfer panel showed discrepancies up to 24% due to air gaps existing between the bladder and the panels, as well as additional heat losses.

6.2 Future Work

Further testing is required to validate the disturbances in the MCVT, which will require specialized installation to test the burning of materials and measure it appropriately. Researchers must wear appropriate protective equipment, and the laboratory conditions required for testing the burning of HVAC systems, chairs, or computers are highly specialized and must be designed and operated with the utmost care to ensure the safety of researchers and minimize the risk of damage to equipment or property. Additionally, to obtain more accurate results on the temperature of the aluminum plate, optimization of the thermal resistance between the gap of the bladder and the structure needs to be performed. Several factors such as precomputing any constants, reducing the number of data points, parallelizing the code, and utilizing a different optimization algorithm may lead to faster convergence.

APPENDIX A: SENSOR CALIBRATION

Pressure Sensors

Table A.1- Sensor Pressure Model

Sensor	Number of Sensors	Series number	Measurement Units	Description
Setra Pressure Transducer	3	AXD1050PG2M2EA1FNN	0.5V-10.5V	0-50 PSI

The sensor is connected to the corresponding wiring seen in Figure A.1 in the middle. The wiring system is shown in Figure A.1 and consists of three cables: black, white, and red. The black cable is connected to the COM, which likely stands for "common" or "ground." This connection provides a reference point for the other signals in the system. The white cable is connected to the OUT signal. This connection likely carries the actual sensor data that is being measured or detected. The red cable is connected to the EXC, which may stand for "excitation." This connection is seen in Figure A.1

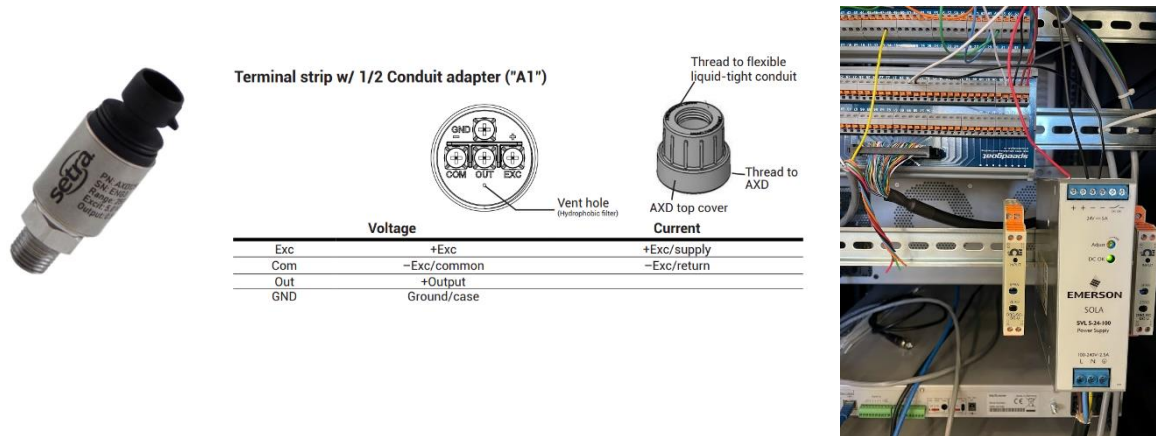


Figure A.1- Pressure sensor details

In order to calibrate pressure sensors for a data acquisition system, a test stand shown in Figure A.2 is being used. The test stand operates by sending different pressure values to the pressure sensor being tested.

To begin the testing process, a nitrogen tank is connected to the right side of the stand and turned on. The fluid is then allowed to flow through the pipe system, where it reaches the handheld pressure calibrators with interchangeable pressure modules (Omega PCL-1B).

Once the pressure has been adjusted in the system, it is sent to the pressure sensor itself. The sensor is connected to both the data acquisition system and a voltmeter, which allows the user to measure the voltage output from the sensor and ensure that it corresponds to the correct pressure value.

After the testing is complete, the piping system continues to another knob, which is turned to release the pressure and reset the system for the next round of testing. Overall, this test stand provides a reliable and accurate way to calibrate pressure sensors for use in data acquisition systems.



Figure A.2- Pressure sensor calibration stand

To ensure accurate calibration of pressure transducers, several steps must be taken to maintain stable conditions and minimize sources of error. First, it is important to ensure that the room temperature remains constant throughout the calibration procedure, varying no more than 10 degrees Celsius. Additionally, all electronic equipment should be allowed to warm up for at least 30 minutes prior to use to ensure that they are stable and operating properly [49].

It is also important to place the pressure transducer and calibration standards in the same environment in which they will be used for at least 24 hours prior to the calibration process. This allows them to adjust to the temperature and pressure conditions of the testing environment, which can help to ensure more accurate results.

Once the conditions are set, the pressure range to be calibrated should be determined and recorded. The electrical end of the transducer should then be connected to both the excitation source and readout instrument, as well as the pressure source, which is connected to a calibrated pressure gauge.

Next, the data recording process can begin. The first step is to record the output of the pressure transducer with no pressure on the system. Then, using the appropriate voltage increments determined by the pressure transducer's range, readings should be taken at each pressure increment for the full pressure range to be calibrated. After each reading, the pressure should be released back to zero.

Once all the data has been collected, the pressure transducer error should be calculated for each pressure increment. The values of error obtained should then be evaluated to determine if they fall within the tolerances specified by the manufacturer. If the percent error does not meet the specified requirements, the calibration process should be repeated. If the transducer still does not meet the tolerances after repeated attempts, it should be rejected from use in the experiment.

Determine pressure transducer error for each pressure increment:

$$Error = applied\ voltage - readout\ response \quad (A.1)$$

Percent error for each pressure increment:

$$Percent\ error = 100 \left(\frac{Error}{Applied\ voltage} \right) \quad (A.2)$$

Table A.2-Results of Sensor Pressure 1

Trial Sensor 1	Applied voltage	Readout voltage	Error	Percentage error	Corresponding Pressure (Psi)
	0.526	0.526	0.000	0.3	0
	1.504	1.499	0.005	0.6	4.83
	2.436	2.421	0.015	0.7	9.47
	3.631	3.606	0.025	0.7	15.43
	4.37	4.34	0.03	0.7	19.13
	5.78	5.74	0.04	0.8	26.19
	6.54	6.49	0.05	0.7	29.97
	7.52	7.47	0.05	0.5	34.82
	7.49	7.45	0.04	0.8	34.59
	8.84	8.77	0.07	0.5	41.31
	9.62	9.57	0.05	0.8	45.09
	10.05	9.97	0.08	0.6	47.24
	9.62	9.56	0.06	0.7	45.12
	8.74	8.68	0.06	0.7	40.77
	7.61	7.56	0.05	0.7	35.13
	4.23	4.20	0.03	0.4	18.28
	2.677	2.667	0.01	0.7	10.58
	1.596	1.585	0.011	1.0	5.22
	1.02	1.01	0.01	0.4	2.37
	0.687	0.684	0.003	0.4	0.75
	0.534	0.532	0.002	0.3	0

Table A.3-Results of Sensor Pressure 2

Trial Sensor 2	Applied voltage	Readout voltage	Error	Percentage error	Corresponding Pressure (Psi)
	0.524	0.524	0	0.00	0
	1.69	1.68	0.01	0.59	5.74
	3.754	3.732	0.022	0.59	16.02
	4.58	4.56	0.02	0.44	20.18
	6.97	6.93	0.04	0.57	32.04
	9.71	9.65	0.06	0.62	45.67
	6.64	6.6	0.04	0.60	30.36
	5.57	5.54	0.03	0.54	25.03
	2.682	2.665	0.017	0.63	10.66
	1.156	1.145	0.011	0.95	3.09
	0.531	0.53	0.001	0.19	0

Table A.4-Results of Sensor Pressure 3

	Applied voltage	Readout voltage	Error	Percentage error	Corresponding Pressure (Psi)
Trial Sensor 3	0.517	0.517	0	0.00	0
	8.24	8.19	0.05	0.61	38.42
	9.69	9.64	0.05	0.52	45.64
	6.07	6.04	0.03	0.49	27.61
	3.605	3.583	0.022	0.61	15.3
	2.561	2.549	0.012	0.47	10.11
	1.504	1.496	0.008	0.53	4.87
	4.65	4.63	0.02	0.43	20.58
	0.534	0.532	0.002	0.00	0

Once the setup is complete, the pressure should be increased in increments throughout the pressure range, and the corresponding voltage output from the pressure transducer should be recorded. This data can then be used to create a pressure vs voltage calibration curve, which will allow for accurate readings of pressure based on the transducer's voltage output seen in Figure A.3.

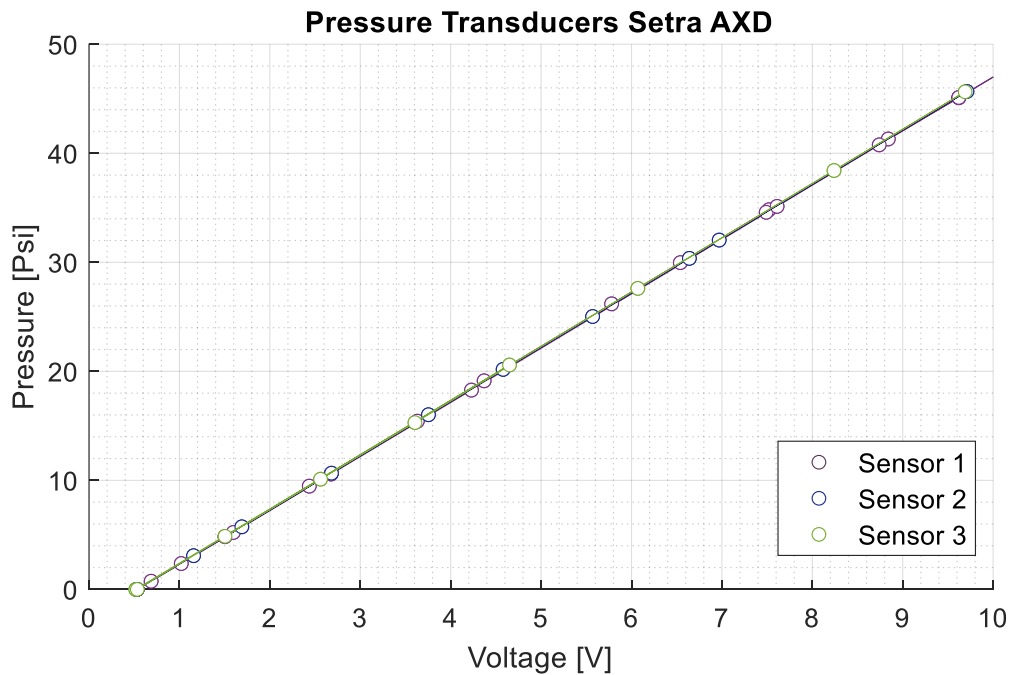


Figure A.3- Pressure vs. voltage of sensors

Flow meter

Calibrating a flow meter involves determining the relationship between the volumetric flow rate and the frequency output of the flow meter (K constant). This process typically involves the use of a calibration rig, which allows for precise control and measurement of the fluid flow.

The first step in calibrating a flow meter with a K constant is to establish a set of reference flow rates using a calibrated flow meter or a volumetric flow standard. These reference flow rates are used to create a calibration curve that relates the flow meter output frequency to the volumetric flow rate. The calibration curve is typically generated by plotting the reference flow rates against the corresponding frequency output from the flow meter.

The relationship between the volumetric flow rate and the frequency output of the flow meter can be expressed using the following equation:

$$Q = Kf \quad (\text{A.3})$$

where Q is the volumetric flow rate, K is the K constant of the flow meter, and f is the frequency output of the flow meter. The K constant is a characteristic parameter of the flow meter that relates the volumetric flow rate to the frequency output.

It is important to note that the viscosity of the fluid being measured can affect the accuracy of the flow meter calibration. In general, the K constant of a flow meter is specified for a particular fluid viscosity. If the viscosity of the fluid being measured differs significantly from the specified viscosity, the calibration curve may need to be adjusted to account for the difference in viscosity.

To account for the effect of viscosity on the flow meter calibration, the following correction factor can be applied to the flow meter output frequency:

$$f' = f (\mu/\mu_{ref})^{0.5} \quad (\text{A.4})$$

where μ is the viscosity of the fluid being measured, and μ_{ref} is the reference viscosity used to establish the K constant. The correction factor adjusts the flow meter output frequency to account for the effect of viscosity on the flow measurement.

In summary, calibrating a flow meter with a K constant involves establishing a set of reference flow rates, creating a calibration curve that relates the flow meter output frequency to the volumetric flow rate, and accounting for the effect of fluid viscosity on the calibration using the correction factor.

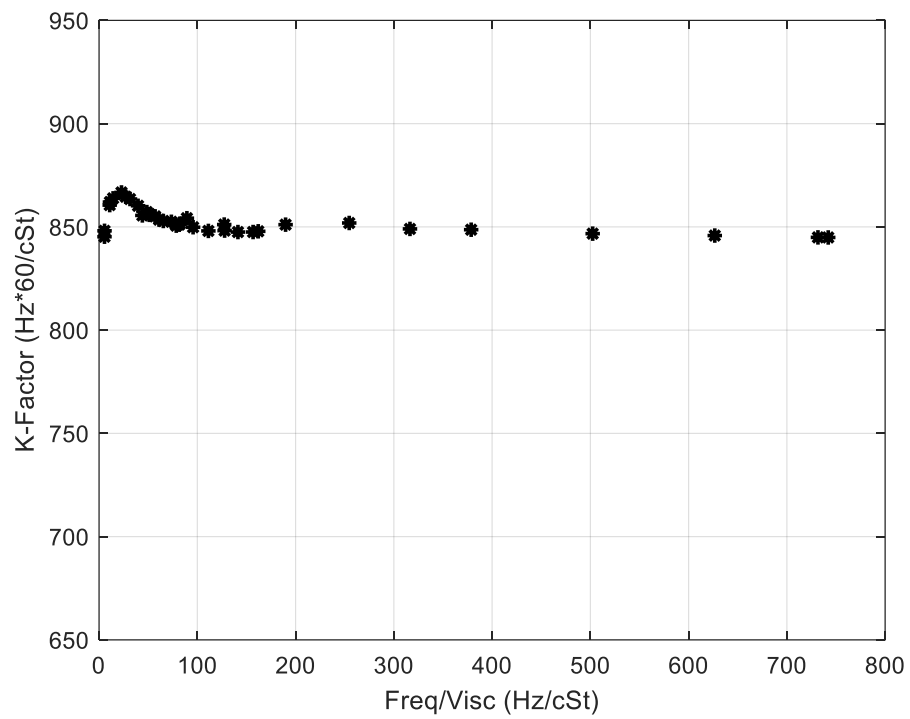


Figure A.4- Frequency vs. K-factor sensors

APPENDIX B: MINI-SPLIT OPERATING PROCEDURE

Table B.1-Operation procedure

A. Software Setup	
1	Open "Mini Split" folder located on desktop
2	Open "ModbusClient.slx" file
3	While loading up, open black cabinet and turn flip all power switches on
4	Make sure 2020b is selected on Speedgoat display
5	Assure TargetPC1 is connected
B. Precheck	
1	Check for any possible leaks around the mini-split unit
2	Check for any tools/materials around the unit that can cause a hazard
C. Mini-split Startup	
1	Flip breaker handle "up" to supply power to mini-split
2	Turn on low voltage power supply
3	Check if pressure transducers and mass flow meter are on
D. Operation	
1	Run the "ModbusClient.slx" simulink file
2	Check for connection (RS-485 light blinking, Gateway blinking, connection state = 1)
3	Input the test conditions required for desired test
4	Turn on unit via Simulink model ON/OFF switch
5	Acquire necessary data for the experiment
E. Shutdown	
1	Turn off unit via Simulink model ON/OFF switch
2	Ensure pressures have equalized
3	Stop the Simulink simulation
4	Shut off power supply and flip breaker "down" to power off mini-split

APPENDIX C: HEAT PUMP MODEL

The assumptions of the evaporator of the mini-split in other to calculate the loads is seen in the table below as well as for the condenser. The evaporator fan and condenser fan operate at a constant speed, and their airflow and power consumption were obtained from the manufacturer's data sheet since they were not measured. The steady-state values used for modeling were 0.816 m³ s⁻¹ for the evaporator flow rate and 33 W for power consumption, and 0.217 m³ s⁻¹ for the condenser flow rate and 252 W for power consumption.

Table C.1-Evaporator specifications [53]

Evaporator	Value	Units
Number of tubes	40	-
Length of tubes	737	mm
Outer diameter of tubes	6.35	mm
Inner diameter of tubes	4.83	mm
Longitudinal distance of tubes	19.1	mm
Transverse distance of tubes	12.7	mm
Fins per inch	20	-
Fin thickness	0.203	mm
Conductivity of fins	237	W/m-K

Table C.2-Condenser specifications [53]

Condenser	Value	Units
Number of tubes	80	-
Length of tubes	889	mm
Outer diameter of tubes	6.35	mm
Inner diameter of tubes	4.83	mm
Longitudinal distance of tubes	22.2	mm
Transverse distance of tubes	21.0	mm
Fins per inch	20	-
Fin thickness	0.203	mm
Conductivity of fins	237	W/m-K

A modified version of the AHRI 540 standard polynomial was utilized to model the continuous modulating compressor. The third-order polynomial equation, which is based on the published ratings from Mitsubishi Electric, uses 19 coefficients to account for the dependence of power and mass flow rates on the evaporating temperature, condensing temperature, and compressor rotational speed. The coefficients for the mass flow rate and power consumption correlations were estimated using the least squares method.

$$\begin{aligned}\dot{W}_{comp} = & c_1 + c_2T_{evap} + c_3T_{evap}^2 + c_4T_{evap}^3 + c_5T_{cond} + c_6T_{cond}^2 + c_7T_{cond}^3 + c_8RPM \\ & + c_9RPM^2 + c_{10}RPM^3 + c_{11}T_{evap}T_{cond} + c_{12}T_{evap}T_{cond}^2 + c_{13}T_{evap}RPM \\ & + c_{14}T_{evap}RPM^2 + c_{15}T_{evap}^2T_{cond} + c_{16}T_{evap}^2RPM + c_{17}T_{cond}RPM \\ & + c_{18}T_{cond}RPM^2 + c_{19}T_{cond}^2RPM \quad (D.1)\end{aligned}$$

$$\begin{aligned}\dot{m}_{suc} = & c_1 + c_2T_{evap} + c_3T_{evap}^2 + c_4T_{evap}^3 + c_5T_{cond} + c_6T_{cond}^2 + c_7T_{cond}^3 + c_8RPM + c_9RPM^2 \\ & + c_{10}RPM^3 + c_{11}T_{evap}T_{cond} + c_{12}T_{evap}T_{cond}^2 + c_{13}T_{evap}RPM + c_{14}T_{evap}RPM^2 \\ & + c_{15}T_{evap}^2T_{cond} + c_{16}T_{evap}^2RPM + c_{17}T_{cond}RPM + c_{18}T_{cond}RPM^2 \\ & + c_{19}T_{cond}^2RPM \quad (D.2)\end{aligned}$$

Table C.3-The estimated compressor model coefficients [53]

	C ₁	C ₂	C ₃	C ₄	C ₅	C ₆	C ₇	C ₈	C ₉	C ₁₀
W _{comp} (W)	-3322.157	-47.239	0.681	4.321x10 ⁻⁶	184.532	-3.585	0.024	30.874	-0.361	1.573x10 ⁻³
m _{suc} (kg/h)	64.684	0.107	-0.022	2.688x10 ⁻⁴	-3.853	0.077	-5.089x10 ⁻⁴	1.597	2.501x10 ⁻³	1.210x10 ⁻⁵
	C ₁₁	C ₁₂	C ₁₃	C ₁₄	C ₁₅	C ₁₆	C ₁₇	C ₁₈	C ₁₉	R ²
W _{comp} (W)	1.077	-2.316x10 ⁻³	0.068	5.498x10 ⁻⁴	-0.012	-8.570x10 ⁻³	-0.129	3.441x10 ⁻³	2.869x10 ⁻³	0.99
m _{suc} (kg/h)	0.011	-1.954x10 ⁻⁴	0.045	1.686x10 ⁻⁴	2.506x10 ⁻⁴	9.597x10 ⁻⁴	-2.966x10 ⁻³	-1.850x10 ⁻³	-2.558x10 ⁻⁵	1

Lastly, the expansion valve is assumed to be a constant enthalpy throttling process.

REFERENCES

- [1] Wagner, S. “The Apollo Experience: Lessons learned for Constellation dust management” NASA/TP-2006-213726, September 2006.
- [2] Wieland, P.O., "Living Together in Space: The Design and Operation of the Life Support Systems on the International Space Station. Volume 1," NASA/TM --1998-206956/VOL1, Jan. 1998.
- [3] Ramachandran, V. Dalal, S., Scheuring, R.A., and Jones, J.A. “Musculoskeletal Injuries in Astronauts: Review of Pre-flight, In-flight, Post-flight, and Extravehicular Activity Injuries. In: Effects of the Space Environment on Human Pathobiology” (R Kerschmann, Section Editor). Published online: 28 July 2018. Current Pathobiology Reports 6:149–158, <https://doi.org/10.1007/s40139-018-0172-z>, (Accessed 11.07.2022).
- [4] Dr. Megan Clark, “Principles For Cooperation In The Civil Exploration And Use Of The Moon, Mars, Comets, And Asteroids For Peaceful Purposes,” Oct. 2020.
- [5] Almirall Toribio , O , Boix , Á , Díez , C , Greaves , J , Molina Ordoñez , C , Murnaghan , M , Navarro Trastoy , A , Partal , N , Puljic , S , Sharique , S A H , Casanova , I (ed.) & Sureda , M (ed.) 2020 , “The Moon : The Next International Space Station” . UPC Postra., no. 16 , Iniciativa Digital Politècnica. Oficina de Publicacions Acadèmiques Digitals de la UPC , Spain . <http://hdl.handle.net/2117/328208>, (Accessed 10.14.2022).
- [6] S. J. Dyke, K. Marais, I. Bilionis, J. Werfel and R. Malla, "Strategies for the design and operation of resilient extraterrestrial habitats," in *SPIE Smart Structures + Nondestructive Evaluation Conference*, 2021.
- [7] J. E. Braun, S. A. Klein and J. W. Mitchell, "Effectiveness Models for Cooling Towers and Cooling Coils," in *ASHRAE Annual Meeting*, Vancouver, 1989.
- [8] M. Krishnan, Rajasekharan, and Pillai, “Modular Coupled Virtual Testbed.”2022.
- [9] 2006M. M. Shah, "A New Correlation For Heat Transfer During Boiling Flow Through Pipes," *ASHRAE Transactions*, vol. 82, pp. 66-86, 1976.
- [10] R. B. Malla and K. M. Brown, "Determination of temperature variation on lunar surface and subsurface for habitat analysis and design," *Acta Astronautica*, vol. 107, pp. 196-207, 2014.
- [11] Exploration Systems Architecture Study, “Exploration Systems Architecture Study Design Reference Missions for The Crew Exploration Vehicle,” 2020.

- [12] J. Park, H. Montoya, Y. Fu, A. Maghareh, S. J. Dyke and D. Ziviani, "Development of a Virtual Cyber-Physical Testbed for Resilient Extraterrestrial Habitats," in Thermal and Fluids Analysis Workshop, 2021.
- [13] M. R. Blackburn, A. Pyster, D.-M. Robin, T. Zigh, and R. Turner, "Results from Applying a Modeling and Analysis Framework to an FAA NextGen System of Systems Program Presented to: SoSECIE," 2021.
- [14] D. Correia, J. L. Marques, and L. Teixeira, "The State-of-the-Art of Smart Cities in the European Union," *Smart Cities*, vol. 5, no. 4, pp. 1776–1810, Dec. 2022, doi: 10.3390/smartcities5040089.
- [15] Winterhalter, D., Levine, J.S., Kerschmann, R. The Dust in the Atmosphere of Mars and Its Impact on the Human Exploration of Mars: A NESC Workshop. NASA/TM—2018-220084/NESC-RP-17-01263, <https://ntrs.nasa.gov/citations/20180006321>, (Accessed 01.20.2023).
- [16] Wallace, W. T. and A. S. Jeevarajan, (2015). Lunar Dust and Lunar Simulant Activation and Monitoring, [Address]. NLSI Lunar Science Conference, Houston, Texas. <https://www.lpi.usra.edu/meetings/nlsc2008/pdf/2015.pdf>
- [17] D. Kortenkamp *et al.*, "A Testbed for Evaluating Lunar Habitat Autonomy Architectures."
- [18] J. F. Connolly, "LM Nasa Lunar Lander Concepts Beyond Apollo."
- [19] C. Moler, "Hardware-in-the-Loop Testing for Power Electronics Control Design Featuring Simulink and Speedgoat real-time target machines," 2019. https://www.speedgoat.com/Portals/0/adam/ImageSlider/I1tyxPgUlkaCjD3_ssLXkw/Image/whitepaper_hil-testing-for-pecd_small.pdf, (Accessed 10.01.2023).
- [20] Wallace, W. T. and A. S. Jeevarajan, 2008. "Lunar Dust and Lunar Simulant Activation and Monitoring, NLSI Lunar Science Conference", 2015.
- [21] Taylor, S.R. (1979) Nickel Abundances in Lunar Mare Basalts, Lunar and Planetary Science X 1215-1216 [Abstract] <http://adsabs.harvard.edu/full/1979LPI....10.1215T>, (Accessed 11.15.2022).
- [22] Ruess, F., Schaenzlin, J., & Benaroya, H. (2006). "Structural Design of a Lunar Habitat. In Journal of Aerospace Engineering" (Vol. 19, Issue 3, pp. 133–157). American Society of Civil Engineers (ASCE). [https://doi.org/10.1061/\(asce\)0893-1321\(2006\)19:3\(133\)](https://doi.org/10.1061/(asce)0893-1321(2006)19:3(133))

- [23] P. Kessler, T. Prater, and T. Nickens, "Artemis Deep Space Habitation: Enabling a Sustained Human Presence on the Moon and Beyond," Institute of Electrical and Electronics Engineers, Mar. 2022.
- [24] A. Lial, "Interior Environment Modeling for Resilient Extra-Terrestrial Habitats," West Lafayette, Nov. 2022.
- [25] Friedman, R., Jackson, B., and Olson, S., "Testing and Selection of Fire -Resistant Materials for Spacecraft Use," NASA/TM--2000-209773, March 2000.
- [26] D. Madrzykowski, "Fire Dynamics: The Science of Fire Fighting," Fifth Annual Dr. John Granito Award for Excellence, (Vol. 7), 2012.
- [27] K. B. McGrattan, H. R. Baum, R. G. Rehm, A. Hamins, and G. P. Forney, "Fire dynamics simulator- technical reference guide," Gaithersburg, MD, 2000. doi: 10.6028/NIST.IR.6467.
- [28] Sircar, S., and Dees, J. "Evaluation of Fire Extinguishants for Space Station Freedom," NASA Johnson Space Center, White Sands Test Facility, Report TR-650-001, March 1992.
- [29] J. Mitchell and J. Braun, "Principles of Heating, Ventilation, and Air Conditioning in Buildings", vol. 1. John Wiley & Sons Inc., 2013.
- [30] Broyan, J., Welsh, D., & Cady, S. (2010). International Space Station Crew Quarters Ventilation and Acoustic Design Implementation. In 40th International Conference on Environmental Systems. 40th International Conference on Environmental Systems. American Institute of Aeronautics and Astronautics. <https://doi.org/10.2514/6.2010-6018>.
- [31] Wentz, F.J., K. Hilburn and D.K. Smith. 2012. RSS SSM/I Ocean Product Grids 3-Day Average from DMSP F11 netCDF [indicate subset used]. Data set available online from the NASA Global Hydrometeorology Resource Center DAAC, Huntsville, Alabama, U.S.A. doi: <https://dx.doi.org/10.5067/MEASURES/DMSP-F11/SSMI/DATA302>.
- [32] Fickett, "The Journal of Research of the Handbooks-Recommended codes of engineering and industrial practice," 2012.
- [33] Heymsfield, A.J., A. Bansemer, and M. Poellot. 2014. GPM Ground Validation NCAR Cloud Microphysics Particle Probes GCPEX. Dataset available online from the NASA Global Hydrometeorology Resource Center DAAC, Huntsville, Alabama, U.S.A.,doi:<https://dx.doi.org/10.5067/GPMGV/GCPEX/MUTIPLE/DATA201>.

- [34] S. Fuller, E. Lehnhardt, C. Zaid, K. Halloran, “Gateway Program Status and Overview”, IAC21, A3,2B,13,x66240, 72nd International Astronautical Congress 2021, Dubai, United Arab Emirates, 25-29 October 2021.
- [35] NASA, A Lunar Orbit That’s Just Right for the International Gateway, 16 May 2022, <https://www.nasa.gov/feature/a-lunar-orbit-that-s-just-right-for-the-international-gateway>, (Accessed 12.20.2022).
- [36] R. and A.-C. Engineers. American Society of Heating, 2009 *Ashrae Handbook: Fundamentals*. ASHRAE, 2009.
- [37] J. He, F. Pan, and C. S. Cai, “A Review of Wood-Frame Low-Rise Building Performance Study under Hurricane Winds,” 2016. Available: <http://www.elsevier.com/open-access/userlicense/1.0/> , (Accessed 02.25.2023).
- [38] W. Scholarship and A. L. Jaffe, “Internal Pressure Modelling for Low-Rise Buildings in Tornadoic Internal Pressure Modelling for Low-Rise Buildings in Tornadoic Winds Winds,” 2020.Available:<https://ir.lib.uwo.ca/etdhttps://ir.lib.uwo.ca/etd/7063>, (Accessed 02.25.2023).
- [39] J. H. Oh, G. A. Kopp, and D. R. Inculet, “The UWO contribution to the NIST aerodynamic database for wind loads on low buildings: Part 3. Internal pressures,” *Journal of Wind Engineering and Industrial Aerodynamics*, vol. 95, no. 8, pp. 755–779, Aug. 2007, doi: 10.1016/j.jweia.2007.01.007.
- [40] S. Bendapudi, J. E. Braun, and E. A. Groll, “A comparison of moving-boundary and finite-volume formulations for transients in centrifugal chillers,” *International Journal of Refrigeration*, vol. 31, no. 8, pp. 1437–1452, Dec. 2008, doi: 10.1016/j.ijrefrig.2008.03.006.
- [41] M. J. Moran, H. N. Shapiro, D. D. Boettner, and M. B. Bailey, “Fundamentals of Engineering Thermodynamics Eighth Edition,” 2014. Available: www.wiley.com/college/moran.
- [42] T. Bourgeois, F. Ammouri, M. Weber, and C. Knapik, “Evaluating the temperature inside a tank during a filling with highly-pressurized gas,” in *International Journal of Hydrogen Energy*, Elsevier Ltd, Sep. 2015, pp. 11748–11755. doi: 10.1016/j.ijhydene.2015.01.096.
- [43] T. Bourgeois, F. Ammouri, M. Weber, and C. Knapik, “Evaluating the temperature inside a tank during a filling with highly-pressurized gas,” *Int J Hydrogen Energy*, vol. 40, no. 35, pp. 11748–11755, 2015, doi: 10.1016/j.ijhydene.2015.01.096.

- [44] S. Bendapudi, J. E. Braun, and E. A. Groll, "A comparison of moving-boundary and finite-volume formulations for transients in centrifugal chillers," *International journal of refrigeration*, vol. 31, no. 8, pp. 1437–1452, 2008, doi: 10.1016/j.ijrefrig.2008.03.006.
- [45] Klein, "EES Engineering Equation Solver for Microsoft Windows Operating Systems Commercial and Professional Versions F-Chart Software 4406 Fox Bluff Rd Middleton, WI 53562," 2000. Available: <http://www.fchart.com>, (Accessed 02.25.2023).
- [46] K. Berwick, "MATLAB, 9.9.0.2037887 (R2020b) Update 8," Natick, Massachusetts: The MathWorks Inc., 2020.
- [47] J. E. Braun, S. A. Klein and J. W. Mitchell, "Effectiveness Models for Cooling Towers and Cooling Coils," in ASHRAE Annual Meeting, Vancouver, 1989.
- [48] M. Mihailović, U. Milovančević, S. Genić, B. Jaćimović, M. Otović and P. Kolendić, "Air side heat transfer coefficient in plate finned tube heat exchangers," *Experimental Heat Transfer*, vol. 33, pp. 388-399, 2020.
- [49] T. Dow Chemical Company, "SYLTHERM™ XLT Heat Transfer Fluid Technical Manual."
- [50] J. Park, H. Montoya, Y. Fu, A. Maghareh, S. J. Dyke and D. Ziviani, "Development Of A Virtual Cyber-Physical Testbed For Resilient Extraterrestrial Habitats," in Thermal and Fluids Analysis Workshop, 2021.
- [51] I. Bell, "CoolProp Documentation Release 4.0.0," 2013. Available: <https://docplayer.net/186925248-Coolprop-documentation.html>, (Accessed 02.25.2023).
- [52] M. Mihailović, U. Milovančević, S. Genić, B. Jaćimović, M. Otović and P. Kolendić, "Air side heat transfer coefficient in plate finned tube heat exchangers," *Experimental Heat Transfer*, vol. 33, pp. 388-399, 2020.
- [53] H. Sakiewicz, "Environmental Control System Modeling for Resilient Extra-Terrestrial Habitats," Purdue University Graduate School, 2023.